OPTICAL AND VIBRATIONAL PROPERTIES OF SINGLE-WALL CARBON NANOTUBES

by

W. Joshua Kennedy

A dissertation submitted to the faculty of
The University of Utah
in partial fulfillment of the requirements for the degree of

Doctor of Philosophy

in

Physics

Department of Physics and Astronomy

The University of Utah

May 2011

The University of Utah Graduate School

STATEMENT OF DISSERTATION APPROVAL

The dissertation of **W. Joshua Kennedy**

has been approved by the following supervisory committee members:

Z. Valy Vardeny	, Chair	**11/30/10** Date Approved
Jordan Gerton	, Member	**11/30/10** Date Approved
Eugene Mishchenko	, Member	**11/30/10** Date Approved
Paolo Gondolo	, Member	**11/30/10** Date Approved
Michael Morse	, Member	**11/30/10** Date Approved

and by **David Kieda**, Chair of the Department of **Physics and Astronomy**

and by Charles A. Wight, Dean of The Graduate School.

ABSTRACT

This work is a study of the optical properties of single-wall carbon nanotubes (SWNTs) using continuous wave (CW) modulation spectroscopy and resonant Raman scattering. SWNTs comprise a nanoscale, quasi-1D system in which the electrons are strongly interacting, resulting in the photo-generation of excitons. Our optical studies have revealed the behavior of these excitons under a number of different perturbations to the system.

We have used absorption, reflectance, electro-absorption (EA), photo-induced absorption (PA), charge-induced absorption (CIA), and resonant Raman scattering (RRS) on films of SWNTs. Our EA results provide strong evidence for the dominance of excitons in the optical absorption spectra of SWNT films. The absence of Franz-Keldysh oscillations and the presence of a derivative-like structure of the EA spectra indicate that the oscillator strength goes to the generation of excitons and not to interband electronic transitions. Furthermore, some of the photo-generated excitons are long-lived due to charge trapping in individual tubes within bundles, and this leads to a PA spectrum that is extraordinarily similar to the EA signal.

When SWNTs are electrochemically doped we see that the exciton absorption is bleached due to k-space filling and screening of the excitons by the modified local dielectric, while there is very little shift in the exciton transition energies due to band-gap renormalization. Simultaneously the infrared absorption, which is due to Drude free-carriers absorption, is enhanced. A similar behavior is observed in the case of direct charge injection. The RRS of doped SWNT samples shows a frequency shift of many of the Raman-active modes that is commensurate with the macroscopic actuation observed in nanotube-based electrochemical devices. This indicates that doping-induced changes in the lattice are connected with softening and stiffening of the vibrational modes.

Our results impact many proposed technologies that exploit the unique prop-

erties of SWNTs. Displays, batteries, and even photovoltaics that incorporate nanotubes are already in development. The performance and robustness of these devices could be improved when our results are taken into account.

For my family, and especially for Dr. J. Clifton Spendlove.

CONTENTS

LIST OF FIGURES

ACKNOWLEDGMENTS

I would like to thank my family for being my inspiration and my support during this process, and I especially thank my wife for being the person that she is. My parents and in-laws provided invaluable moral support and I am sure that they are almost as happy as I am to have finished this work.

I am extremely grateful to Dr. Vardeny for his insights, his enthusiasm, and most of all, his patience with me. I would like to thank the members of my committee for valuable discussions regarding my research. The physical resources necessary to complete this work were made possible by the facilities at the University of Utah physics department and I would like to give particular thanks to Matt DeLong, Wayne Wingert, Ed Munford, and Jolene Snyder.

CHAPTER 1

INTRODUCTION

1.1 The Structure of Carbon Nanotubes

The first carbon nanotubes were discovered almost twenty years ago by Sumio Iijima.[5] The walls of carbon nanotubes consist of the honeycomb-like two-dimensional lattice structure of graphene, and tubes can be either single walled (SWNT) or multiwalled (MWNT). Transmission electron microscopy and scanning tunneling microscopy of nanotubes reveal that the tube walls are closed, with no overlapping edge of the graphene lattice, and have a helical structure that depends on the way in which the graphene lattice is wrapped to form the cylinder. The graphene lattice may be wrapped in a countably infinite number of ways to form the seamless nanotube wall (see Figure 1.1). While in theory any one of these wrappings would form a stable configuration, in practice the kinetics of the growth mechanism limit SWNT sizes to around $0.5 - 2.5$ nm in diameter and $0.5 - 500$ μm in length. SWNTs as small as 0.2 nm in diameter[6] and as large as 6 nm in diameter[7] have been produced under well-controlled conditions.

Each nanotube may be characterized by the way in which the graphene lattice is wrapped to form it. The degree of helicity along the nanotube axis is called chirality, and each allowed geometry is characterized by the chiral vector. Figure 1.1a shows a diagram of the 2D hexagonal lattice along with the in-plane vectors associated with the nanotube geometry. The basis vectors of the 2D lattice are $\vec{a}$ and $\vec{b}$, while the chiral vector $\vec{c} = n\vec{a} + m\vec{b}$ points along the circumference of the tube (perpendicular to the axis) and determines the helicity and the diameter of the tube. The other pictures in Figure 1.1 represent tubes of different chiralities. Tubes for which the chiral indices are equal are called zigzag tubes because of the way the carbon atoms lie along the tube axis. Similarly, tubes for which $m = 0$ are called armchair tubes. All other tubes are simply called chiral due to the

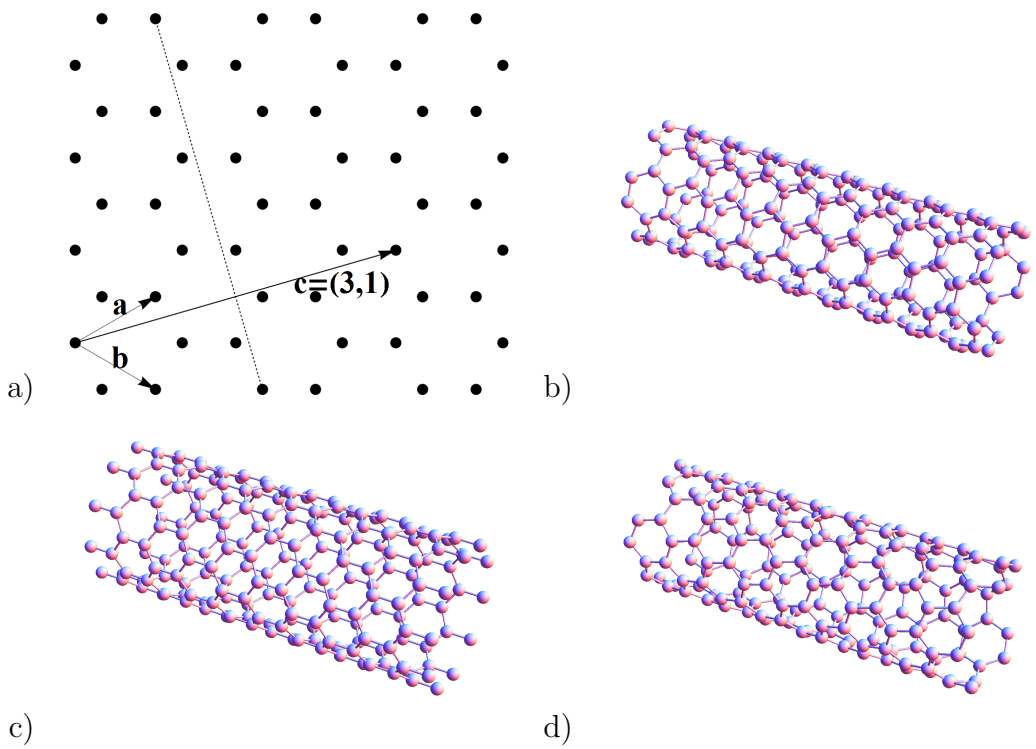

Figure 1.1. Lattice structure for SWNTs. a) 2D graphene lattice with basis vectors and the chiral vector $\vec{c} = (3, 1)$ shown. The dashed line corresponds to the direction of the nanotube axis (the length is not determined by the chiral vector). b) The zigzag tube (5,5). c) The armchair tube (10,0). d) The chiral tube (7,3).

twist of the carbon hexagons along the tube axis. The diameter of the SWNT is related to distance between nearest neighbor carbon atoms ($s = 1.44\ \mathring{A}$) and the chiral vector. For cylindrical tubes the magnitude of the chiral vector is the circumference of the tube, which leads to the following expression for the tube diameter.

$$d = \frac{|\vec{c}|}{\pi} \tag{1.1}$$

$$|\vec{c}| = \sqrt{3}s\sqrt{n^2 + m^2 + nm} \tag{1.2}$$

$$d = 0.793\mathring{A}\sqrt{n^2 + m^2 + nm} \tag{1.3}$$

Due to their enormous length to width ratio, nanotubes may be considered in many ways to be one-dimensional structures. The physical and electronic properties discussed below reflect the quasi-1D character of the nanotubes. Even though the chirality is defined in terms of the circumference of the tube, the wrapping also defines the configuration of the atoms along the length of the tube as seen in Figure 1.1a. Thus, the chirality also characterizes the one-dimensional properties of the tubes.

1.2 Production and Purification

While nanotubes are extremely stable, they are not a commonly occurring form of carbon due to the special conditions required for their production. Nanotubes were originally produced in a low-pressure inert atmosphere at the negative electrode of a carbon arc discharge chamber designed to produce fullerenes.[5] The first experimentally observed nanotubes were multiwalled, but SWNTs were soon produced.[8] Early experimental pursuits were limited, however, by the extremely low yield of nanotubes in arc-discharge production compared to other carbon species such as graphite and fullerenes. The exact mechanism of nanotube growth is still under investigation,[9,10] but it is understood that the growth rate, average diameter, and length of SWNTs depend on the temperature, pressure, and catalyst composition. Empirical advances have led to greater nanotube yields from the carbon-arc discharge method,[11] and such tubes are called arc-produced nanotubes.

Another method of nanotube production is the laser ablation technique. A target consisting of carbon with a small amount of Nickel and Cobalt for catalysts

is vaporized in an inert atmosphere with a short laser pulse, and carbon nanotubes form in the vapor phase as the material cools. Refinements in this method eventually resulted in a significant yield of SWNTs relative to multiwall tubes and debris - as much as 80% by some estimates.[12] Tubes produced in this way are called laser-ablation tubes, or just laser tubes.

A continuous flow method known as high pressure carbon monoxide (HiPCO) has been used to produce large quantities of SWNTs that are free from amorphous carbon and graphitic impurities (though they retain some metal catalyst impurities).[13] HiPCO tubes may be produced at rates up to tens of grams per day, but the benefit of high production rates and pure samples is offset by the large initial costs of establishing a HiPCO system. Other vapor-phase production mechanisms have also been used. For example, chemical vapor deposition (CVD) has been used to grow nanotubes directly onto substrates, and through a specific distribution of seed catalyst particles one can grow tubes of uniform size and orientation in this manner.[14] Similarly, direct CVD growth in preformed channels on crystalline substrates can result in isolated tubes nestled in crevices on the crystal surface.[6]

While various production mechanisms result in different diameter distributions of nanotubes (see Table 1.1), none is able to produce only one chirality of tubes (except for channel-grown CVD). Therefore, nanotube samples always comprise a range of chiralities corresponding to a particular range of diameters. Furthermore, the Van der Waals interaction between nanotubes causes them to aggregate into ropes or bundles. Bundling can have an impact on several of the nanotubes' electronic and vibrational properties as will be discussed in detail later in this work. Finally, nanotube samples invariably contain non-nanotube carbon species and usually contain residual catalyst materials such as nickel, iron, manganese, and other metals. The desire for pristine nanotube samples for experimental work necessitates the removal of these impurities. A variety of chemical, optical, and thermal treatments have been developed for this purpose and the reader is encouraged to consult several of the included references for further details.[15–17]

1.3 Physical Properties

One reason for the worldwide interest in SWNT is their enormous strength to weight ratio and tensile strength. The graphene lattice consists of trigonally bonded carbon atoms (three nearest neighbors) in which sp^2 hybridization results in σ bonds in the plane of the lattice and π bonds perpendicular to the plane. The σ bonds are particularly strong, making the tensile strength (the stress at which the tube breaks) for individual SWNTs around 50 GPa. Composite fibers and textiles made with carbon nanotubes have achieved elongation tensile strengths of over 1 GPa, greater than titanium and stainless steel. In compression, however, the tubes are prone to bending and the effective strength is much lower.

The unique character of the ubiquitous σ bonds in SWNTs gives rise to many surprising phenomena. For example, the bond lengths are particularly susceptible to change when sheets of nanotubes are electrochemically doped.[18,19] Furthermore, the interaction between orbitals along different symmetry axes gives rise to a negative Poisson's ratio in sheets of nanotubes,[20] meaning that when the sheet is stretched in one direction it expands in the perpendicular direction.

The interatomic forces that give nanotubes these extraordinary properties also govern the frequencies of the allowed lattice vibrational modes; thus, Raman spectroscopy is a useful technique for characterizing the physical properties of SWNTs. The vibrational spectrum of SWNTs can be approximated by the zone-folding technique applied to graphene.[8] Periodic boundary conditions are applied along the circumference of the tube, which gives a phonon dispersion consisting of one dimensional cross-sections of the two dimensional graphene dispersions. The phonon dispersion and density of states calculated in this way for the (10,10) armchair tube are shown in Figure 1.2. The most significant Raman-active modes are discussed in Chapter 4. The majority of phonon bands are doubly degenerate at the Γ point, and many of them are Raman-active.

1.4 Electronic and Optical Properties

1.4.1 Electron Dispersion

The valence band in SWNTs is made up of the hybridized σ and π bonds. Because of this, many of the electronic properties of SWNTs are similar to those

Table 1.1. Average diameters of nanotubes produced by a few common methods.

Production Method	Average Diameter (nm)
Arc-discharge	1.5
Laser ablation	1.5
HiPCO	1.0
CoMoCat	0.7
Zeolite	0.4
CVD	$0.6 - 2.2$

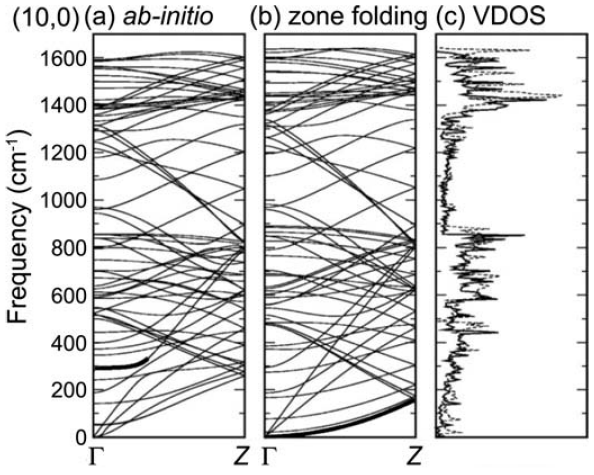

Figure 1.2. The phonon dispersion and density of states for a (10,0) armchair tube. a) The phonon dispersion along the nanotube axis calculated from first-principles. b) Phonon dispersion from the zone-folding method. c) The density of phonon states from first-principles (solid line) and zone-folding (dashed line). From.[1]

of π-conjugated polymers. However, as with the phonon modes, the electron band structure may be obtained by applying the zone folding method to the well known energy dispersion of graphene, which is a zero-gap semiconductor.[8] The result is a series of one-dimensional dispersions corresponding to different quantized values for the momentum in the circumferential direction as shown in Figure 1.3. Because of the way in which the zone-folding depends on the chirality, some nanotubes are found to have a nonzero density of states at the Fermi level, while others have a gap on the order of electron Volts. Thus, some tubes are semiconducting (s-SWNT) while others are metallic (m-SWNT). The armchair tubes (Figure 1.3a) are zero-gap semiconductors like graphite, while the chiral tubes (Figure 1.3b) have an appreciable energy gap.

In general, SWNTs are metallic if the difference between their chiral indices is divisible by three ($mod 3[n - m] = 0$); otherwise they are semiconducting. The exception is armchair nanotubes which are always zero-gap semiconductors. Thus, approximately one-third of any heterogeneous mixture of nanotubes are metallic and two-thirds are semiconducting.

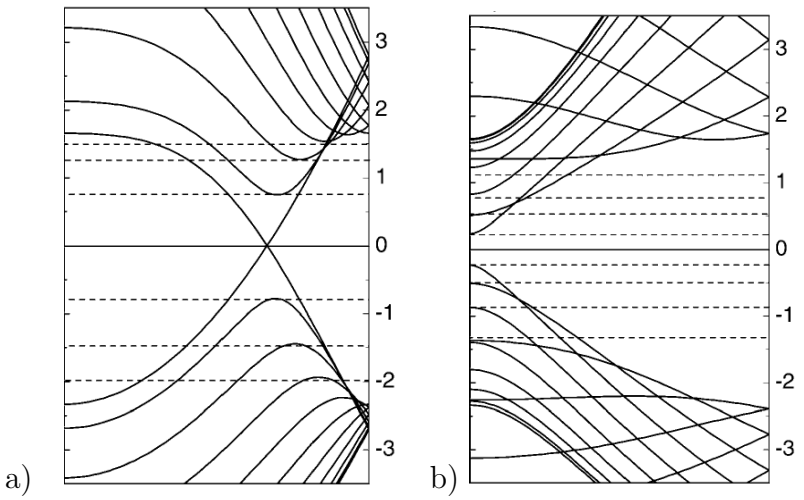

Figure 1.3. Electronic dispersion relations for two different nanotube chiralities calculated by the tight-binding approximation using third-nearest neighbors. a) Dispersion relation for the (10,0) armchair tube. b) Dispersion relation for the (19,0) chiral tube. From.[1]

1.4.2 Optical Absorption

In each of the plots in Figure 1.4 there appear a number of symmetric bands above and below the Fermi level. Each pair of symmetric bands corresponds to a different value of the circumferential component of the electron momentum. Each of these bands is quasi-1D, so the density of states contains sharp peaks called Van Hove singularities at symmetric positions above and below the Fermi level. Because of their one-dimensional nature the polarizability of SWNTs is very small perpendicular to the tube axis. Therefore, selection rules in SWNTs are such that the allowed photo-excited transitions occur between the members of these matched pairs. As a result, the optical absorption of light by SWNTs contains sharp peaks corresponding to transitions between these bands (see Chapter 3). The transitions are labeled according to their energy from lowest to highest. Thus E_{1-1} indicates the transition energy between the first valence band and the first conduction band, E_{2-2} is between the second valence and conduction band, and so forth.

The energy of these Van Hove transitions depends, of course, on chirality. Unfortunately, there is no simple analytical relationship between the chiral indices and the transition energies, but the dispersion relationship for an individual tube may be worked out according to the procedures described above. This has been

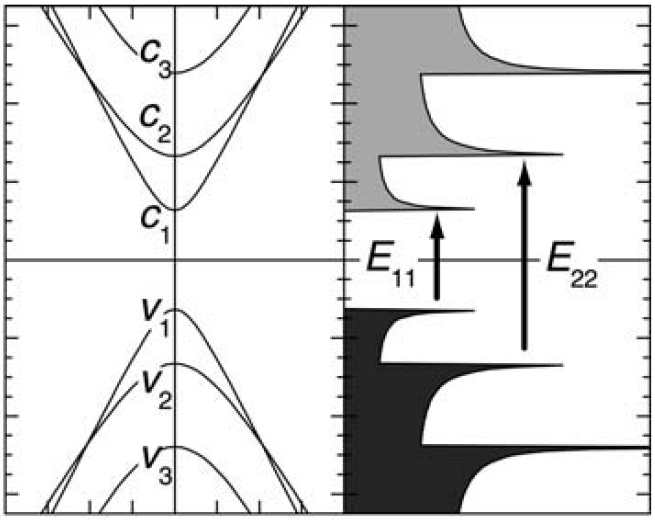

Figure 1.4. Band structure (left) and quasi-1D density of states (right) for a zigzag nanotube. Optically excited transitions are only allowed between symmetric Van Hove singularities as shown in the density of states diagram. From.[1]

done for a number of different tubes and the results are often plotted on a Kataura plot, named for Hiromichi Kataura who first generated it.[4] The Kataura plot represents a single transition for an individual tube as a point on a graph of energy vs. tube diameter as shown in Figure 1.5. The branches in the plot correspond to different indicies of the Van Hove singularities: the filled circles correspond to s-SWNTs while the open circles are m-SWNTs.

1.4.3 Excitons

The Kataura plot is extremely useful for predicting transition energies in nanotubes, but several factors reduce the precision to which the transitions can be calculated theoretically using Kataura's procedure. For example, the transition energies are particularly susceptible to perturbation from Van der Waals interactions in bundles, functionalization of the tube walls by impurities, and variations in the local dielectric constant due to surfactants and solvents. Furthermore, the Kataura plot is based on the tight-binding model for the electron dispersion relations, which ignores the effects of electron-electron interactions.

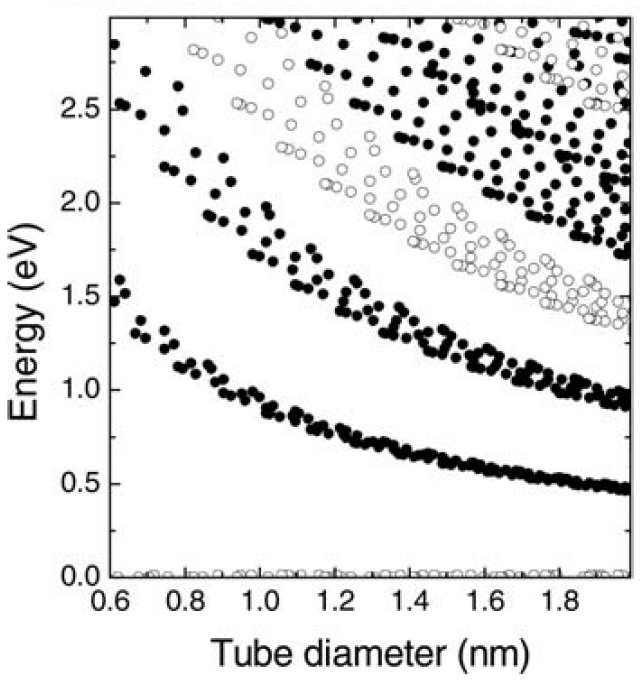

Figure 1.5. Kataura plot of electron transition energy between symmetric Van Hove singularities in the density of states for a variety of tube chiralities. From.[1]

All theories neglecting electron-electron interaction predict a ratio of $E_{2-2}/E_{1-1} = 2$ for large diameter tubes. However, experimental results extrapolated to large diameters have consistently measured $E_{2-2}/E_{1-1} = 1.8$.[21] This discrepancy is due to the large role that electron-electron interactions play in low-dimensional systems. In fact, theoretical work has shown that excitons play an important role in the photoexcitations in SWNTs.[22–24] Experimental measurements in two-photon absorption[25] and ultrafast dynamics[26] confirm the existence of excitons with large binding energies. In fact, because of their 1D character there are even bound excitons in m-SWNTs.[27] Thus, we now speak of all optical excitations in SWNTs as being excitonic. Still, the qualitative agreement with the tight-binding model due to the association of each exciton state with a continuum band makes tools like the Kataura plot and the language of Van Hove singularities useful.

1.5 Sample Characterization

Because the physical and electronic properties of individual SWNTs depend on the tube chirality we can use various optical techniques to characterize nanotube samples. First, some of the Raman modes in SWTNs have a strong dependence on tube diameter. In particular the Radial Breathing Mode (see Section 4.1) is inversely proportional to the diameter for most tubes. Equation 1.4 gives an approximate relationship between the frequency ω_{RBM} of the RBM and nanotube diameter d.

$$\omega_{RBM} = \frac{227 cm^{-1} nm}{d} \tag{1.4}$$

This relationship does *not* hold for armchair nanotubes.[1] Armchair nanotubes typically represent only a fraction of the tubes in a sample, though, so characterization of the average diameter via Raman spectroscopy of the RBM is still a valid procedure. Furthermore, because the Raman signal in SWNTs is strongly resonantly enhanced, a single Raman spectrum will only reveal a subset of the tubes in a heterogeneous sample. Therefore a variety of excitation frequencies is desired to obtain an average diameter distribution for a particular sample. The results can be compared with the standards given in Table 1.1 for the likely diameters resulting from a given production method.

Once the diameter distribution is known for a sample a vertical section of the Kataura plot (Figure 1.5) may be used to distinguish transitions in s-SWNTs from those in m-SWNTs. In many cases, depending on the required precision of the analysis, the Kataura plot may have to be modified according to the shifts in transition energies as discussed above.[28]

1.6 Summary: Motivation for this Work

It is worth noting that the 2010 Nobel Prize in physics was awarded to Andre Geim and Konstantin Novoselov "for groundbreaking experiments regarding the two-dimensional material graphene." Many of the properties of SWNTs are directly related to the corresponding features of graphene, and this year's Nobel Prize underscores the internationally recognized importance of these carbon structures. Nanotubes are of interest to the physics community because their unique architecture provides a meso-scale, quasi-1D system in which the connection between the atomic structure and the bulk properties is readily accessible. This is apparent when one considers the large range of scales over which nanotubes have been put to use in technology: from nano-electronics to large textiles.

1.6.1 Mesoscale Physics

Nanotubes consist of anywhere from a few hundred carbon atoms to several hundred thousand atoms. As such, they constitute a class of materials altogether different from other molecular or bulk materials. They are much larger than most large organic molecules, including both polymers and proteins. On the other hand, even though we speak of nanotubes as being semiconducting or metallic, the tubes themselves are much smaller than the smallest materials used in conventional electronic devices. They are quasi-one-dimensional, yet many of their properties depend on the orientation of the carbon atoms along their circumference, perpendicular to the tube axis. Thus, a precise understanding of carbon nanotube physics may be informed by knowledge of these other systems, but in the end it is unique to this mesoscale material.

The techniques of modulation spectroscopy and Raman spectroscopy have proven invaluable to the characterization of both π-conjugated polymers and bulk

metals and semiconductors. Thus, we have applied many of these techniques to SWNTs in an effort to better understand their properties. For example, the Raman experiments in this work connect changes in the nanotube lattice under electrochemical doping to macroscopic actuation of nanotube sheets, and the absorption measurements connect the behavior of excitons in individual tubes to the optical properites of heterogeneous nanotube sheets.

1.6.2 Potential Applications

While many of the proposed, potential applications for carbon nantubes are as yet unrealized, they have already found commercial use in textiles, military armor, chemical sensors, batteries, displays, photovoltaics, and even medicine. Nanotubes have been proposed as ideal materials for the next generation of computer technology, including the possibility of using the nanotubes to contain and manipulate qubits in quantum computers. There is a high demand for further understanding the physical and electronic properties of nanotubes so that their unique characteristics can be put to use in a variety of ways. We hope that we have contributed to this process in the current work.

CHAPTER 2

EXPERIMENTAL DETAILS

2.1 Introduction

In this chapter we describe the various experimental apparatus and procedures used in our study of SWNTs. It is our intent that these descriptions are complete and accurate to the degree that future graduate students would be able to repeat our measurements.

2.2 Sample Preparation

2.2.1 Impurities in SWNTs

Almost all of the manufacturing techniques discussed in the Introduction involve metal catalysts, organic solvents, graphitic precursors, and other impurities which generally remain with the nanotubes in further processing for measurements. Therefore, when interpreting electronic and spectroscopic data for SWNTs, it is always important to remember the fundamental limitations and possible artifacts due to these impurities. The constraints of each of our measurements typically require specific sample processing to eliminate such artifacts.

Carbonaceous impurities in nanotube samples include crystaline graphite, turbostratic graphite, amorphous carbon, and even fullerenes. These impurities can distort the electronic properties of nanotubes, and they have spectroscopic signatures in both absorption and Raman scattering that overlap with those of pure nanotubes (see Chapters 3 and 4). Therefore, the elimination of carbonaceous impurities is highly desirable for spectroscopic studies. Early efforts using oxidization to purify nanotubes were often detrimental to the nanotubes,[15] but subsequent techniques using organic molecules and polymers to selectively wrap nanotubes[29,30] met with more success. Modern methods use a combination of techniques,[16,17] and nanotube samples are commercially available at purity levels of 90-99.9%.

Metallic impurities are particularly undesirable for optical measurements since they tend to induce some intrinsic doping and also quench nanotube fluorescence. Even tubes produced by vapor deposition require metallic seed particles which result in metallic impurities as well as end-of-tube structural defects. Metallic impurities may be removed by acid treatments,[31] but such treatments reduce the average length of the nanotubes and introduce other structural defects which may be undesirable in some cases. Purified samples are produced by an elaborate procedure consisting of treatment with various acids and solvents.[17]

Finally, while not an impurity *per se*, the tendency of nanotubes to clump together into ropes or bundles is often an undesired characteristic. This bundling is illustrated in Figure 2.1. The strong intertube Van der Waals interactions distort the electronic structure of individual nanotubes and sometimes result in the mutual exchange of charge and the broadening of spectral features. In order to spectroscopically distinguish some of the tubes in a sample from other tubes in the same sample (such as identifying absorption peaks due to metallic tubes as being distinct from those due to semiconducting tubes) it is advantageous to reduce the size and number of those bundles. There are a variety of ways to accomplish this, but we mention two in the following sections.

2.2.2 Dispersions

In order to spectroscopically probe isolated nanotubes in a bulk sample it is necessary to suspend them in a liquid or solid matrix. With polymers and organic molecules this is typically accomplished by dissolving the material in an optically inert solvent. However, nanotubes are extremely insoluble in most common solvents. There are two standard solutions to this dilemma which are explained below.

It is possible to add functional groups to the walls of the SWNTs that make them more soluble in a particular solvent. This is accomplished by chemically bonding a soluble molecule to one or more of the carbon atoms in the nanotube.[32] The result is a nanotube with increased solubility. However, the functionalization distorts the electron orbitals, and in rare cases the tube structure, changing the tubes' electrical and optical properties. We chose not to use such samples for our

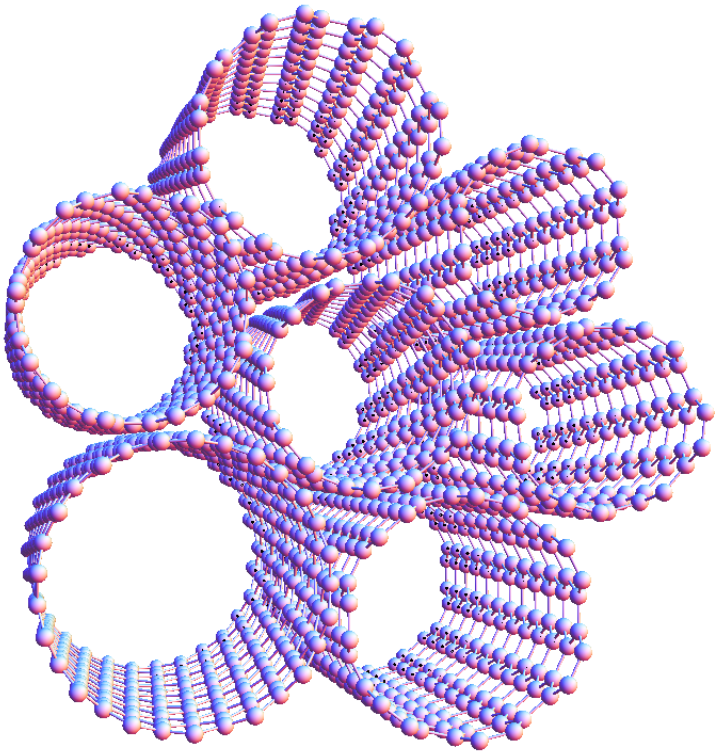

Figure 2.1. Nanotubes of different chiralities bundled together in a nearly hexagonal array via the Van der Waals force.

measurements.

In order to preserve the intrinsic properties of the SWNTs as much as possible we combined them with surfactants in solution. The surfactant, which consists of an organic molecule with a hydrophobic and hydrophilic side, wraps individual nanotubes and small bundles and suspends them in the solvent (see Figure 2.2). Larger bundles of nanotubes are not coated by the surfactant and fall to the bottom of the solution. A typical processing procedure is as follows below. This is based on techniques used by others,[28,33–36] but the specific process described here is the one we used to prepare samples for almost all of the measurements described in this dissertation.

- Combine 10 mg as-produced or purified SWNTs with 100 mg Sodium Dodecyl Sulfate (SDS, also known as Sodium Lauryl Sulfate, a common detergent) in 20 mL of water
- Place in a heated ultrasonic bath for 2 hours at $50°C$
- Place in centrifuge at 3000 rpm for 30 minutes
- Extract (via pipet) the top 80% by volume of the solution and discard the remainder

Dispersions produced in this manner may be used directly for spectroscopic measurements that are not sensitive to the aqueous solvent, or they may be further processed to make films. Also, once the nanotubes are isolated and suspended, the water may be allowed to partially evaporate (or more water may be added) to obtain a more (or less) optically dense dispersion. Over time the mutual affinity of the nanotubes causes them to begin to clump together again. Replacement in the ultrasonic bath restores the original degree of isolation of the nanotubes.

2.2.3 Films and Papers

Many of our experimental techniques require that we have bulk films of nanotubes. Such films may be produced starting with the aqueous dispersions described above.

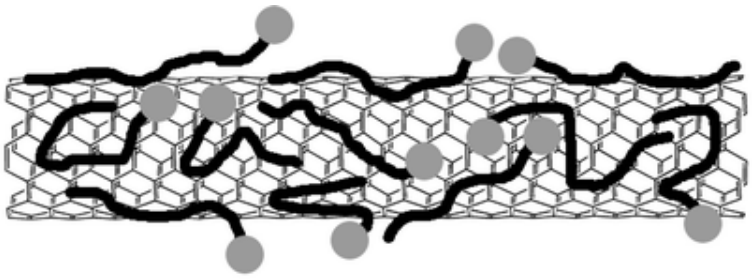

Figure 2.2. An individual nanotube coated with a surfactant such as SDS. The surfactant is "stuck" to the nanotube wall via π orbital overlap, but there is no chemical bond. The other side of the surfactant is hydrophilic, resulting in good dispersion in aqueous solutions.

First, thin films for use in transmission measurements such as absorption, electroabsorption, photoinduced absorption, etc. are made by drop-casting or spin-casting the aqueous dispersion onto a transparent substrate. Spin casting results in extremely thin films because of the low viscosity of the solvent, and drop casting results in an uneven distribution of nanotubes because of surface effects as the water evaporates. Therefore, the substrates are heated to 80°C before casting. This results in more rapid evaporation of the solvent and a thicker, more uniform film. The surfactant may be allowed to remain in the sample or it may be evaporated by annealing at $300°C$ for an hour or more. The addition of an optically inert polymer matrix such as polyvinyl alcohol (PVA) or polystyrene increases the viscosity of the solution, making spin-cast films thicker. An example of such a film is shown in Figure 2.3.

Thicker films are obtained in a more direct manner. Free standing films of laser ablation, HiPCO, and arc-produced tubes were prepared by scientists at Rice University and at the University of Texas at Dallas for use in Raman spectroscopy. These films, also called nanotube papers or buckypapers, were made by passing a dispersion of purified SWNTs through a fine filter at high pressures. The resulting black paper is several hundred microns thick and consists of interwoven bundles of SWNTs with only trace amounts of metal impurities (though the carbonaceous impurity level can be several percent). The paper is robust enough to be handled manually and to be wet and dried repeatedly without tearing or falling apart. A picture of such a film is shown in Figure 2.3.

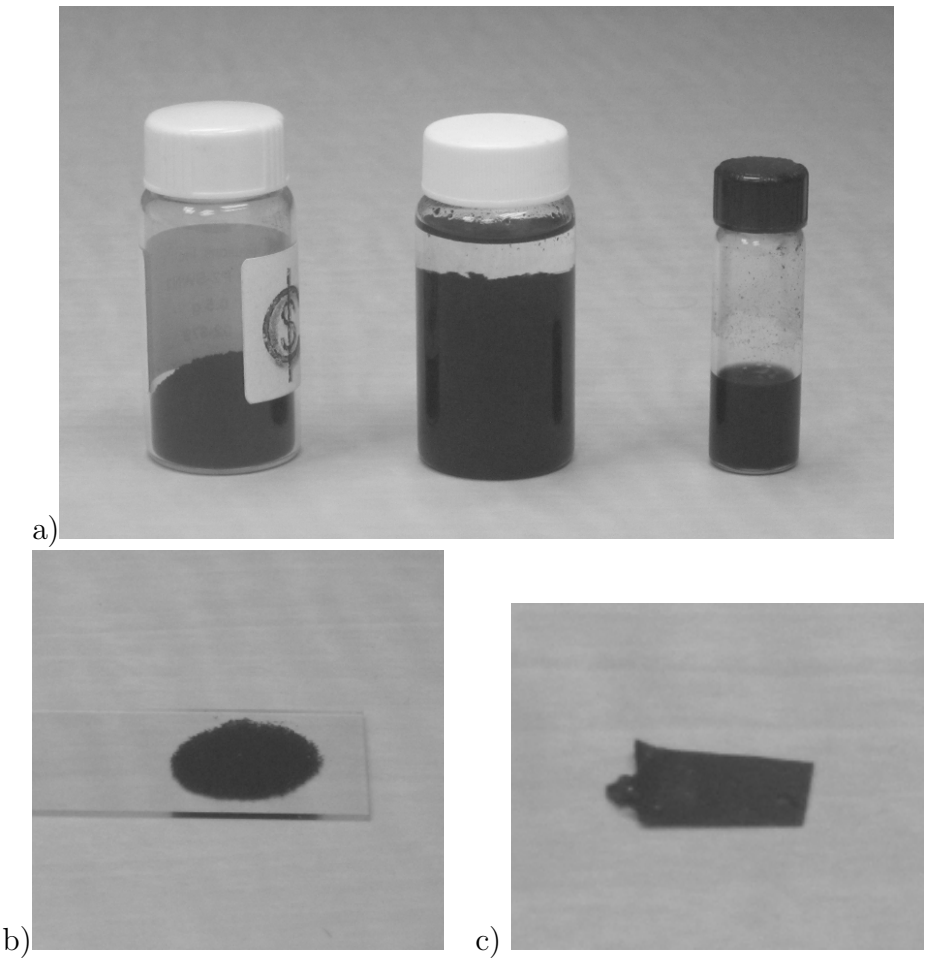

Figure 2.3. Nanotube samples in different preparations. (a) From left to right: raw nanotube powder, nanotubes sitting at the bottom of an aqueous mixture, nanotubes dispersed with surfactant in aqueous solution. (b) A film deposited on a glass slide from the aqueous dispersion. (c) A free-standing nanotube paper prepared by high pressure filtration.

2.3 CW Optical Techniques

2.3.1 Absorption and Reflectivity

The absorption of light through by matter is often described in terms of the absorption coefficient $\alpha(\omega)$, and the reflection is characterized by the reflectance $R(\omega)$l. The intensity I of light of a particular frequency ω transmitted a distance d through a material is related to the intensity I_0 of incident light according to the following relationship, which is illustrated in Figure 2.4.

$$I(\omega) = I_0(\omega)[1 - R(\omega)]^2 e^{-\alpha(\omega)d} \tag{2.1}$$

The optical density (OD) of a sample is a measure of its opacity. It is calculated from the logarithm of the transmittance so that it is linear with respect to the absorbance.

$$OD = -Log_{10}\left(\frac{I}{I_0}\right) = \frac{\alpha(\omega)d}{\ln 10} - 2Log[1 - R(\omega)] \tag{2.2}$$

In regions of the spectrum for which $R(\omega)$ is small, the first term in Equation 2.2 dominates and the OD is proportional to the absorbance $A = \alpha d$. On the other hand, if $R(\omega)$ is close to one then the second term dominates. Furthermore, if d is very small then multiple reflections can contribute measurably to the signal. The reflectance of nanotubes in the visible and near-infrared regions of the spectrum is indeed very small, so the optical density is proportional to the absorption coefficient. On the other hand, in the mid- and far-infrared the reflectance of SWNTs plays a significant role in the transmission of light through our samples.

One advantage of dealing with the absorbance is the relationship between the absorbance of two samples in the same beam path, such as a sample film and the substrate on which it rests. If the sample film F is deposited on a substrate S and the reflectance is negligible then the total optical density is

$$\begin{aligned} OD_T &= \frac{1}{\ln 10}(\alpha_S d_S + \alpha_F d_F) && (2.3)\\ &= OD_S + OD_F && (2.4)\\ \Rightarrow OD_F &= OD_T - OD_S. && (2.5) \end{aligned}$$

So, when the film consists of more than one layer one can find the absorbance of the film by subtracting the absorbance of the substrate from the total absorbance of the sample.

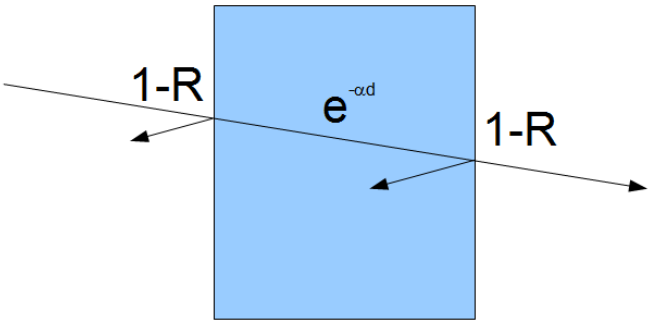

Figure 2.4. Diagram of the propagation of light through a sample with appreciable absorbance and reflectance. The fractional losses at the interfaces and inside the medium are shown.

2.3.1.1 UV-Vis Spectroscopy

Absorption in the ultraviolet, visible, and near-infrared regions was obtained using the Cary 3000 spectrophotometer. This device has two measurement channels, a sample chamber and a reference chamber, making it possible to directly measure the absorbance of a sample in one scan. It also is capable of correcting for a premeasured background shift that may be the result of optics within the instrument. It has its own light sources and detectors, making it a standalone instrument for direct spectroscopic measurements. Reflectance measurements are performed in the same way with a sample holder comprising two or more mirrors to direct the incident light to the sample surface and collect the reflected light.

When using the spectrophotometer for absorption measurements it is important to remember that the optical characteristics of the instrument can drift over time. For example, the temperature of the light source is not directly controlled, nor is the atmosphere inside the instrument monitored for changes in temperature or humidity. To minimize these influences a dual-channel configuration is used as shown in Figure 2.5. The background is adjusted by obtaining the ratio of the sample and reference chambers in the absence of any sample. That background is then subtracted from each spectrum to obtain the absorbance of the sample.

Because of this overall drift in the spectrophotometer, and because of the propagated uncertainty in the optical density, the absolute absorbance is not reliable

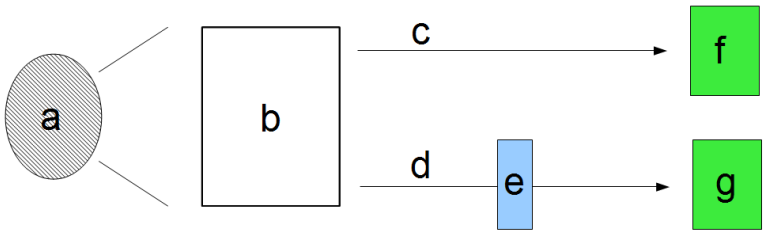

Figure 2.5. Simple schematic of the Cary spectrophotometer with (a) broadband light source (b) monochromator and beam splitter (c) reference beam (d) sample beam (e) sample (f) reference detector (g) sample detector.

enough to compare one sample with another if those two samples have different substrates, different surface reflectivities, etc. Most of the time the Cary is used simply to obtain the *shape* of the absorption spectrum, including the frequencies of absorption peaks and edges. The exception to this is in the well-controlled instance in which the sample and reference chamber are left untouched over the course of several measurements such as in the time-evolution measurements discussed in the next chapter.

2.3.1.2 Infrared Spectroscopy

Absorption in the infrared spectrum was obtained using the Bruker Fourier-Transform Infrared spectrometer (FTIR). The FTIR uses an interferometer with a moving mirror to obtain an interferogram of the light passing through the sample chamber. The real part of the Fourier-transform of this interferogram is the spectrum (the imaginary part is the phase). A simplified schematic of the FTIR is shown in Figure 2.6.

Because of the practical time scales of the scanning mirror and accompanying detectors the FTIR is particularly well suited for spectroscopic measurements between $10000cm^{-1}$ and $4cm^{-1}$. Molecular vibrations, free-carriers absorption, surface plasmons of some nanoscale structures, and the absorption by polarons in polymers are among the phenomena whose energies lie in this spectra range. The FTIR is designed to make direct spectroscopic measurements of absorption,

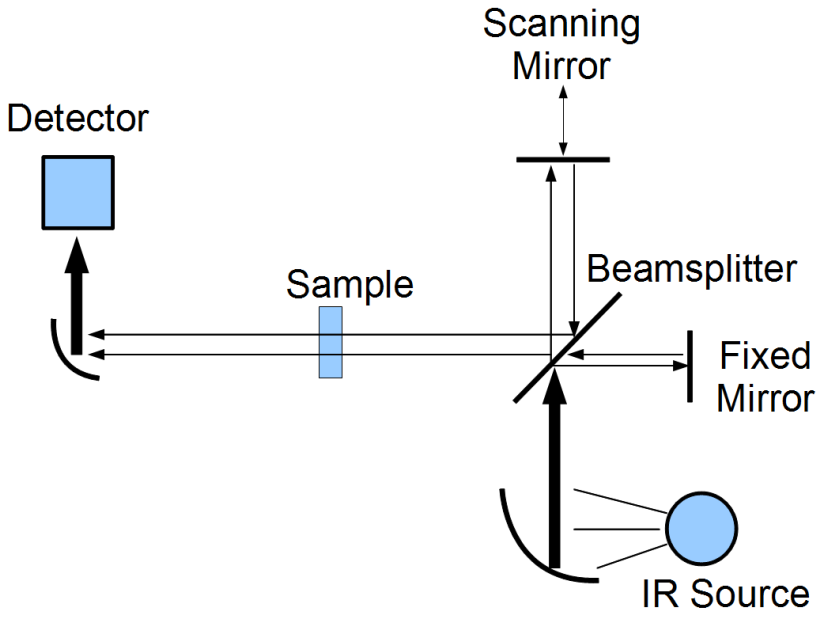

Figure 2.6. Simple schematic of the FTIR spectrometer. The movable mirror scans at a fixed rate, so the spectrum (intensity vs. frequency) is the Fourier–transform of the signal at the detector (intensity vs. time)

Raman scattering, fluorescence, etc. by comparing the sample signal to a reference background signal. However, we have also modified it with a macro to perform quasistatic modulation experiments such as electroabsorption and photoinduced absorption. For modulation we turn the electric field, excitation light, or other modulated influence on and off at regular intervals and average over many scans (sometimes thousands) to obtain the signal.

2.3.1.3 THz Spectroscopy

To investigate the absorption of our samples in the THz frequency region we used a pulsed laser antenna configuration to generate and detect electric fields as per the methods that were co-developed by our collaborator Dr. Ajay Nahata.[37,38] A schematic of the THz experimental configuration is shown in Figure 2.7.

A pulsed laser excites electrons and holes in the semiconducting target. These carriers are accelerated toward an array of antennae with a fixed potential difference. As they accelerate they produce a time varying electric field. The field is then detected using a similar antenna array that is unbiased, i.e., the incident

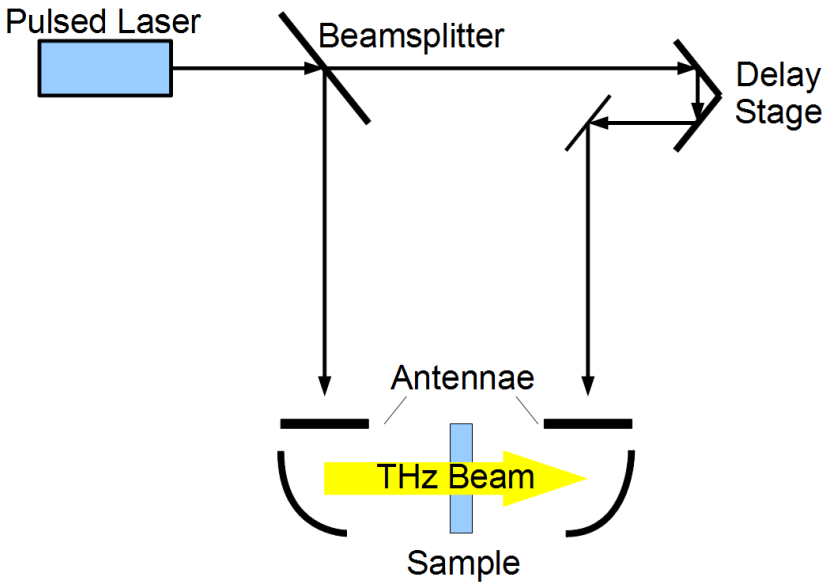

Figure 2.7. Simple schematic of the THz spectrometer.

field provides the potential that moves the photo-generated carriers. The typical frequencies of these fields are $0.01THz$ to $1.0THz$ as shown in Figure 2.8b. This allows us to probe the electronic nature of samples in a frequency range that is of great importance to emerging electronic technologies. The THz apparatus generates and detects electric fields directly, so it is inherently phase-sensitive. The real part of the Fourier-transform of the raw data makes up the spectrum, and the imaginary part of the transform gives the phase. The combination of the two allows us to calculate the complex index of refraction, which is done by software.

Figure 2.8a shows the raw data from the THz apparatus (averaged over 160 scans). In order to calculate the spectrum one must know the step size, which depends on the particular experiment. The frequency domain spectrum of the raw waveform is shown in Figure 2.8b. For most of our measurements the emitter is biased at $500V$ and the average pump power is $120mW$ with $50fs$ pulses. Typical scan speeds are about $5\mu m/s$, and more than 100 scans are needed for a signal-to-noise ratio of 10 or more, so the data collection often requires several hours. Sample signals are referenced to a background signal as in Equation 2.1 to determine the

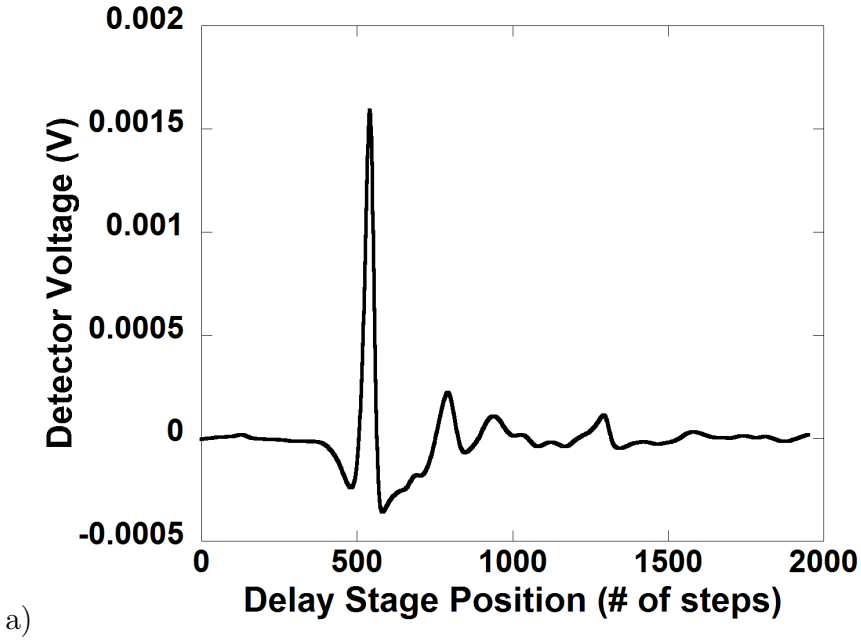

a)

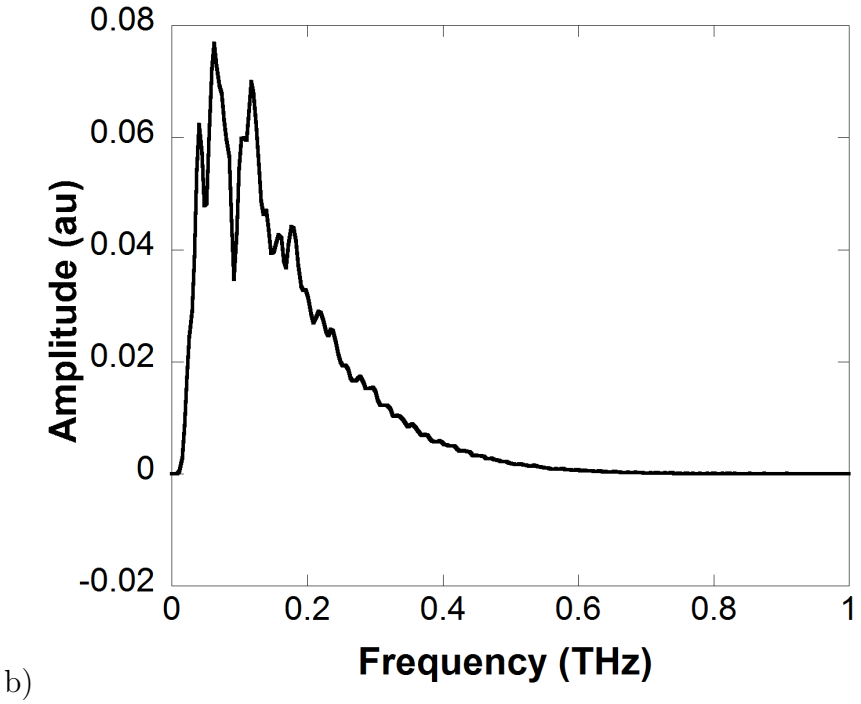

b)

Figure 2.8. Sample data from the THz apparatus. a) Signal at the detector vs. step number. b) Frequency domain spectrum calculated from the Fourier transform of the raw data.

complex index of refraction or the reflectance and absorbance.

2.3.2 Raman Spectroscopy

When a photon interacts with a molecule or crystal one possibility is that it is scattered inelastically, exciting a vibrational mode of the material and changing the energy of the scattered photon. Such a scattering process is called Raman scattering, and it is a powerful tool for spectroscopically probing the vibrational spectrum of a material. Only those vibrations that change the polarizability of the lattice (molecule) participate in Raman scattering. Vibrations involving a change in the permanent dipole moment are called infrared-active vibrations (IRAV) and do not participate in Raman scattering. The phonon modes that participate in Raman scattering are called optical modes, both longitudinal (LO) and transverse (TO).

Figure 2.9 depicts the quantum-mechanical theory of two Raman scattering processes. In the Stokes process an incoming photon is absorbed to a virtual electronic state and re-emitted with a lower energy. In the anti-Stokes process the incoming photon scatters off of an existing phonon and the scattered photon has a higher energy. Because of the distribution of phonons in the material the Stokes process is much stronger than the anti-Stokes process at room temperature. However, phonons produced through the Stokes process become available for participation in the anti-Stokes process, so that at high intensity excitation the nonequilibrium distribution of phonons can result in an anti-Stokes signal that is as strong as the Stokes signal.[39] In each case, the difference in energy is equal to the energy of the vibrational mode that participates in the process. Therefore, the spectrum of the *difference* between the incident and scattered photons is the spectrum of the Raman-active vibrational modes in the sample. The only phonons that participate in Raman scattering are those very close to the $k = 0$ point because the difference in momenta of the incoming and outgoing photons is very small compared to the phonon momenta.

In the Raman scattering measurement we excite our sample with laser light from an Argon, Helium-Neon, diode, or Krypton laser and collect the non-specularly scattered light using a low F-number lens. A band-pass filter is used on the

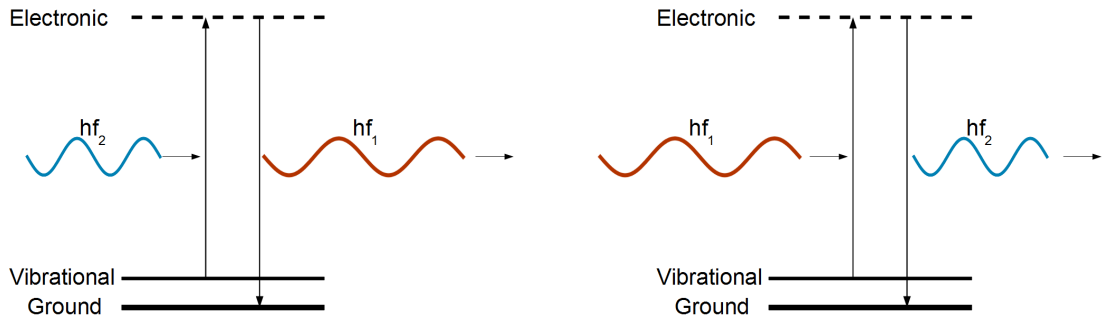

Figure 2.9. Energy level diagram for Raman scattering. The difference between the absorbed and emitted photon energies is equal to the vibrational energy. In the Stokes process (left) the incoming photon excites a vibration. In the anti-Stokes process (right) the existing vibration gives up its energy to the photon.

excitation beam to eliminate spurious fluorescence lines which are many times more intense than the Raman scattered signal. We use a high resolution spectrometer consisting of a triple-slit, triple-monochromator, and CCD detector to reject as much of the Rayleigh scattered light as possible. *In-situ* Raman spectra on electrochemically doped samples is obtained in the same way except that the incident and scattered light passes through the aqueous solution and the glass wall of the electrochemical cell. Figure 2.10 shows the important optical components in our Raman scattering experiment.

A careful calibration is performed for each position of the spectrometer gratings using standard fluorescent sources to minimize the error in wavelength. The Raman spectrum consists of the intensity spectrum of the energy difference between the incident and scattered photon as shown in Figure 2.9. Therefore, it is directly related to the phonon spectrum of the sample. The incident light is unpolarized and the heterogeneous samples are, on average, isotropic. However, in some of the SWNT papers we found evidence for inhomogeneities in the metal catalyst impurities that lead to enhanced scattering and fluorescence in certain areas of the sample. We eliminated such regions by moving the excitation beam to a different region of the sample where the fluorescence was minimized.

For some experiments we used a Witec confocal microscope for the Raman. The Witec is a sophisticated machine with tight spatial resolution. The excitation

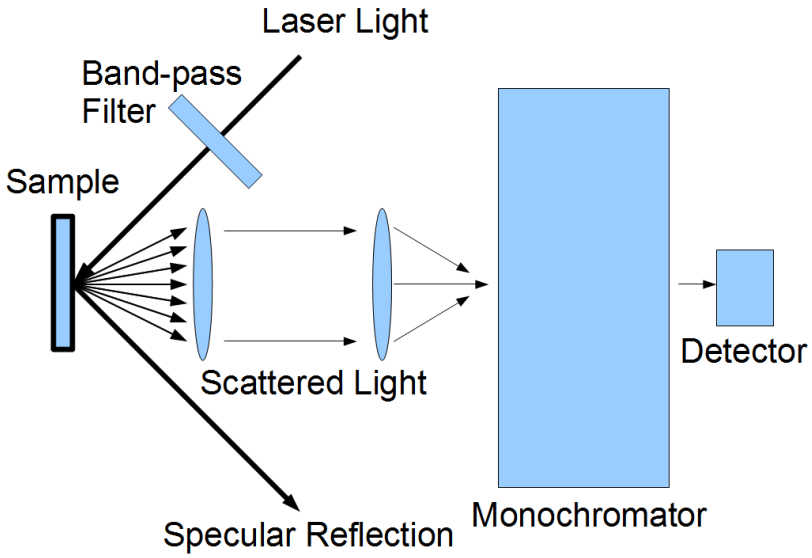

Figure 2.10. Schematic for the Raman scattering measurement.

is focused with a lens onto the sample and the back-scattered (or radiated, in the case of photoluminescence measurements) light is gathered with the same lens. The gathered light is directed to a CCD-array spectrometer after passing through a notch filter to eliminate the incident light. One advantage of the Witec system is its ability to raster point by point over an area of the sample to give high resolution Raman images, and that technique may be of use in the future to distinguish the signal coming from different regions of a heterogeneous sample. For example, we might better understand the distribution of the metal impurities through such a study.

Quite generally, the Raman cross-section is extremely small; the Raman scattered light is many orders of magnitude less intense than the Rayleigh scattering, which is an elastic process. However, in the case that the excited electronic state is a real state (instead of virtual), the Raman scattering efficiency can increase by as much as six orders of magnitude. This process is called resonance Raman scattering (RRS) and is particularly important in the Raman spectroscopy of SWNTs. As discussed in Chapter 4 it is the extreme RRS enhancement that allows us to distinguish among different species of tubes in a heterogeneous sample when measuring the Raman scattering spectrum.

2.4 Modulation Spectroscopy

The absorption coefficient $\alpha(\omega)$ of a material depends on its electronic properties, and that relationship may be probed by altering α through the influence of an external perturbation. Using a lock-in amplifier phase-locked to the source of the perturbation allows us to directly measure the change in a signal both in phase and out of phase with the perturbation. Suppose that α and R depend on an external influence F. If F changes, then α and R will change, and from equation 2.1 (dropping the explicit dependence on ω) we can calculate how the transmitted intensity would change as a result.

$$I = I_0(1-R)^2 e^{-\alpha d} \tag{2.6}$$

$$\frac{dI}{dF} = I_0\left(2(1-R)\delta R e^{-\alpha d}(\frac{dR}{dF}) + d(1-R)^2 e^{-\alpha d}(-\frac{d(\alpha d)}{dF})\right) \tag{2.7}$$

Again, if the reflectance and change in reflectance are negligible then we have

$$-\frac{\Delta I}{I} \approx \Delta\alpha d. \tag{2.8}$$

Thus, for small perturbations, the ratio of the modulated signal with the unmodulated signal is a direct measure of the change in the absorbance as a result of the modulation.

2.4.1 Photoinduced Absorption

In photoinduced absorption (PA) we measure the changes in a sample's absorbance as a result of pumping with a high-intensity, and usually monochromatic, excitation. The pump beam, typically a laser, excites electronic transitions, and the continuum probe reveals the influence of those excitations on the absorption of the sample. The method has been used extensively in organic materials, and various types of excitations can be distinguished by their PA signatures and accompanying frequency, polarization, and magnetic field dependence.[40–43] The experimental configuration for measuring PA is shown in Figure 2.11. The pump beam is modulated with a mechanical chopper or acousto-optic modulator (AOM) and the absorption of the white light continuum probe detected with a lock-in detector synchronized with the chopper. A long-pass filter negates artifacts due to second order diffraction of short wavelengths present in the beam. The phase

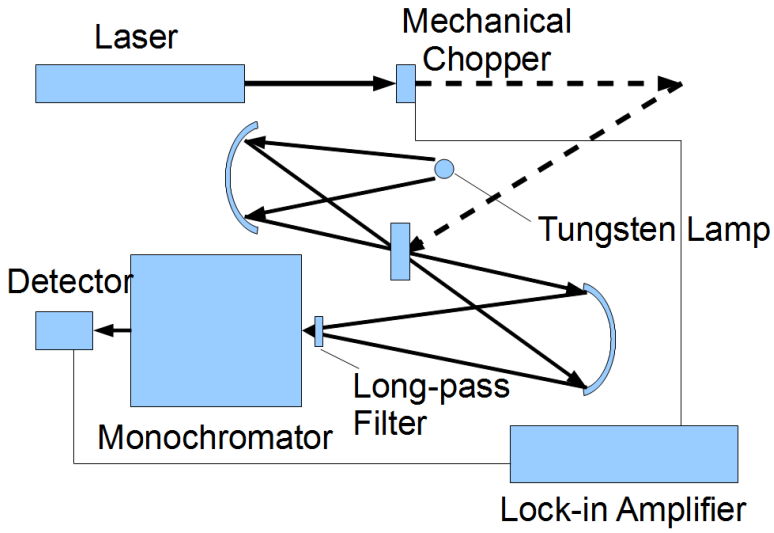

Figure 2.11. Schematic of the photoinduced absorption measurement (PA). The tungsten lamp provides the white light continuum probe, and the chopped laser provides the modulated pump beam.

of the lock-in detector is correctly found by maximizing the in-phase signal at the laser wavelength.

This is a very typical configuration for a variety of modulation spectroscopy techniques. The absorbance may be probed in a similar way by synchronizing the lock-in with whatever modulation one desires, such as electric field (electroabsorption), microwave field in a static magnetic field (optically-detected magnetic resonance), current (current-induced absorption), etc.

2.4.2 Electroabsorption

Electroabsorption (EA) is the measurement of the changes in absorbance of a sample perturbed by a quasi-static external electric field. Therefore, in order to measure EA on SWNTs one must modulate an electric field impinging on a collection of nanotubes. In order to observe a change in absorbance the perturbing field should be as large as possible on a sample that is transparent enough to measure (OD≈1).

Because SWNTs always contain both conducting and semiconducting tubes any sample with an appreciable optical density also has a significant electrical conductivity. Since the conductivity of the sample limits the field it can sustain

we want to isolate the conducting tubes from the semiconducting tubes as much as possible. For our electroabsorption samples SWNTs dispersed with SDS in water (as described above) were mixed with polyvinyl alcohol (PVA). PVA is electrically insulating as well as transparent in the UV-Vis-NIR spectral regions, and it is soluble in water. Typically the SWNT+SDS+PVA mixture consists of well isolated tubes (or small bundles thereof) drop cast in a 0.75 μm thick film with a total resistivity greater than 6×10^5 Ω-cm.

To produce a strong local electric field the sample is placed on top of an electrode array as shown in Figure 2.12. This array is produced by sputtering 50 nm of titanium and $200nm$ of gold onto a glass or sapphire substrate and then using photo-lithography to create the pattern shown. The resulting device consists of interlocking "fingers" $40\mu m$ wide with $40\mu m$ separation between electrodes. The length of each electrode is approximately 1.2 cm. These electrodes are contacted (via the large contact pads on either side) to the poles of an alternating voltage source, giving an alternating electric field in the gaps between electrodes. These gaps make up the region through which light passes so that 50% of the active area of the device is transparent. The measurement is then made using an optical path similar to the other modulation spectroscopy techniques as shown in Figure 2.13.

The voltage source comprises a low-voltage, sinusoidal signal generator and a high-frequency transformer which allow us to produce an electric field of up to $10^7 V/m$ in the gap at frequencies of $1kHz - 1MHz$. The maximum field, however, also depends on the resistance of the sample. The amplifier has a very low output impedance (less than 100 Ω), so if the resistance of the sample is low there will be energy dissipated in the sample and the voltage drop across the sample will be significantly lower. In practice we found that sample resistances greater than 1 MΩ between the two contacts are necessary to obtain a clean EA signal (preferably greater than 10 MΩ).

In an isotropic system such as a disordered film of nanotubes the change in absorption in the presence of an electric field does not depend on the direction of the field. Thus the EA signal is related most strongly to the third order nonlinear susceptibility matrix $\chi^{(3)}$, which depends on the square of the applied field. Therefore, EA is obtained by measuring the transmission of the sample

Figure 2.12. Diagram of the electroabsorption antenna array. A varying potential difference between the two contact pads results in a varying electric field between the electrode fingers.

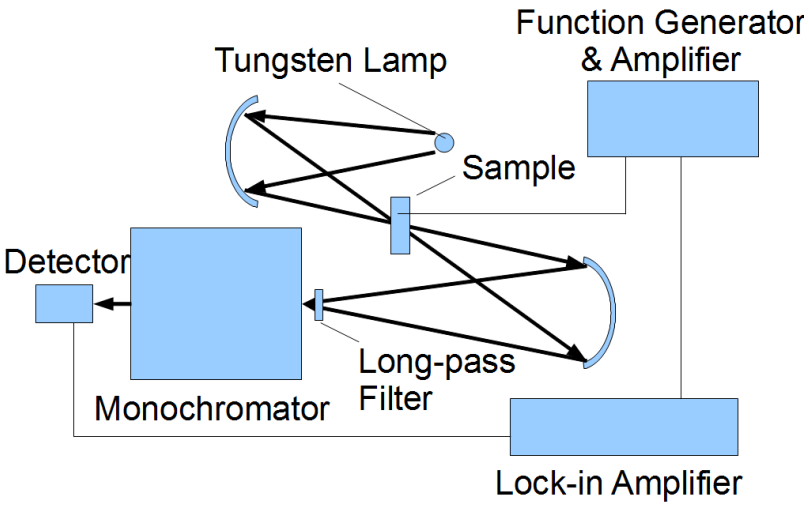

Figure 2.13. Diagram of the electroabsorption experiment. The lock-in amplifier is synchronized at twice the frequency of the applied field, but the phase is arbitrary. The phase must be set using information from some other method.

is with a lock-in amplifier synchronized with the signal generator at *twice* the modulation frequency of the generator (second harmonic of the lock-in).

One challenge in EA that is not present in PA measurements is the task of assigning the phase of the lock-in detector. Since there is no direct optical signature from the electric field itself we must determine the phase independently. In our experiments we used the quasi-static approach with the FTIR (discussed in Chapter 3) to determine the phase of the signal in the infrared and then multiplied the in- and out-of-phase spectra at higher energies by the appropriate factor to adjust the phase afterwards. We performed further validation of this approach by measuring the EA signal for the nanotube samples simultaneously with other materials for which the EA signal is known, such as MEH-PPV.

2.4.3 Charge-induced Absorption

Charge-induced absorption (CIA) is the measurement of changes in absorbance of a sample upon directly injecting charges (i.e., current). When a potential difference is maintained across a conductive material charges are injected from the electrodes to provide the current. These charges are extrinsic to the material and can have an influence on the material's intrinsic properties, such as α. In practice, the charge-induced absorption technique is very similar to the electroabsorption discussed above, and the experimental setup is shown in Figure 2.14. However, for charge induced absorption we want to maximize the number of injected carriers. This is accomplished by making the gap between electrodes very small and modulating at a much lower frequency: hundreds of Hertz instead of thousands. Since the charge injection depends on the quality of the contact interface a different geometry is used. Figure 2.15 illustrates a device appropriate for measuring the charge-induced absorption. The cathode and anode consist of thin layers of conducting material between which the sample is deposited. The challenge is to deposit the electrodes in such a way that the absorption can still be measured.

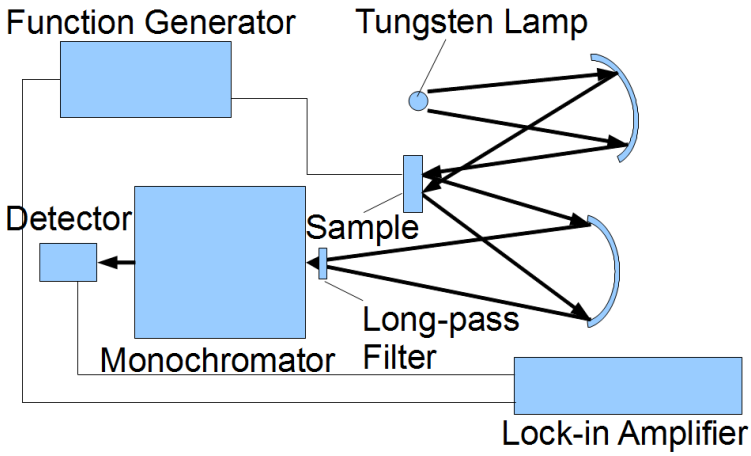

Figure 2.14. Diagram of the CIA experiment in reflection mode using a sample as shown in Figure 2.15.

2.4.3.1 Optical Considerations

One way to obtain the absorption in the CIA device is to make one electrode and the substrate transparent to light in the spectral range in which we are interested. For example, Indium-Tin-Oxide (ITO) is a conducting material that is transparent in the visible and near infrared. The other electrode is made to be reflecting in the same spectral range (e.g., Aluminum) and the transmission through the sample is obtained by reflecting the incident light off of the rear electrode. In this configuration the change in absorbance is not able to be measured directly from the modulated and unmodulated signals, because each includes the intensity from several reflections. The following derivation refers to values specified in Figure 2.15(c) for the various reflected and transmitted intensities. Ignoring secondary reflections gives a good approximation for what we can expect for the signal under modulation of some influence F as compared with Equation 2.8.

$$I = I_0(1-r_g)^2(1-r_I)^2(1-r_S)^2 r_A e^{-2\alpha d} + I_0 r_g ... \quad (2.9)$$

$$+I_0(1-r_g)^2 r_I + I_0(1-r_g)^2(1-r_I)^2 r_S \quad (2.10)$$

$$= I_0\left(Ae^{-2\alpha d} + B\right) \quad (2.11)$$

$$\Rightarrow -\frac{\Delta I}{I} \approx \frac{2\alpha d A e^{-2\alpha d}}{Ae^{-2\alpha d} + B} \quad (2.12)$$

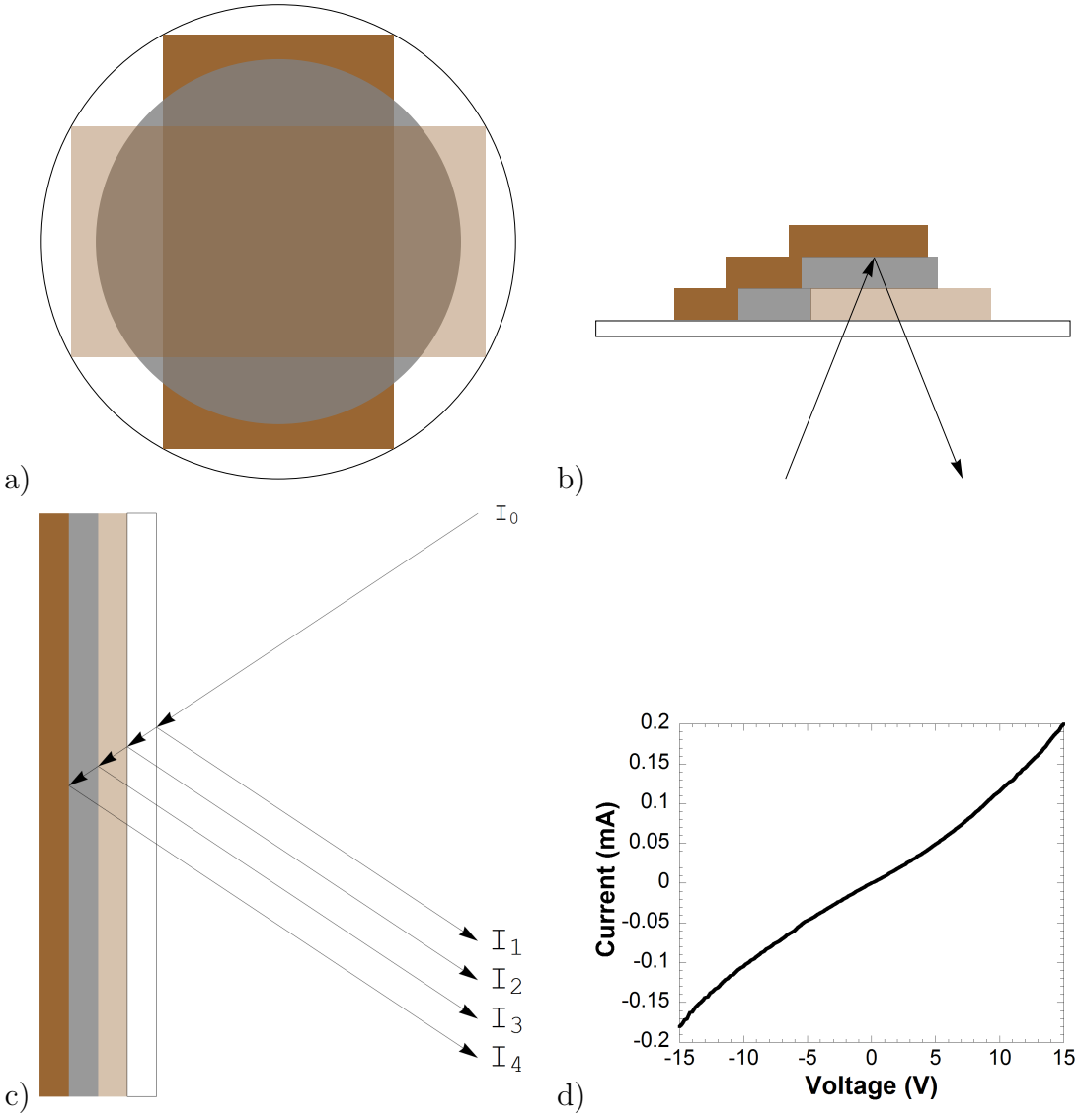

Figure 2.15. The charge-induced absorption device. (a) A top view of the device showing the cross-orientation of the rectangular electrodes with the circular nanotube film between. (b) A cross-sectional view showing both electrodes in contact with the substrate and open for contact from above. (c) A detailed diagram of the various sources of light at the detector due to multiple reflections in the device. (d) The I-V characteristics for the device.

Since the reflectivity of the glass is not negligible compared to the reflectivity of aluminum we cannot neglect the term B in the denominator and the ratio $\Delta I/I$ is not proportional to the change in absorbance. Therefore, to find the change in absorbance we need to either measure B directly (i.e., measure the reflectivities and transmittances of each portion of the device) or measure I_0 directly; we measured the reflectivities of each surface independently and used the results to calculate the CIA signal.

In the other configuration both electrodes are transparent enough for the transmission to be measured directly through the whole device. The reflection configuration is more robust, but more difficult to analyze, whereas the transmission configuration is easier to measure and analyze but far more vulnerable to electronic shorts and open circuits (e.g., failure to connect the source and drain electrodes). Because the devices are so much harder to fabricate in transmission mode our CIA spectra were obtained exclusively in the reflection mode as shown in Figure 2.14.

2.4.3.2 Work-Function Considerations

There are multiple electronic configurations possible in a CIA device. The relative size of the work functions of the two electrodes and the sample determine how efficiently electrons or holes are injected into the device. In the language of molecular energy levels the electrons in the nanotubes reside in the highest occupied molecular orbital (HOMO) and electrons can only be injected into the lowest unoccupied molecular orbital (LUMO). By an appropriate choice of electrodes, and sometimes additional transport layers, one can control whether electrons, holes, or both are injected over a given range of voltages.[44] Figure 2.16 shows the energy diagram for carriers in a SWNT device for two different electrode configurations used in our experiments. Contact effects, including Fermi-level pinning, are not shown here, but the schematic illustrates the overall behavior. In general, electrons are injected when the LUMO of the sample is close to the work function of the electrode and holes are injected when the HOMO is close to the electrode work function. Many reports of the work function of SWNTs have been given,[45,46] and the overall consensus is that the average HOMO level for SWNTs is between

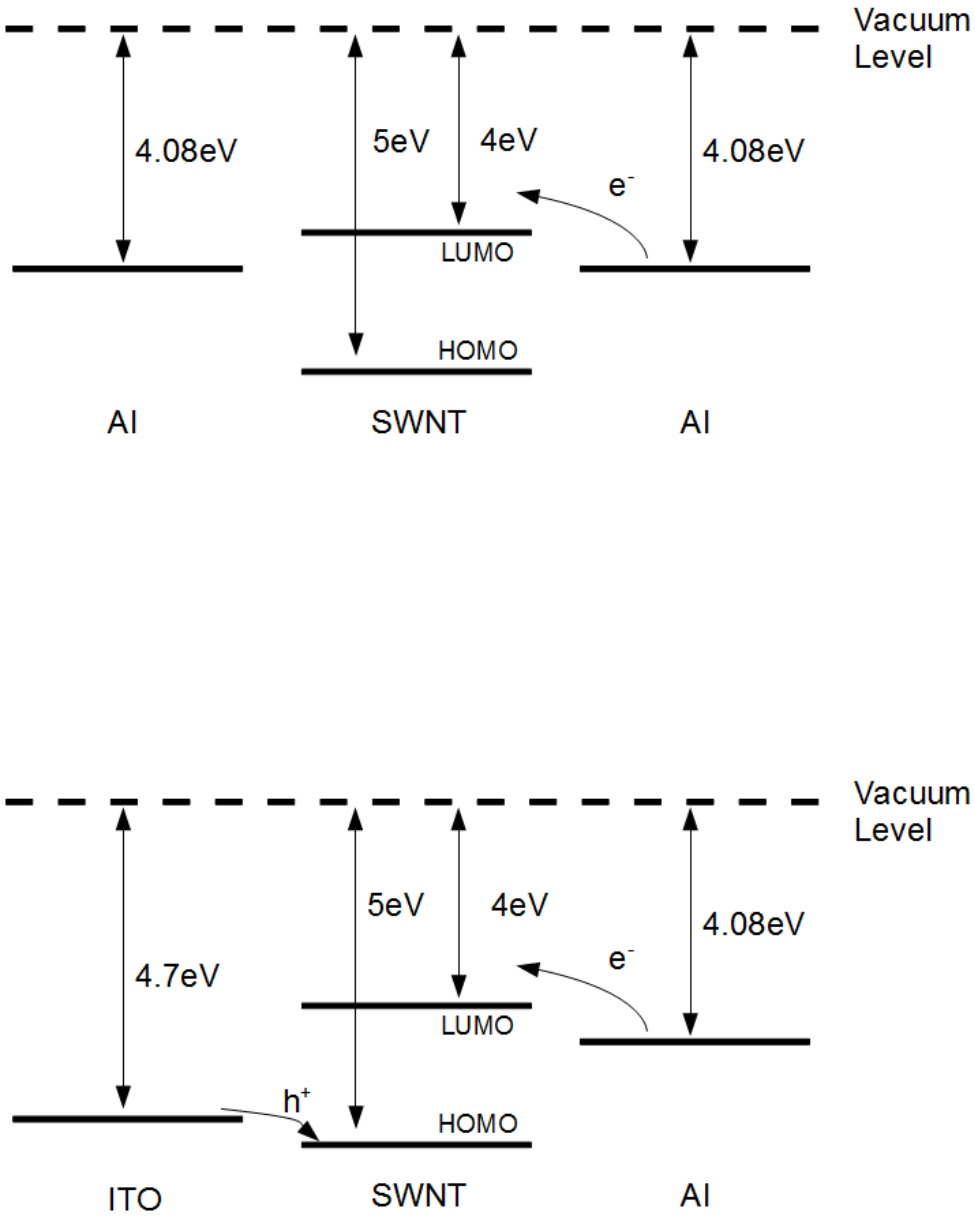

Figure 2.16. *Electron* energy level schematic for a unipolar (top) and bipolar (bottom) device for charge injection. Material work functions are depicted as relative distances below the vacuum energy. Under modest bias electrons can move easily between close energy levels.

$4.85eV$ and $5.1eV$ below the vacuum level.

Our CIA spectra were obtained with ITO/Aluminum electrodes (bipolar device) and with Aluminum/Aluminum electrodes (unipolar device). The nonlinear current-voltage curve for the unipolar device is shown in Figure 2.15(d). We note that we were unable to obtain CIA spectra for devices using gold for both electrodes. We attribute this to the close matching between the work functions of gold and SWNTs, which results in a more Ohmic contact.

2.5 Electronic Techniques

2.5.1 Electrochemical Doping

Electrochemistry is essentially the process of producing chemical reactions at the interface of an electrode and an electrolyte solution. The electrochemical cell comprises the electrolyte, a working electrode, a counter electrode, and a reference electrode. The electrolyte may be either solid or liquid, but in either case it functions as a channel for ionic conduction between the electrodes. The working electrode is the electrode of interest in the particular reaction being studied. The counter electrode provides the potential bias that drives ions toward or away from the working electrode. Finally, the reference electrode provides a known reference voltage to which the voltage at the working electrode may be compared. A potentiostat provides feedback control by adjusting the potential at the counter electrode such that the potential difference between the working and reference electrodes is maintained at the desired level. In cyclic voltammetry one measures the current as a function of potential over a certain range to identify the chemical potentials at which certain reactions take place.

In the case of electrochemical doping the "reaction" at the working electrode is simply the addition or removal of charges due to the physical proximity of ions from the solution. In the ideal case no chemical reaction occurs at the interface, so there is no plateau or step in the I-V curve.[47] Figure 2.17 shows a simplified diagram of how electrochemical doping functions. A negative applied potential at the counter electrode (not pictured in 2.17b) attracts positive ions and repels negative ions and results in a positive potential difference between the working electrode and the solution. The increased concentration of negative ions at the

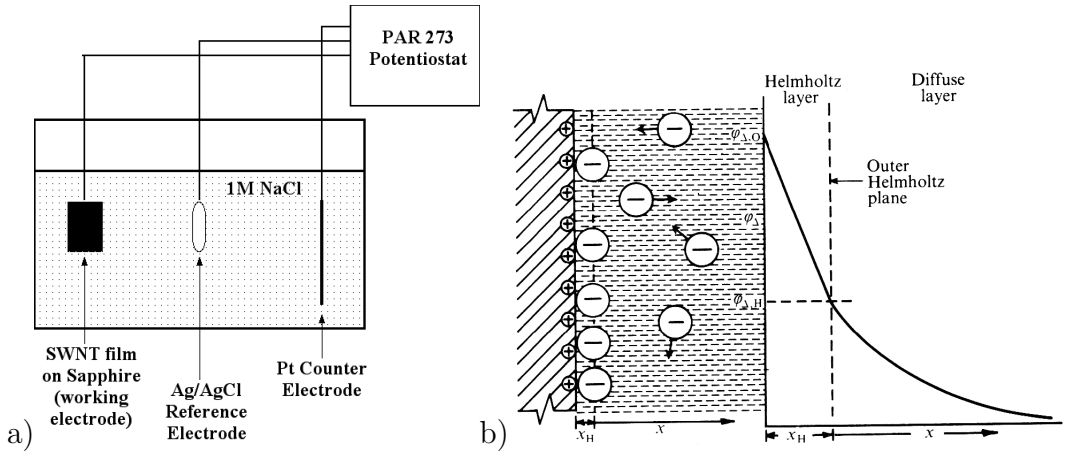

Figure 2.17. The electrochemical cell. (a) The three electrodes are connected to the potentiostat, which adjusts the potential at the counter electrode and measures the potentials at the working and counter electrodes with respect to the reference electrode. (b) The distribution of charges near the working electrode.

working electrode (the sample to be doped) results in a flow of electrons through the potentiostat circuit. In effect, the net result is that the negative ions at the sample surface have become electron acceptors. Thus a positive potential for the working electrode corresponds to hole doping and negative potential corresponds to electron doping.

Our electrochemical doping was done primarily with 1 Molar sodium chloride dissolved in deionized water. Sodium ions provide the positive carriers and chloride ions the negative carriers in the electrochemical cell. Because of the polar nature of water each ion carries with it a sheath of water molecules which partially screens the charge and attracts oppositely charged ions, making it difficult to calculate the total amount of charge added. The configuration of charges at the sample surface (working electrode) is often referred to as the charge double-layer,[2] and the potential difference between the working electrode and the solution is spread out over a region known as the Helmholtz layer (see Figure 2.17b).[2,48] Despite the complications due to the charge double-layer we can place an upper limit on the amount of charge added to the sample in this way. The current that flows depends on the total size of the working electrode, but it is typically on the order of milliamps for doping at 1 V. This current is sustained for a few minutes and then quickly drops to picoamps as the sample electrode becomes saturated. This

residual current is the result of charge transfer, via solvated ions, directly between the counter electrode and the small area platinum wire supporting the SWNT working electrode. If all of the nonresidual current corresponds to charges added to the nanotubes we obtain the following for the doping concentration under these conditions.

$$n = \frac{I}{e}\Delta t\frac{1}{V} \tag{2.13}$$

$$= (\frac{10^{-3}A}{10^{-19}C})(10^{2}s)(\frac{1}{1cm^{3}}) \tag{2.14}$$

$$= 10^{18}cm^{-3} \tag{2.15}$$

This gives an upper limit on the doping level as being equal to heavily doped semiconductors. However, the actual doping level is expected to be much lower than this because of the distribution of charge in the double-layer and the error in the current associated with nondoping charges that transfer directly through the contact electrode (the residual current). An analysis of the charge density in (6,5) and (7,5) nanotubes gives a valence electron density of only $10^{15}cm^{-3}$,[47] 1000 times smaller than the doping level we estimate from measurements of the doping current. To better estimate the number of charges we added we can use the Stern model for the effective capacitance of the charge double-layer.[48] In this model the charge density at the electrode surface is given by

$$\sigma = \sqrt{8\epsilon_r\epsilon_0 k_B T n_i^0}\sinh\left(\frac{zeV}{2k_B T}\right) \tag{2.16}$$

where ϵ_r is the relative dielectric constant of the solvent (for water $\epsilon_r = 78$), n_i^0 is the volume density in the bulk solution of the ions ($1M = 6.022 \times 10^{26}m^{-3}$), z is the number of elementary charges per ion ($z = 1$), and V is the electrochemical voltage. Since the surface to volume ratio for a cylinder is $2/r$ we calculate the density of added charges at ± 1 V to be $5.5\times10^{14}cm^{-3}$ assuming that the nanotubes are thoroughly wetted by the solution. This assumes a pure nanotube electrode. This model is expected to be especially accurate when using sodium chloride as the electrolyte because of the small size of the ions and their strong affinity for the polar solvent molecules (water).

2.5.2 I-V Characterization and Conductance

To measure the current-voltage dependence of various films and devices we used a computer controlled power supply to apply a fixed voltage across the sample while measuring the current. For a single conductance (resistivity) measurement only one voltage is needed. In order to characterize the conductance over a range of voltages the computer is used to scan the voltage over a fixed set of voltages and measure the current at each point.

2.6 Summary

In this chapter we have provided a detailed description of each of the important experimental techniques used in our study of SWNTs. The results of these experiments are discussed in the following chapters. We have described the core theoretical backgrounds for each technique, but detailed analysis will be given in connection with the particular results discussed hereafter. We have also attempted to describe several common challenges and pitfalls associated with these measurements. The careful student should be able to reproduce our experimental results by adhering to the procedures described above.

CHAPTER 3

ABSORPTION AND MODULATION SPECTROSCOPY OF SWNTS

3.1 Absorption of SWNT Films and Dispersions

The interaction of SWNT films with electromagnetic radiation depends, of course, on the frequency of the radiation. In the far infrared the absorption of SWNTs is dominated by Drude free-carrier absorption from carriers in both metallic and semiconducting tubes as well as low energy gaps in tubes of certain chiralities. In the near infrared and visible regions of the spectrum the absorption features are mainly due to the excitation of singlet excitons. In the ultraviolet the absorption of nanotube samples is dominated by the collective π-plasmon resonance common to many forms of carbon. We will discuss each of these regions of the spectrum along with the influence of doping and charge injection on the absorption features.

3.1.1 NIR-Vis-UV

In the near infrared (NIR), visible (vis), and ultraviolet (UV) regions of the electromagnetic spectrum the absorption of light by SWNTs is due to two main factors. First, optically active excitons are responsible for the various absorption peaks from approximately 0.4 eV to 3.2 eV.[22,25,26,49] As discussed in Chapter 1, these excitonic transition energies are dependent on nanotube size and chirality, so the exact energies vary from sample to sample. Second, there is a broad peak near 5 eV that is commonly associated with the π-plasmon,[50,51] which is the collective excitation of the π electrons in the SWNTs and other carbon structures (impurities) in a given sample.

The tendency of nanotubes to bundle together has an impact on the exact energies and shapes of the excitonic features in this region of the absorption spectrum. When nanotubes are bundled the Van Der Waals interaction between

them results in an inhomogenous broadening of the absorption peaks.[28] Therefore, the absorption of a collection of nanotubes in dispersions or solutions is quite different from that of a film of the same tubes. Furthermore, when tubes of different chirality exist in the same sample their absorption peaks may overlap. Even in films, though, one can increase the degree of separation of the nanotubes with a spacer material, such as the surfactants discussed in Chapter 2. Figure 3.1 shows the absorption spectra for two different films produced by the method described in Section 2.2 but which were subject to different degrees of sonication while in the suspension. In the nondispersed film the absorption peaks overlap significantly and there is little detail in the features. However, in the film dispersed with sodium dodecyl-sulfate (SDS) the absorption peaks are narrower and more resolved. Even in the well separated sample, individual tubes species may not be responsible for the small features, such as those near 1eV in the lower figure. The absorption spectrum from a film is always a combination of the (often broadened) absorption peaks from each of the tubes in the sample.

Figure 3.2 shows the visible and UV absorption for a film of SWNTs dispersed in SDS before and after annealing in a nitrogen atmosphere at $300°C$ for 6 hours. None of the excitonic features change with annealing, but the broad plasmon peak on which they sit does change. Upon annealing the plasmon peak decreases due to the disappearance of some of the carbonaceous impurities in the sample, and the resonance energy is red shifted. This is similar to the changes in the plasmon observed by other studies in which the absorption peak broadens and shifts with the introduction of defects in nanotube samples.[52] We conclude that annealing has little effect on the SWNTs themselves but helps reduce the impact of shortened tubes and nonnanotube carbon impurities in our film.

3.1.2 Infrared and THz

At energies below the exciton energies there is a broad absorption that generally increases with increasing wavelength (decreasing energy). Figure 3.3 shows the typical absorption of two films of SWNTs in the infrared. The upper spectrum is from a "paper" of nanotubes consisting of large bundles and a measurable amount of metallic catalyst impurities. The lower spectrum is from a thin film of SWNTs

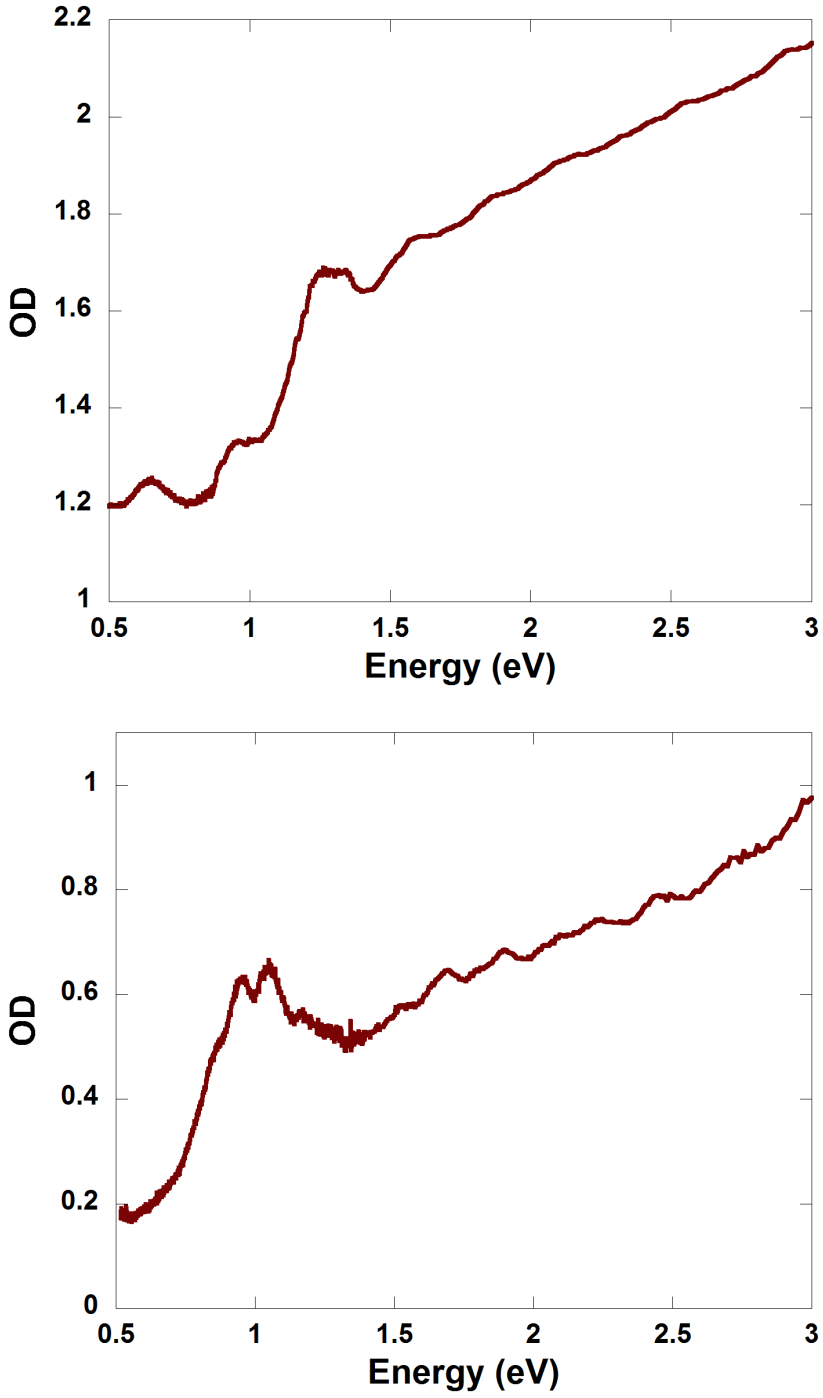

Figure 3.1. Typical absorption spectra for two SWNT films. The upper spectrum corresponds to a film in which the nanotubes are in large bundles, and the lower spectrum corresponds to smaller bundles and more isolated tubes.

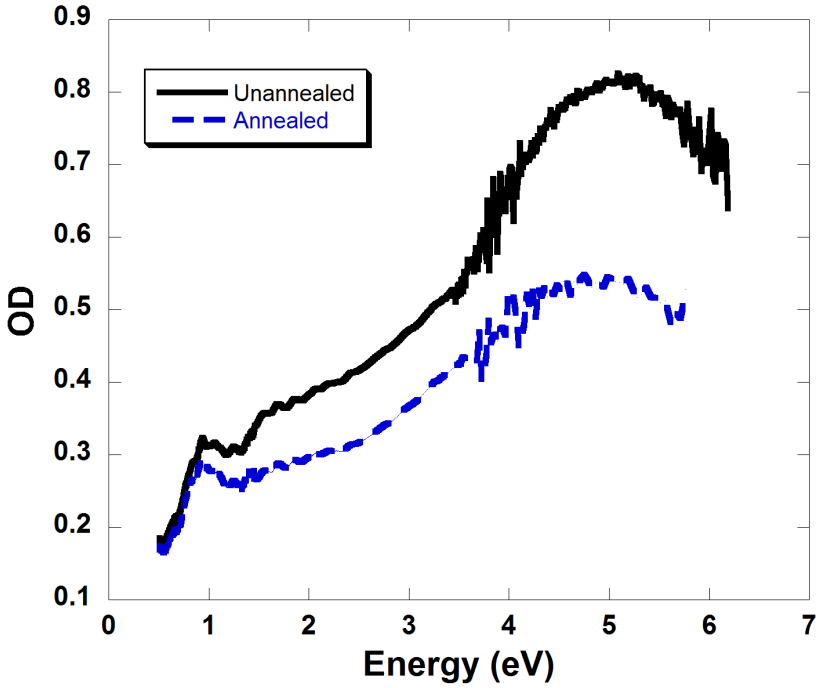

Figure 3.2. Absorption spectra before (solid) and after (dashed) annealing at $300°C$ for 6 hours.

dispersed in SDS surfactant. The sharp absorption peaks near 0.35 eV correspond to the surfactant. In both samples the absorbance increases sharply below 0.2 eV.

The shape of the absorption of SWNTs in this region follows the predicted absorption of free charge carriers according to the Drude model (see Chapter 6 of[53] for a derivation). The Drude model predicts an absorption coefficient for free carriers in semiconductors as follows:

$$\alpha(\omega) = \frac{\varepsilon_\infty \omega_p^2 \gamma_c}{n_r c(\omega^2 + \gamma_c^2)} \tag{3.1}$$

$$\omega_p = \sqrt{\frac{Ne^2}{\varepsilon_0 m^* \varepsilon_\infty}} \tag{3.2}$$

In these expressions ε_∞ is the local dielectric constant that is responsible for screening the free carriers from each other, ω_p is the plasma frequency, N is the carrier density, n_r is the real index of refraction, c is the speed of light, and γ_c is the scattering rate of the carriers. At high frequencies the free-carriers absorption tends to zero, while at low frequencies it rises and then approaches a zero-frequency limit given by

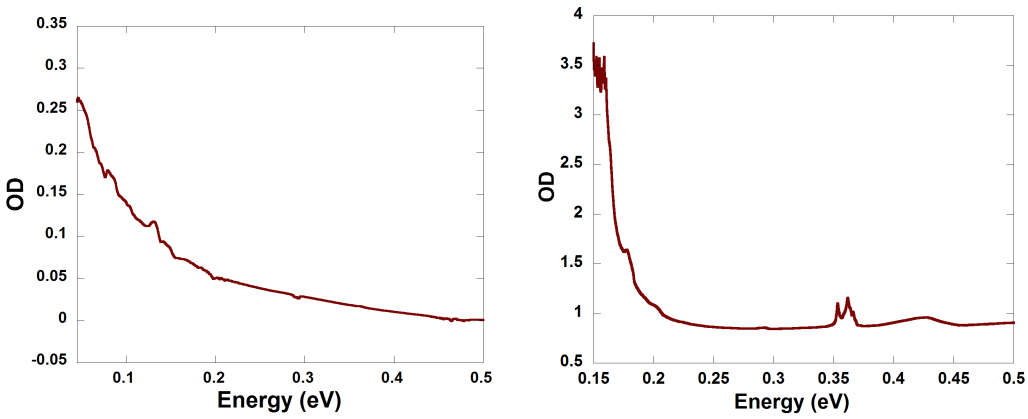

Figure 3.3. Typical absorption spectra for two SWNT films. The left spectrum corresponds to a film in which the nanotubes are in large bundles, and the right spectrum corresponds to smaller bundles and more isolated tubes. The features in the more isolated sample near 0.35 eV are due to IRAV of the surfactant.

$$\alpha_0 = \frac{Ne^2}{\varepsilon_0 n_r c m^* \gamma}. \tag{3.3}$$

Note that there are no IR-active vibrations (IRAV) in the spectrum other than those that belong to C-H stretching in the surfactant. There are some theoretical[24,54] and experimental[55] evidences for a low energy absorption peak in nanotube samples due either to a curvature-induced gap or intertube effects in bundles. However, the fit of our data to a Drude model in the spectral region shown in Figure 3.4 is essentially unaffected by the addition of a low energy Lorentzian term (i.e., the fit parameters for the Drude portion are changed less than a percent). This suggests that the oscillator strength of the pseudo-gap, if it exists in our samples, is much less than that of the free carriers.

3.2 Absorption of Electrochemically Doped SWNTs

Monitoring the absorption while doping is an important tool for understanding how doping influences the electronic properties of SWNTs. We electrochemically doped films of nanotubes and obtained their absorption spectra following the processes discussed in Chapter 2. We primarily used sodium chloride (NaCl) as the electrolyte due to its availability and lack of absorption in the range of interest, but the results are qualitatively the same with other electrolytes.

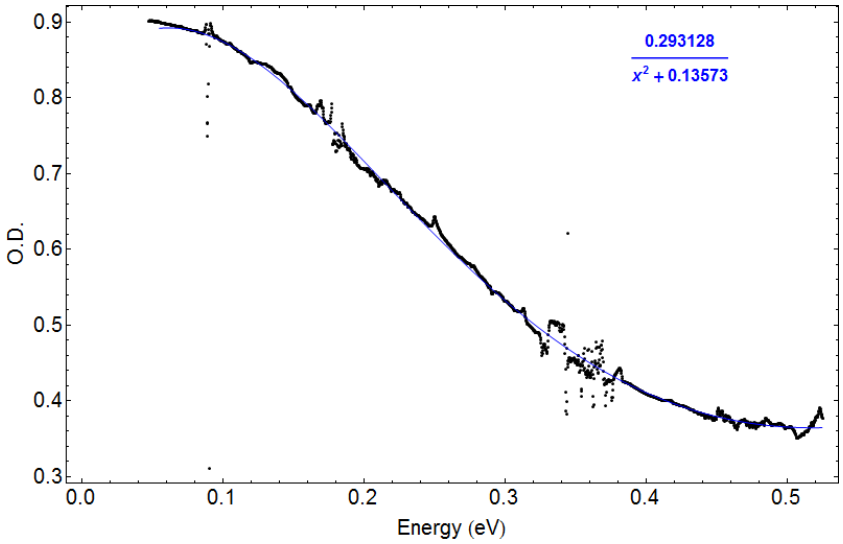

Figure 3.4. Infrared absorption of a film of SWNTs. The points correspond to the data and the solid line corresponds to a fit to the Drude model for free carriers absorption. The nonlinear fit parameters are shown, corresponding to a relaxation rate of 0.266 eV or about 64 THz.

Figure 3.5 shows a broad range absorption spectrum for a film of nanotubes before and after electrochemical doping. The absorption above 0.5 eV is bleached upon electrochemical doping and the absorption in the IR is enhanced. The peaks from the IRAV of the surfactant remain unchanged relative to the FCA background. We will discuss the behavior of each region of the spectrum in detail in the following sections.

3.2.1 NIR-Vis Absorption

As mentioned above, the absorption features in the NIR-Vis region of the spectrum are due to two phenomena. First, individual excitonic transitions are responsible for the relatively sharp absorption peaks. Second, the collective π-plasmon resonance, which is present in nanotubes as well as other carbon materials in the sample, is primarily responsible for a broad Lorentzian peak near 5 eV. Its tail forms a rising background on which the excitonic peaks sit. Electrochemical doping modifies both of these features. In general, electrochemical doping bleaches the NIR-Vis absorption of SWNT films.

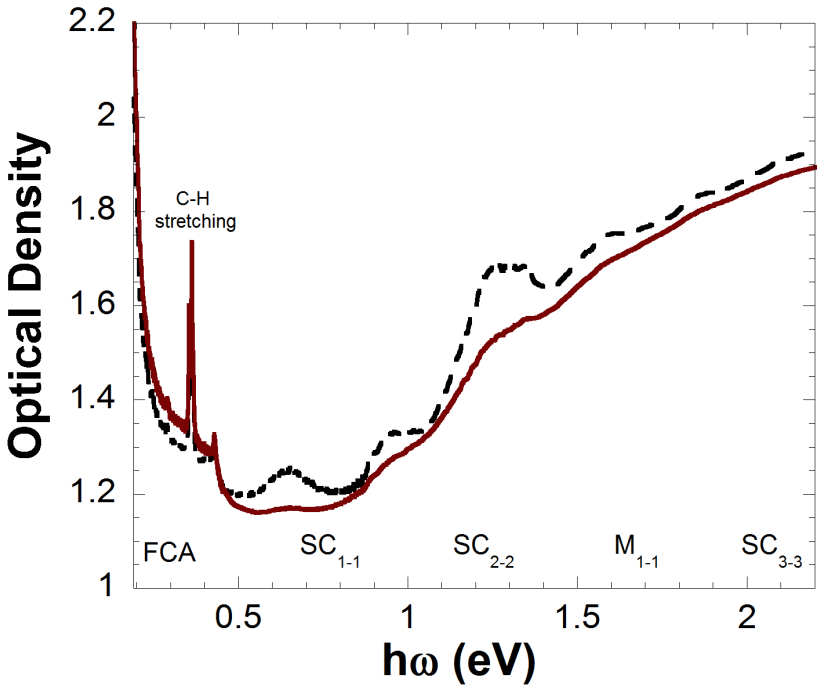

Figure 3.5. Absorption spectra before (dashed) and after (solid) electrochemical doping at $+1.5V$ in 1M NaCl. The excitonic transitions for semiconducting (SC) and metallic (M) species are shown, as well as the region corresponding to free-carriers absorption (FCA).

3.2.1.1 π-plasmon Resonance

Figure 3.6 shows the absorption of a relatively disperse nanotube sample before and after electrochemical doping. The spectra have not been normalized in any way, so the absence of any change in optical density at 0.5 eV indicates that the dopant has not introduced any additional scattering or other systematic offset. The sharp absorption features due to excitons are bleached with doping, but the greatest change in the film's absorption is near 2.0 eV. However, that corresponds to the region of excitonic transitions belonging to the metallic tubes in the sample which should be minimally affected by the addition of charge. Therefore, it is likely that the reduction in absorption in this region is due primarily to a change in the plasmon absorption.

The π-plasmon in bundles of carbon nanotubes has been shown to depend on the size of the tubes, the degree of bundling, and the local dielectric of the bundles.[50] Each of these may change with electrochemical doping. First, as discussed in Chapter 4, the size of the nanotubes themselves may change with doping due to electrostriction of the lattice. Second, if there is any intercalation between the tubes by the dopant or charge transfer among the tubes in a bundle then the proximity of the tubes will change. Finally, the dopants themselves will certainly change the local dielectric for the nanotubes as they adhere directly to the tube surfaces.

Unfortunately, attempts to fit absorption spectra to a combination of Gaussian peaks for individual nanotube transitions and a Lorentzian peak for the plasmon are unsatisfactory and inconclusive. The (largely unknown) degree of broadening in the exciton peaks and the fact that they sit on the tail of the plasmon peak make the fit extremely sensitive to starting values. Attempts have been made by other groups to fit the plasmon peak in order to quantify the purity of SWNT samples.[56] Such techniques are useful for characterizing the purity of a sample when the absorption is known over a very large spectra range that includes the majority of the plasmon peak. However, it has not been shown to be helpful when characterizing individual absorption peaks. Therefore, we have used a simple third-order polynomial to fit the plasmon background in the low energy region of the spectra which correspond to the excitonic transitions.

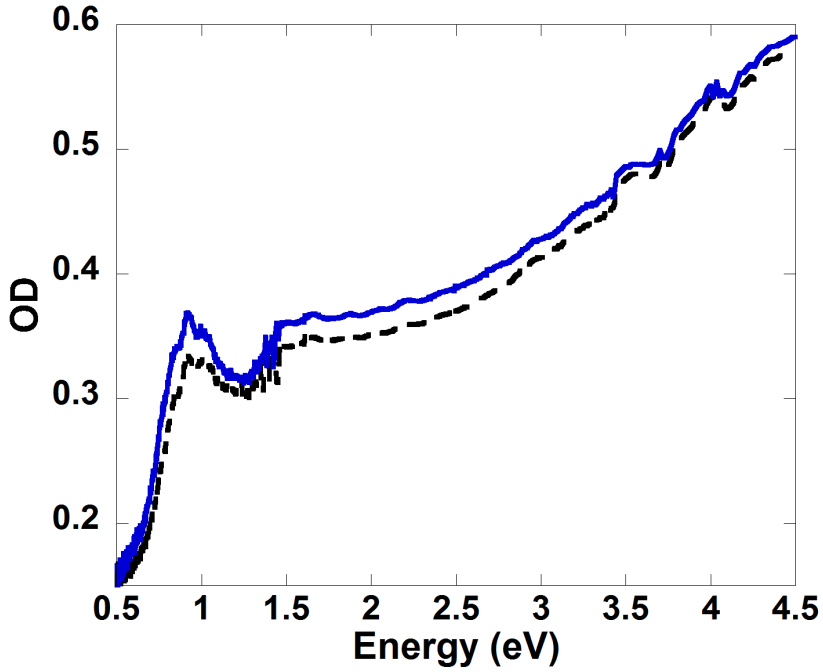

Figure 3.6. Absorption spectra before (solid) and after (dashed) electrochemical doping at $+1V$ in 1M NaCl. The change in the excitonic absorption peaks is much larger than the change in the π-plasmon background.

3.2.1.2 Excitonic Transitions

Figure 3.7a shows the excitonic absorption peaks at several different electrochemical doping potentials for a SWNT film consisting of a narrow diameter distribution ($\approx$ 1.2 nm). The regions of the spectrum corresponding to semiconducting (SC) and metallic (M) excitonic transitions for the corresponding diameter distribution of tubes are labeled. Negative potentials correspond to electron doping and positive potentials to hole doping. The small wiggles near the peak of the SC_{2-2} region are due to instrument noise and are not physically significant. These spectra have not been normalized to any particular point, so the correspondence of the spectra below 0.6 eV is validation that the changes we see are due purely to the electrochemical modulation and not to increased scattering by the dopant ions.

For small negative potentials the absorption in this region is enhanced relative to the pristine sample, but for larger negative potentials (≈ -0.8 V), and for all positive potentials, the absorption is bleached. The general effect is summarized

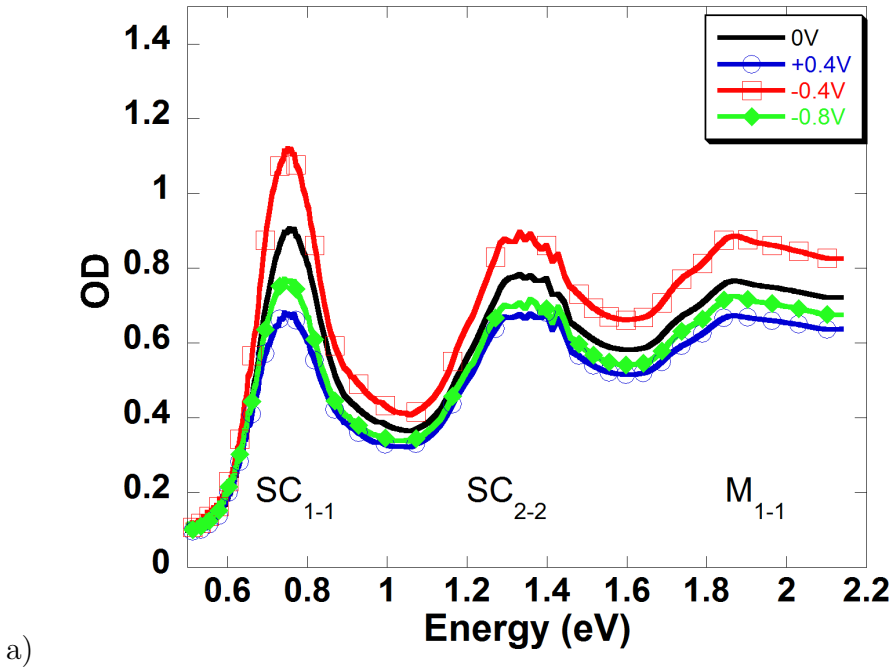

a)

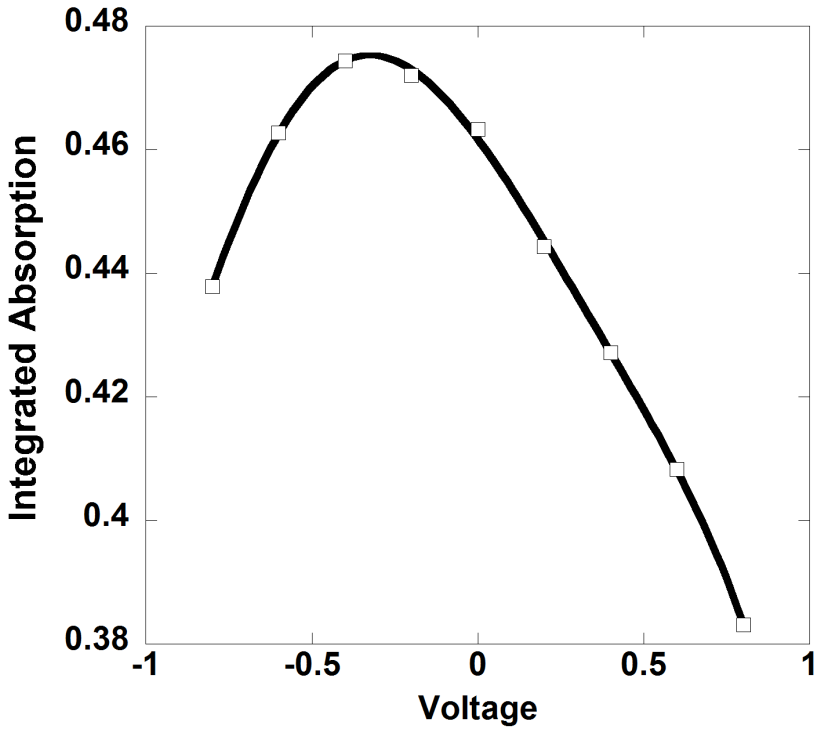

b)

Figure 3.7. Electrochemically induced changes in the absorption of a SWNT film at various potentials vs Ag/AgCl in 1M NaCl. a) Absorption spectra. b) Integrated optical density over the spectral region shown.

in Figure 3.7b in which the integrated signal (total optical density) is plotted as a function of doping potential. The overall absorbance in this region attains a maximum at a doping potential of ≈ -0.4 V. This apparent asymmetry between electron and hole doping is due to the curvature-induced intrinsic hole-doping in SWNTs. According to[57] the curvature of the nanotube walls mixes the π and σ hybridized orbitals and results in a transfer of charge from the π electrons that make up the valence band to the σ orbitals that form the lattice. The effect is that the nanotubes, even those that are metallic, are inherently p-type and low density electron doping compensates the intrinsic holes. We will elaborate on this point when we explain the effect of doping on the excitonic transitions below.

One experimental verification of this intrinsic doping compensation is the modification of the conductivity of a SWNT sheet by electrochemical doping. Figure 3.8 shows the resistance of a free-standing nanotube paper as a function of electrochemical doping potential. The resistance has a maximum around -0.4 V vs Ag/AgCl in 1M NaCl, corresponding to the maximum optical absorption in Figure 3.7. Thus, at -0.4 V the doped electrons have fully compensated the intrinsic holes and the π valence band is full and the conduction band is empty, so there is a minimum density of carriers to conduct electricity. At larger negative potentials the increased electron density begins to fill the conduction band and the conductivity increases while the absorption decreases.

The fractional changes in the absorption at several different points in the spectrum are shown in Figure 3.9a. However, as mentioned earlier, the spectral region in Figure 3.7 contains absorptions from individual excitonic transitions as well as from the π-plasmon. We modeled a background in each of the spectra in Figure 3.7a by fitting a simple curve to the local minima. We then subtracted this artificial background and compared the peak absorptions at various doping potentials. The results are shown in Figure 3.9b. This analysis is a conservative estimate since it ignores the influence of the tails of the absorption peaks at the local minima. The absorption of the S_{1-1} exciton is affected most, followed by the S_{2-2} exciton. The metallic exciton is practically unaffected. The explanation for this effect involves three phenomena: exciton screening, k-space filling, and band renormalization.

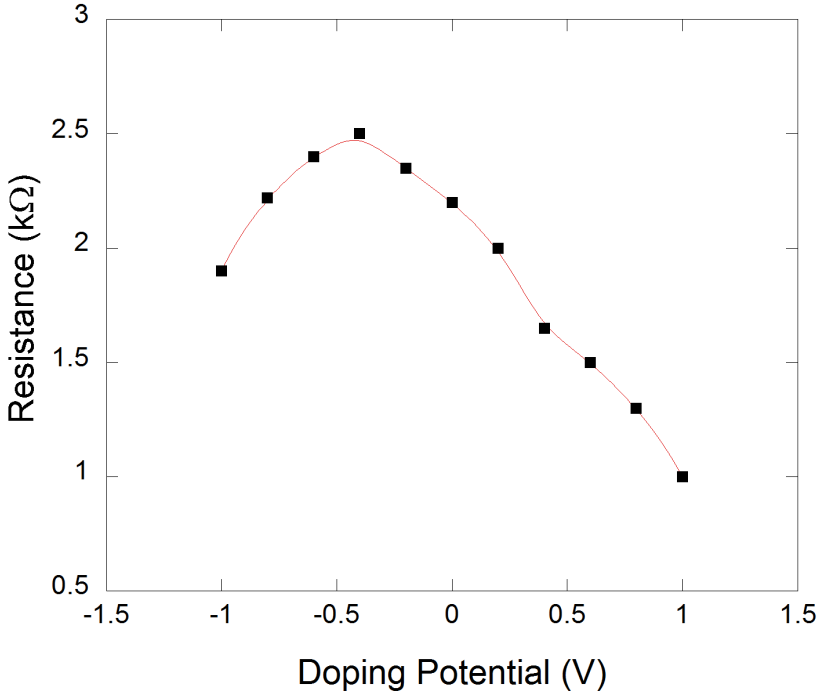

Figure 3.8. Resistance of a SWNT paper after electrochemical doping at various potentials vs Ag/AgCl in 1M NaCl. The resistance has a maximum when the density of carriers is a minimum at a doping potential of -0.4 V.

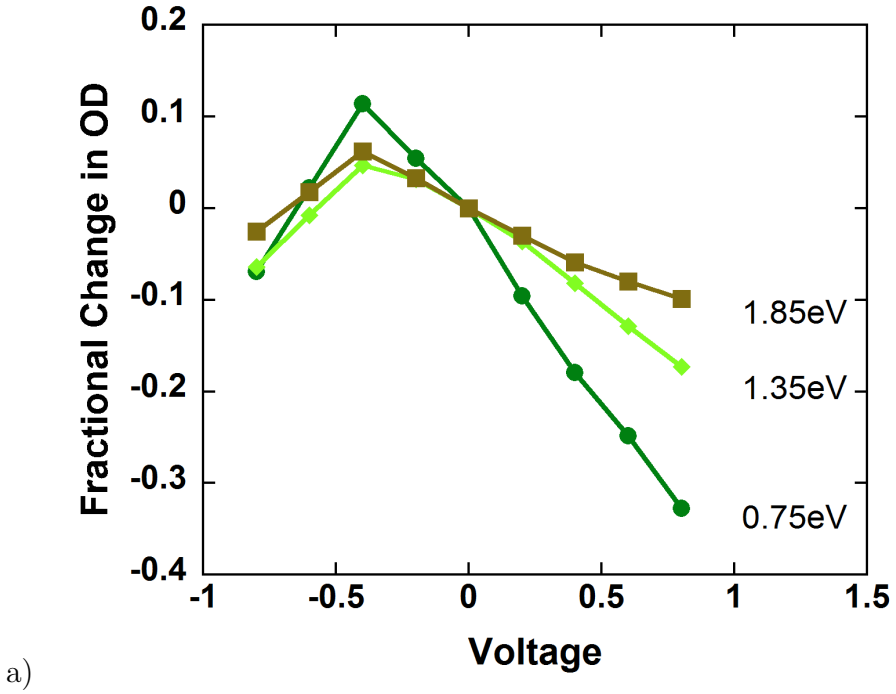

a)

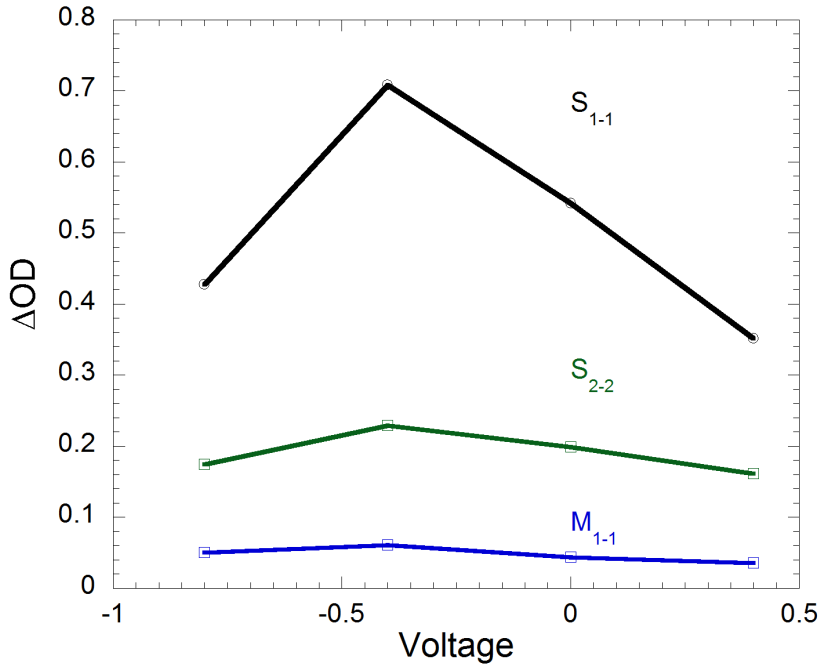

b)

Figure 3.9. The change in absorption at three different resonances in Figure 3.7. a) Fractional change in overall absorption of the three absorption peaks. b) Total change in optical density after subtracting the plasmon background.

3.2.1.3 Exciton Screening

The interaction between an electron and its corresponding hole in an exciton is primarily Coulombic in nature. Therefore, the modification of the surrounding dielectric results in a change in the average distance between the electron and hole as the Coulomb interaction between them is screened by the surrounding charges. The effective Bhor radius for a three-dimensional exciton is

$$a = \frac{\hbar^2 \epsilon}{\mu e^2} \tag{3.4}$$

where ε is the local dielectric constant and μ is the reduced mass of the electron-hole system.[58] The effective radius in one or two dimensions is more complicated and depends on the geometry of the system. However, the general behavior is the same. As the dielectric constant increases (as with the addition of free carriers) the size of the exciton increases. This decreases the binding energy and causes the oscillator strength to decrease as the square of the dielectric constant according to the following (also from[58] for the lowest energy transition: $n = 1$).

$$|\phi(0)|^2 = (\pi a^2)^{-1} \tag{3.5}$$

$$\Rightarrow f \propto \epsilon^{-2} \tag{3.6}$$

This screening of the excitons due to the modification of the surrounding dielectric is the reason that the S_{2-2} exciton in the spectra in Figure 3.7 is affected by the doping. The addition of carriers to the nanotubes screens *all* of the excitons so that their oscillator strength decreases. For the metallic tubes, however, the local carrier density is already high (and the binding energy is lower than the s-SWNTs[27]) so the addition of charges has a much smaller effect in that case.

3.2.1.4 Band Gap Renormalization

If exciton screening were the only effect of the electrochemical doping then we would expect to observe a blue shift of the exciton transitions, which we do not. In fact, the fits of the absorption peaks in Figure 3.7 to Gaussian profiles shows a very small red shift, though the shift is less than our experimental uncertainty of 10 meV. A similar effect was observed in a related study[3] where the dielectric surrounding the nanotubes was changed by changing the relative humidity of

the tubes' environment. In highly correlated systems like SWNTs one major effect of the strong electron-electron interactions is the renormalization of the band gap to smaller levels. This band gap "shrinkage" is a direct result of the Coulomb interaction among carriers, and strong evidence for carrier-induced band-gap renormalization in SWNT transistors has been observed.[59] In our electrochemically doped absorption spectra we observe a decrease in exciton oscillator strength but no apparent shift in exciton transition energy because the effects of band-gap renormalization compensate for the shift in exciton binding energy as shown schematically in Figure 3.10.

3.2.1.5 k-space Filling

Finally, the fact that the lowest energy transitions (S_{1-1}) are the most affected by doping leads us to conclude that band filling plays an important role in the observed changes in absorption. If the observed absorption features were due to interband transitions we would expect that the filling of the conduction band (or depletion of the valence band) would lead to a reduction in absorption as the authors of[60] propose because the additional charges occupy the allowed energy levels within the band. However, we would expect that the absorption peaks would disappear in sequence as the doping level increases. For example, at room temperature the Fermi distribution function is sufficiently steep that the S_{2-2} transition should not be noticeably affected by the filling of the first conduction band. Because the absorption is excitonic, though, the introduction of additional carriers fills the momentum space in a process called k-space filling.

The exciton bound states are made up of linear combinations of direct products of electron and hole momentum eigenstates with the same value of the momentum; the electron and hole scatter off of each other in momentum space as the exciton propagates in the lattice. However, each free carrier occupies a certain energy eigenstate corresponding to a particular value of the momentum. As free carriers are added to the lattice there are fewer and fewer momenta allowed for the excitons to exist and so the formation of excitons from electrons with energies closest to the Fermi energy is suppressed. This phenomenon has been investigated in two-dimensional quantum wells[61] where it was shown that the k-space filling caused

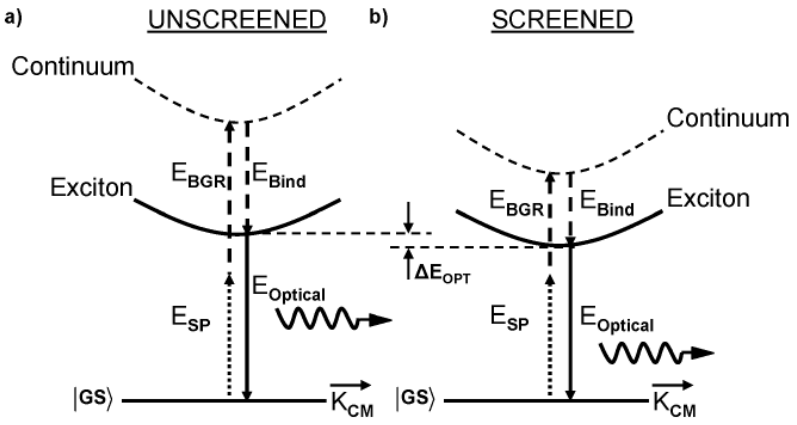

Figure 3.10. The combined effect of exciton screening and band gap renormalization. The two effects are each of the order of the exciton binding energy and tend to compensate one another so that the shift in the exciton transition energy is small - after[3]

the lowest energy excitons to be suppressed by a factor of ten with respect to the suppression of higher energy excitons. This is in agreement with the difference between the S_{1-1} and S_{2-2} curves in Figure 3.9b. In our experiment the S_{1-1} peak is suppressed by a factor of 7.8 with respect to the suppression of the S_{2-2} peak when we compare the zero-charge absorption (-0.4 V doping) with the charged absorption (1.0 V doping).

3.2.2 Infrared and THz

The increase in the infrared absorption behaves similarly to the decrease in exciton absorption upon electrochemical doping. The upper plot in Figure 3.11 shows the absorption in the infrared of a film of SWNTs before and after doping along with the edge of the S_{1-1} exciton transition for that sample. By fitting the spectra to the Drude model for free carriers absorption we find that the scattering rate has increased in the doped sample. The lower graph in Figure 3.11 shows only the free-carrier absorption edge, corrected for the reflectance, of a film of SWNT before and after doping along with the fit to the Drude model discussed above. The scattering rate γ_c increases from 0.266 eV (64 THz) in the undoped sample to 0.368 eV (89 THz) in the doped sample.

Furthermore, we measured the extreme far-infrared absorption of SWNTs be-

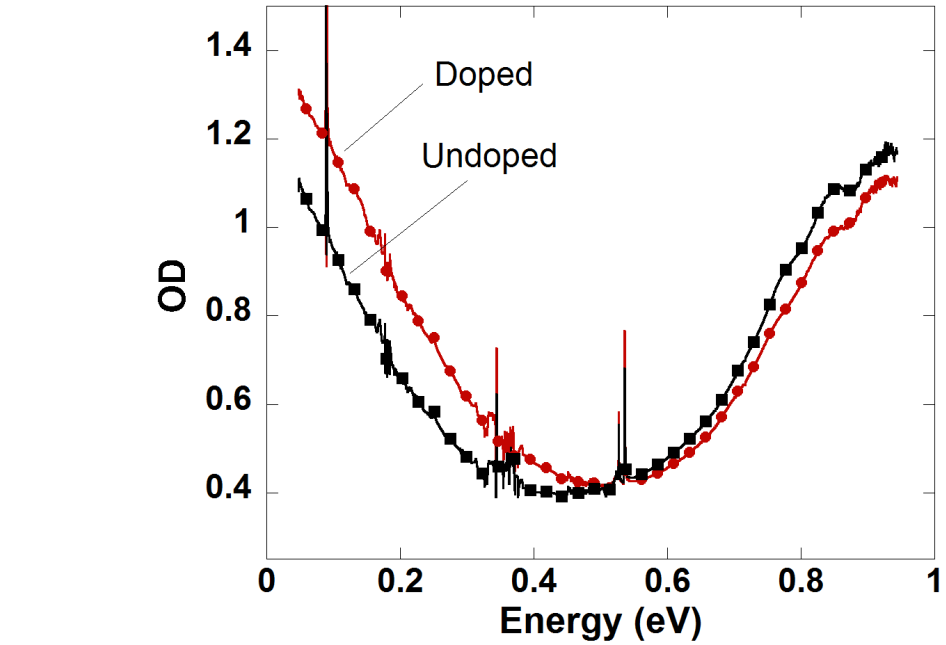

a)

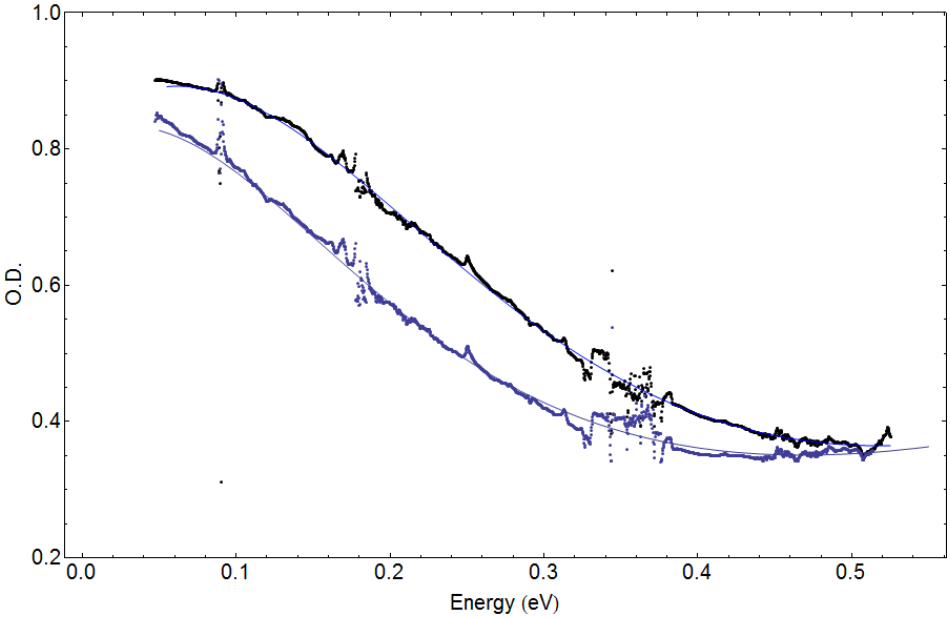

b)

Figure 3.11. Infrared absorption of SWNTs with and without electrochemical doping. a) Absorption before (squares) and after (circles) doping at $+1V$ vs Ag/AgCl. As the exciton absorption decreases the free-carriers absorption increases. b) Absorption before (lower) and after (upper) doping. The Drude fit is the solid line passing through the data points. The scattering rate γ_c is 0.266 eV for the lower curve and 0.368 eV for the upper curve.

fore and after electrochemical doping. Figure 3.12 shows the absorption spectrum from 0.1 to $1.0THz$. Because the THz spectroscopy is a complex measurement requiring many hours per spectrum (see Chapter 2 for details), a detailed comparison of different doping levels is impractical. Discussion of this point continues in the Time Evolution section below. However, we can compare the low frequency absorption before and after doping to quantify the change in the plasma frequency ω_p. The results are similar to those obtained in the mid-IR using the FTIR spectrometer in that the free-carriers absorption in the asymptotic limit increases with added carriers. Above $0.7THz$ the absorption decreases according to the Drude model. However, below $0.6THz$ the absorption levels off, indicating that the conductance of our sample is essentially flat with respect to frequency up to that point. The ratio of the low frequency plateaus is 1.9. If the sample consisted purely of semiconducting tubes this would indicate that the number of carriers in the sample has approximately doubled with the electrochemical doping. The plasma frequency in metals, however, is unaffected by changes in the Fermi level. Therefore we estimate that the doped carrier density in the semiconducting tubes in our sample is on the same order as the carrier density in the metallic tubes, which is $\approx 10^{15} cm^3$.

3.2.3 *Ex-Situ* Time Evolution

As discussed in Chapter 2, the nature of the charge injection in electrochemical doping is relatively complex. To better understand the doping induced changes we measured the absorption at various times after removing the nanotube from the electrochemical cell. The sample was doped at a fixed voltage for several minutes then removed, rinsed, and dried in nitrogen. The sample was then placed in the spectrometer and left there for up to several days. Figure 3.13 shows the absorption spectrum of a film of SWNTs after electrochemical doping. When the film is p-doped (a) the absorption of each exciton peak decreases. Over time red-ox reactions in air reduce the doping level and the absorption increases. However, under standard temperatures and pressures the doping effect never disappears completely as evidenced by the asymptotic limit that is still below the pristine level. In n-doping (b) the opposite occurs. This is indicative of the inherent

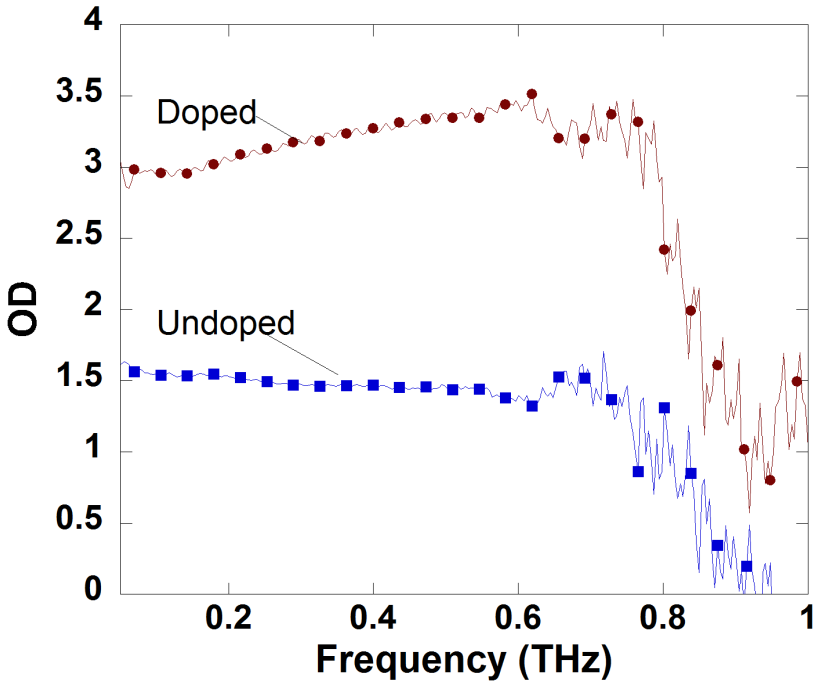

Figure 3.12. Infrared absorption before (squares) and after (circles) electrochemical doping at $+1V$ vs Ag/AgCl.

nature of the doping asymmetry with respect to the PZC. The pristine tubes are p-type, so n-doping enhances the exciton absorption and red-ox reactions in the atmosphere that remove the electrochemical charge double-layer simply push the tubes back toward their pristine state.

Surprisingly, there is a substantial effect remaining after many hours in air. Figure 3.14 shows the fractional change in integrated absorption over the spectral range of $0.5 - 2.5$ eV over two days. The influence of the doping decreases with time, but it asymptotically approaches a nonzero limit. The time constant of the decay of the doping effect, calculated by fitting an exponential decay to the data, is roughly the same for negative and positive doping potentials (decay constant of approximately $2/hr$). We found some dependence in the time evolution on sample thickness. Generally, thicker samples had longer time constants than thinner samples. However, we did not specifically measure the thickness of the films used for these spectra; the assessment comes from the overall optical density.

This effect is relatively unique and is due to the very high capacitance of

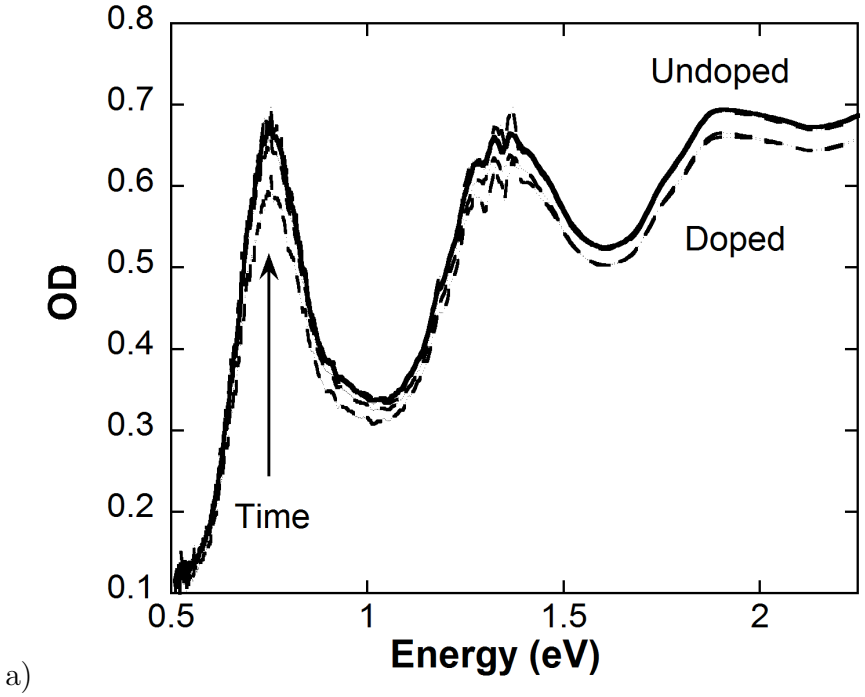

a)

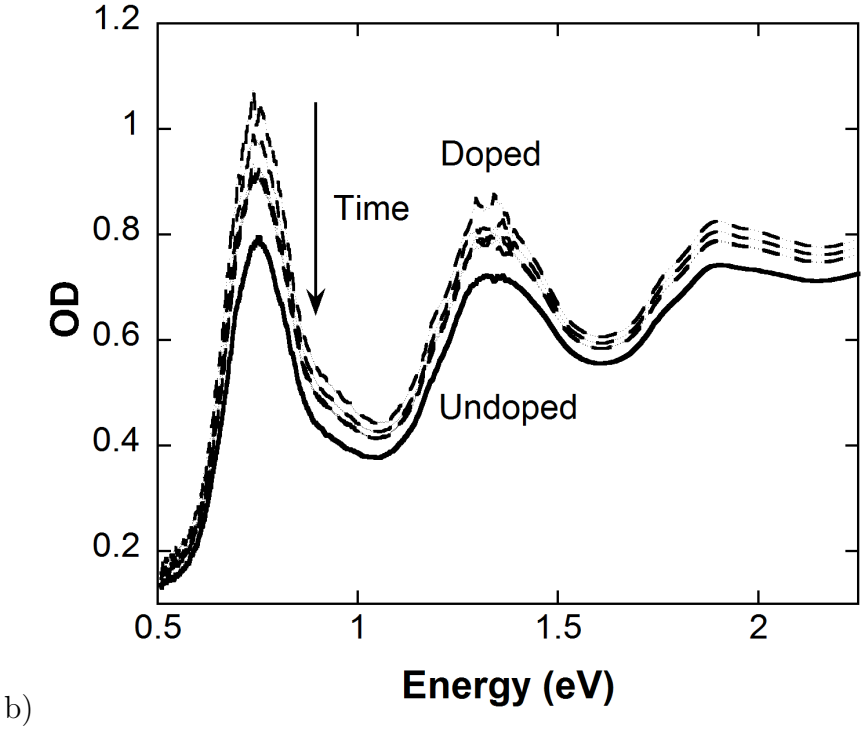

b)

Figure 3.13. Time evolution of the absorption spectrum after electrochemical doping. (a) Negative doping followed by a gradual decrease in the absorption. (b) Positive doping followed by a gradual increase in the absorption.

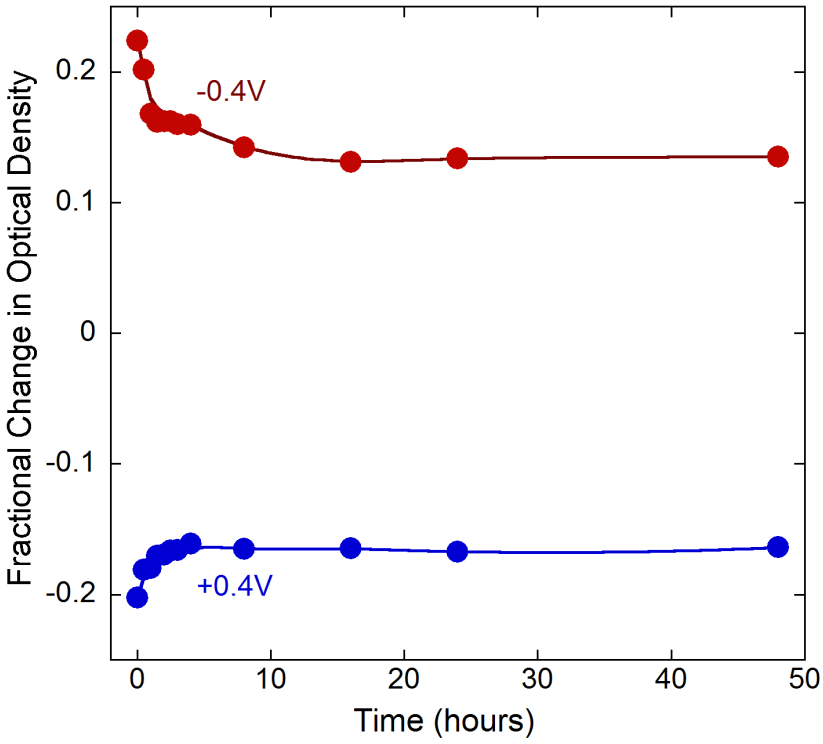

Figure 3.14. Time evolution of the fractional change in integrated optical density in the NIR-Vis region for electron (upper) and hole (lower) doping.

SWNTs because of their large surface to volume ratio. In other materials the charge double layer disappears quickly due to evaporation of the solvent and/or red-ox reactions in air. Typically, electrochemical doping that is robust at standard temperature and pressure is due to intercalation of the doping ions into the lattice of the sample. However, there is no hysteresis at all in the effects we measure. A nanotube film may be doped repeatedly at positive and negative voltages and the same spectroscopic effects are always observed at the same values of the doping potential. Therefore no measurable intercalation has occurred (else there would be some energy associated with getting the ions into and out of the lattice[18]).

3.2.4 Discussion

As indicated in the introduction in Chapter 1, early attempts were made to understand optical excitations in SWNTs by a tight-binding model for the quasi-one-dimensional band structure. In such a model, electrochemical doping would result in a quenching of band transitions due to filling or depleting the density of states in the conduction and valence bands, respectively. However, we now know that the optical excitations in the NIR-Vis region are due to excitons. This allows for a better understanding of the effects of electrochemical doping on the absorption of nanotube films. Added carriers, whether from electrochemical doping or direct injection, screen the bound electron-hole pairs thereby reducing their binding energy and their oscillator strength. However, the reduction in the exciton binding energy is compensated by the carrier-induced band gap renormalization. Furthermore, the k-space filling by the added carriers bleaches the lowest energy transitions by almost a factor of ten more than higher energy transitions. Simultaneously, the increase in carrier density shifts the Drude edge by changing the plasma frequency and scattering rate, and this results in an enhancement of the infrared absorption for doped samples.

A complication in our analysis is the influence of doping on the plasmon resonance. Electrochemical doping has a strong effect on the plasmon signal; it is bleached when charges are added relative to the zero-charge (hole-compensated) doping levels. However, there is little indication that direct charge injection has the same effect (see the next section below). Therefore it is likely that the primary

influence on the plasmon resonance is through changes in the tube and bundle sizes that occur in the presence of the doping ions.

Of central importance in understanding the effects of doping is knowing the doping level. Each of our measurements provides a way to calculate the number of additional charges that we have introduced. From the doping current we estimate an upper limit on our doping level as $10^{18}/cm^3$ (see Chapter 2). However, from the changes in the plasma frequency (a factor of 1.9) and the changes in the conductivity (a factor of 2.5) we estimate that the maximum doping level we achieved through electrochemical doping was in fact equal to the undoped carrier concentration of $\approx 10^{15}/cm^3$.[47] Therefore we conclude that the actual doping concentration is around $10^{15}/cm^3$ and that only a fraction of the current in the electrochemical cell actually contributes to doping the tubes. This is in agreement with our calculations following the Stern model discussed in Chapter 2.

3.3 Charge-induced Absorption

To further investigate the effect of charging SWNTs on the optical properties we measured the charge-induced absorption (CIA) of a film of SWNTs dispersed in PVA as described in Chapter 2. The CIA spectrum in the IR-Vis range is shown in Figure 3.15a. For comparison, the absorption of the same sample is shown in Figure 3.15b. The effect of directly injected charges is similar to the effect of electrochemical doping in that the absorption belonging to semiconducting transitions is bleached while the absorption of metallic excitons is essentially unchanged. There is pronounced bleaching of the absorption between 0.6 eV and 1.6 eV as well as above 1.8 eV. There is little or no change in the absorption in the small portions of the spectrum around 0.5 eV, below the lowest exciton, and 1.7 eV, the energy of the 1-1 metallic excitons in our sample. Between 0.49 eV and 0.55 eV the charge-induced absorption is essentially zero, while below 0.49 eV there is enhanced absorption corresponding to the increase in free-carriers absorption. Above 0.5 eV there are several small features that are not directly correlated with features in the absorption. These may reveal a variation in individual tube responses or a higher efficiency of charge injection in certain species.

There are two main differences between the CIA and the electrochemically

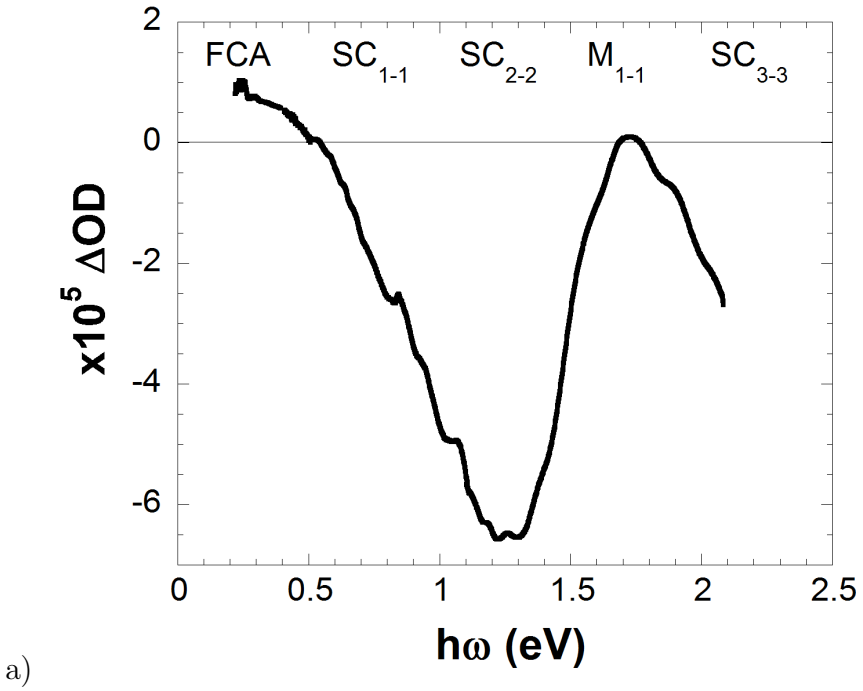

a)

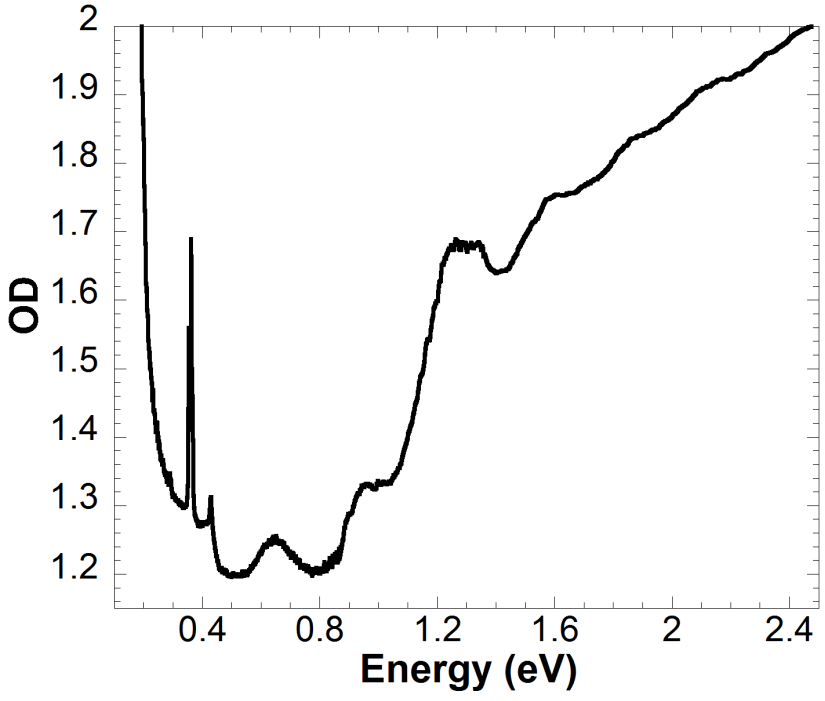

b)

Figure 3.15. Charge-induced absorption in a unipolar device. (a) CIA spectrum. (b) Sample absorbance.

doped samples. First, there is no broad offset in the CIA signal as would be the case if the π-plasmon were affected by the injected charges. As mentioned in the previous section, this is evidence that the π-plasmon is practically unaffected by the injected charges and is only sensitive to changes in the morphology such as we expect for electrochemical doping. Second, the S_{2-2} transitions seem to be bleached *more* than the S_{1-1} transitions. This effect is probably due to the fact that there is significant overlap between the S_{1-1} and S_{2-2} transitions in this sample because the diameter distribution is broader than for the samples studied by electrochemical doping. Smaller diameter tubes have higher exciton energies but also have higher levels of intrinsic hole-doping. Thus, their electron affinity is higher and electrons may be injected preferentially into smaller diameter tubes. This would skew the observed bleaching of the lowest level transitions to energies that would overlap with the S_{2-2} transitions of other tubes in the sample.

Figure 3.16 shows the I-V curve for our device and the voltage dependence of the CIA signal at various photon energies. The CIA signal increases with increasing applied voltage up to around $8V$. Above this value the increase in CIA signal is very small, indicating a saturation of the effect. This saturation may be due to enhanced intertube charge transfer to the metallic tubes at high carrier densities, or it may be due to a transition to a different injection mechanism that prevents the further build up of charge in the tubes.

3.3.1 Discussion

In summary, CIA shows bleaching of semiconducting excitonic transitions, but no effect on metallic transitions, in agreement with our results for electrochemical doping. The effect of the injected charges on the plasmon resonance is unknown, but it clearly shows no shift at the metallic transition energy. The saturation of the CIA signal (Figure 3.16b) may be an indication of a change in the injection mechanism at large bias voltages. The voltage dependence of the CIA signal is similar in each region of the spectrum: the free-carriers absorption, the low energy semiconducting excitons, and the high energy semiconducting excitons. It is possible that a few conduction channels made up of primarily metallic tubes begin to dominate the conduction above $8V$, thereby suppressing further charge

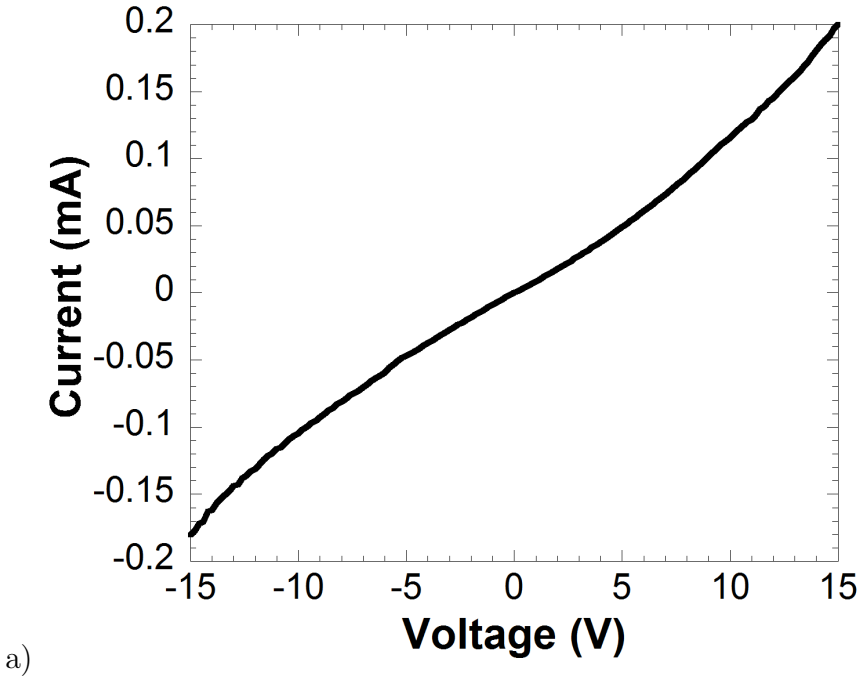

a)

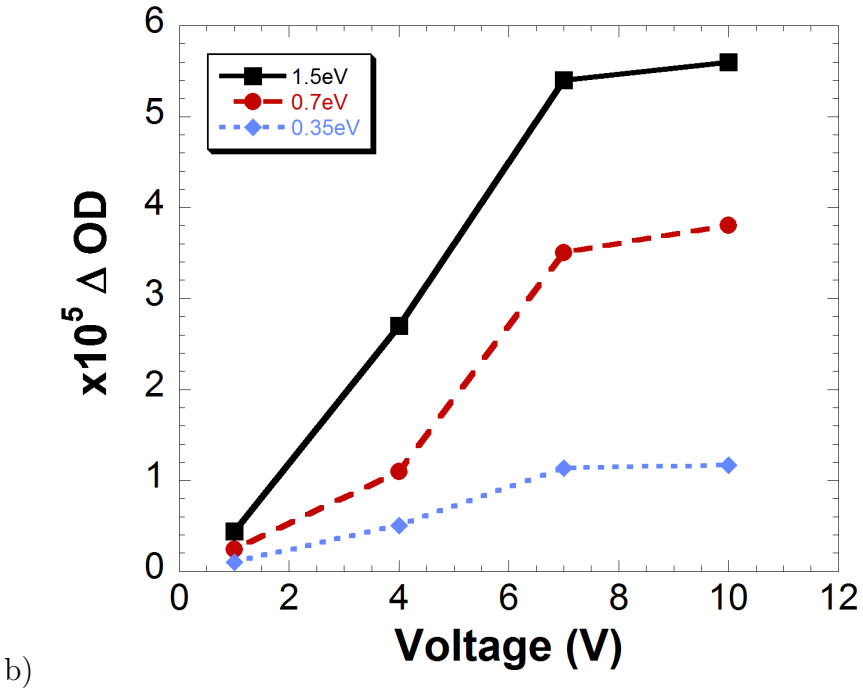

b)

Figure 3.16. Current characteristics of the CIA device. (a) I-V curve for the device. (b) CIA signal as a function of bias voltage for several points in the spectrum.

injection into the semiconducting tubes.

We note that we do not see any 2F component of the CIA signal, nor have we observed any asymmetry in our devices with respect to unipolar vs. bipolar configurations. Our attempts to produce unipolar, hole-only devices were unsuccessful. The CIA spectra for bipolar devices are almost identical to the spectra for unipolar devices except that the overall effect is smaller (around 60%) because rapid electron-hole recombination reduces the number of carriers contributing to the effect.

3.4 Electroabsorption

When a neutral charge configuration is placed in an electric field the dipole moment and polarizability of the configuration may change. As a result, the absorption features due to those excitons will change with the applied field. Electroabsorption (EA) has been widely used in π-conjugated polymers to study the nature of photoexcitations there.[62–64] In order to see the influence of the electric field on relatively isolated tubes we obtained the electroabsorption spectrum in the NIR-Vis region for a film of SWNTs dispersed with SDS and embedded in a matrix of poly-vinyl alcohol (PVA).

The absorption and EA are shown in Figure 3.17. From Figure 3.17a we can see that the tubes are of a wider diameter distribution than those used in the electrochemical measurements, but the tubes are more disperse so we can see more of the individual exciton peaks. Figure 3.17b shows the results of the EA measurement; note that $\Delta T/T \approx -\Delta OD$ (see Chapter 2), so peaks in the ΔT/T spectrum correspond to bleaching. There is no electroabsorption signal below 0.6 eV, indicating that the free carriers absorption is not affected by a quasi-static field (we measured down to 0.2 eV using the FTIR) and there are no below-gap transitions that become allowed through mixing with the quasi-static field.

In the spectral region corresponding to excitonic absorption there is a rich EA signal which we interpret in light of its connection to the derivative of the absorption because of the connection between nanotubes and other π electron systems such as π-conjugated polymers. As mentioned in Chapter 2, the electroabsorption signal in the absence of any transfer of oscillator strength is predicted to behave

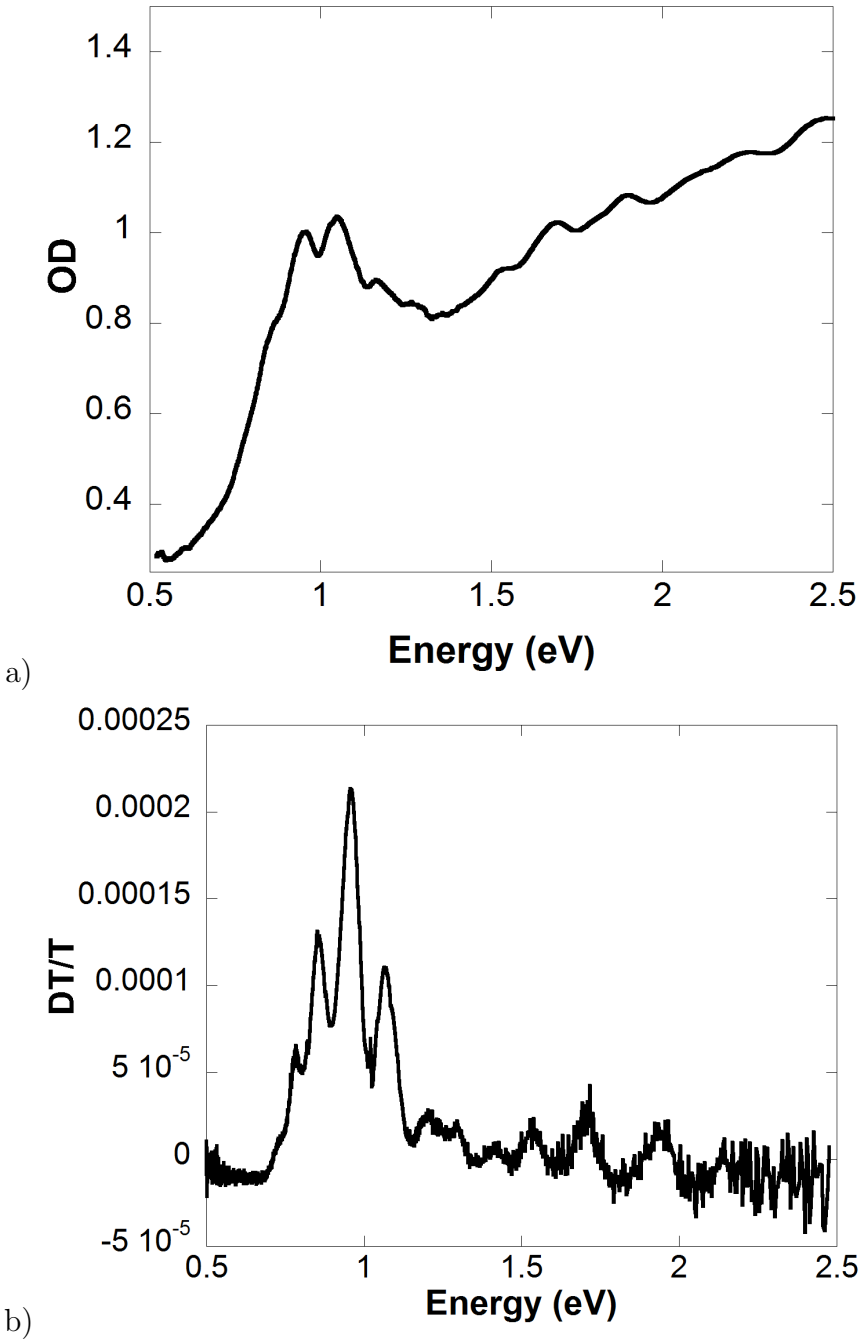

Figure 3.17. Absorption (a) and electroabsorption (b) of a SWNT film dispersed in SDS.

according to

$$\Delta\alpha \approx \frac{1}{2}\Delta p F^2 \frac{\delta\alpha}{\delta E} + \frac{1}{6}\mu F^2 \frac{\delta^2\alpha}{\delta E^2} \tag{3.7}$$

where F is the applied field, p is the polarizability of the excitation and μ is its permanent dipole moment.[65] However, if there is a transfer of oscillator strength then the actual signal is better represented by

$$\Delta\alpha = \delta f \alpha + \frac{1}{2}\Delta p F^2 \frac{\delta\alpha}{\delta E} + \frac{1}{6}\mu F^2 \frac{\delta^2\alpha}{\delta E^2} + \Delta\alpha_{other} \tag{3.8}$$

where δf is a parameter representing the amount of oscillator strength being transferred to α_{other}.

In Figure 3.18 we show the raw signal compared to the negative of the first derivative of the background-corrected absorption with respect to photon energy. The positions of the peaks in each spectrum are a close match, but the overall shape of the EA spectrum does not match the derivative spectrum. There are two reasons for the discrepancy. First, the sample comprises many different chiralities, each of which has a different susceptibility and therefore a different change in polarizability upon the application of the quasi-static field. Thus, the constant of proportionality between the EA spectrum and the derivative spectrum will depend on the particular tube. Second, there is a broad offset of the EA spectrum that seems to correspond with the background-corrected absorption.

To quantify our analysis via Equation 3.8 we divided the absorption derivative spectrum into sections corresponding to the individual peaks. We then used Mathematica to do a least-squares linear fit of the derivative to the EA data. We interpolated the EA data to perform the fit at corresponding photon energies. The results are shown in Figure 3.19, which indicates that the observed electroabsorption may be best explained by

$$\Delta\alpha = -\delta f \alpha + \frac{1}{2}\Delta p F^2 \frac{\delta\alpha}{\delta E} \tag{3.9}$$

where Δp is proportional to the scale factor (Figure 3.19c) and δf is proportional to the offset (Figure 3.19d).

Figure 3.19a shows the close match between the electroabsorption and the piecewise fit of the first derivative corresponding to Equation 3.9 where the normalized energy spectrum of Δp is shown in Figure 3.19c. The similarity between

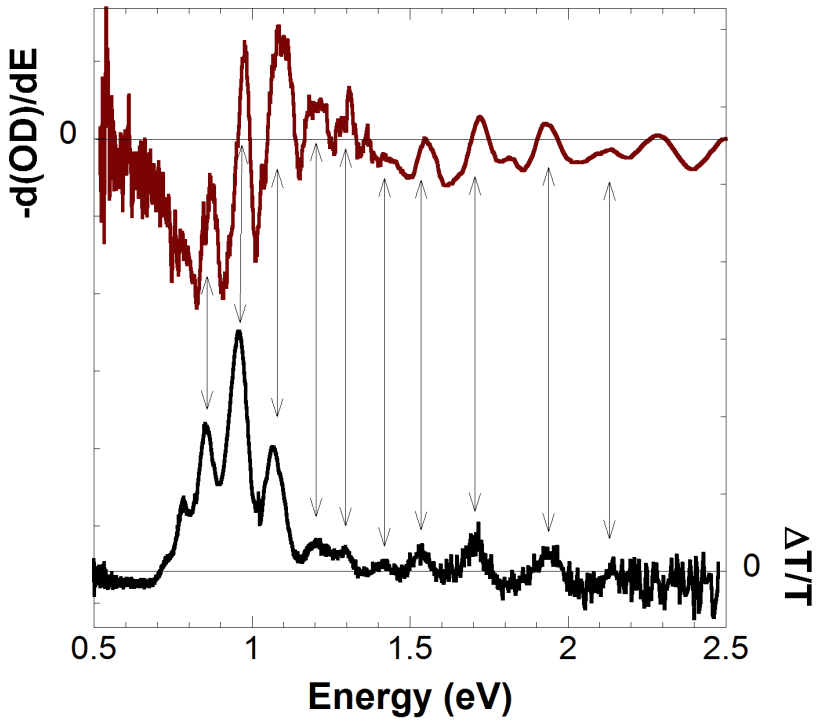

Figure 3.18. Electroabsorption of SWNT film dispersed in SDS at 1kHz modulation and $20MV/cm$ field shown along with the negative of the first derivative of the absorption. The vertical lines identify corresponding peaks in the two spectra.

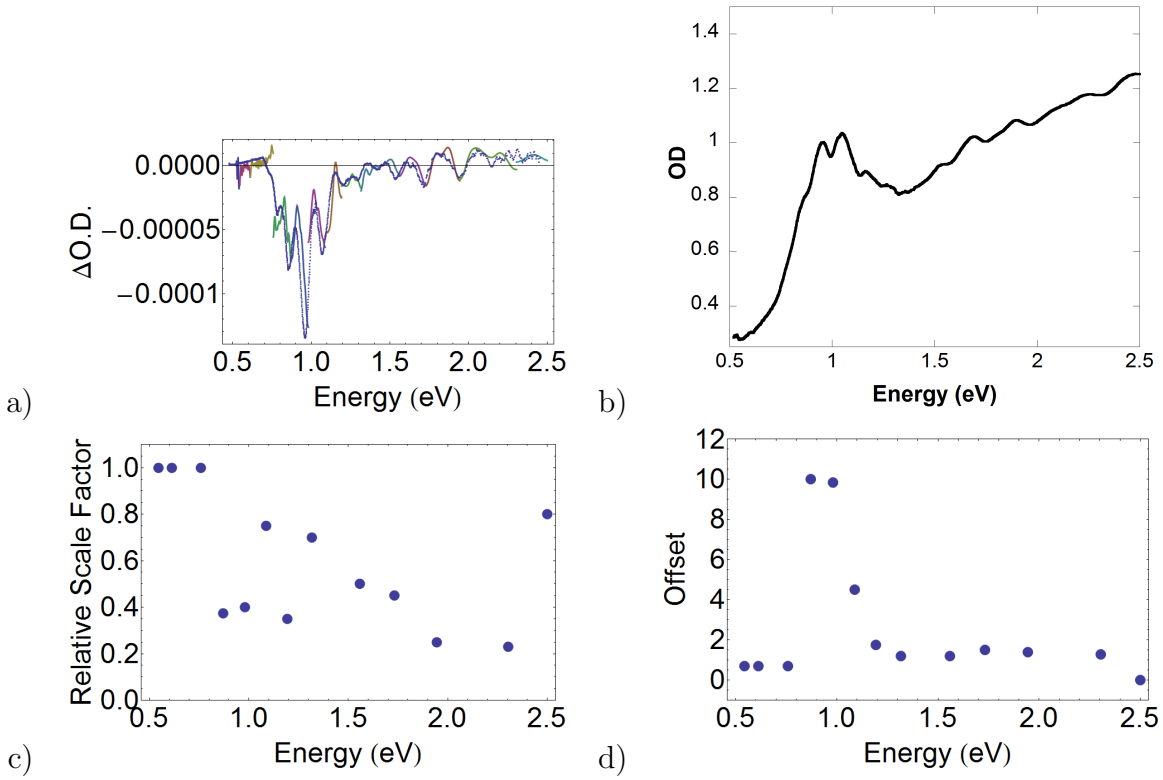

Figure 3.19. Analysis of the electroabsorption of a SWNT film dispersed in PVA. a) Electroabsorption signal (points) shown with the piecewise adjusted first derivative (solid line segments). b) Absorption spectrum of the sample. c) Normalized spectrum of multiplicative factors for the first derivative. d) Normalized spectrum of the linear offset.

Figure 3.19b and the background-corrected features in Figure 3.19d reflects the first term in Equation 3.9. The scale factor in Figure 3.19c is 10^5 eV, from which we estimate the exciton polarizability to be 3×10^{-38} Cm^2/V. This corresponds to an exciton volume, in the traditional three-dimensional approximation, of around $300\mathring{A}^3$; this is comparable to the size determined from recent measurements of the exciton via high-intensity exciton bleaching where the radius of the exciton was reported to be 2.0 nm for (6,5) tubes.[66] It is difficult, however, to compute the polarization volume in carbon nanotubes because of their unique geometry. Furthermore, this result is biased by the assumption that the nanotubes experience the full applied field. In fact, because the nanotubes are conductive most of the potential drop occurs in the surrounding PVA matrix. Correcting for this effect would reduce the effective field and increase our estimation of the polarizability of the excitons.

We note that some recent experiments on well-separated tubes have indicated a second-derivative like signal that has been interpreted as being due to a transfer of oscillator strength to so-called "dark" (forbidden) excitons below the optically active excitons.[67] However, because a small contribution from the zeroth-derivative can resemble a second-derivative signal these results agree with ours within experimental uncertainty. We observed a variation in the contribution from δf in Equation 3.9 with respect to the concentration of surfactant and degree of separation that can easily explain that data. Furthermore, the observed electrobleaching may be better understood in terms of the charge-induced bleaching due to the inadvertently injected charges (see Discussion below).

3.4.1 Voltage and Polarization Dependence

The variation in the EA signal with the applied field depends on the nature of the effect. We studied the EA signal for our SWNT film with a variety of field strengths. Figure 3.20a shows the magnitude of the EA signal at a variety of applied fields. The EA signal increases linearly with the square of the applied field. This dependence of the EA signal is uniform for all regions of the spectrum, which indicates that δf also scales as the square of the applied field.

We also measured the dependence of the EA signal on the polarization of the

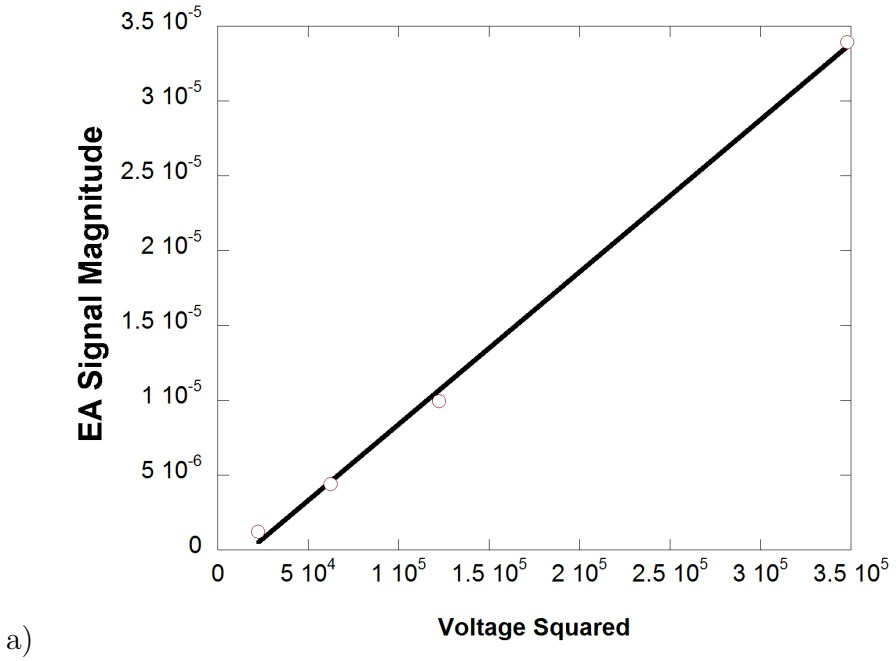

a)

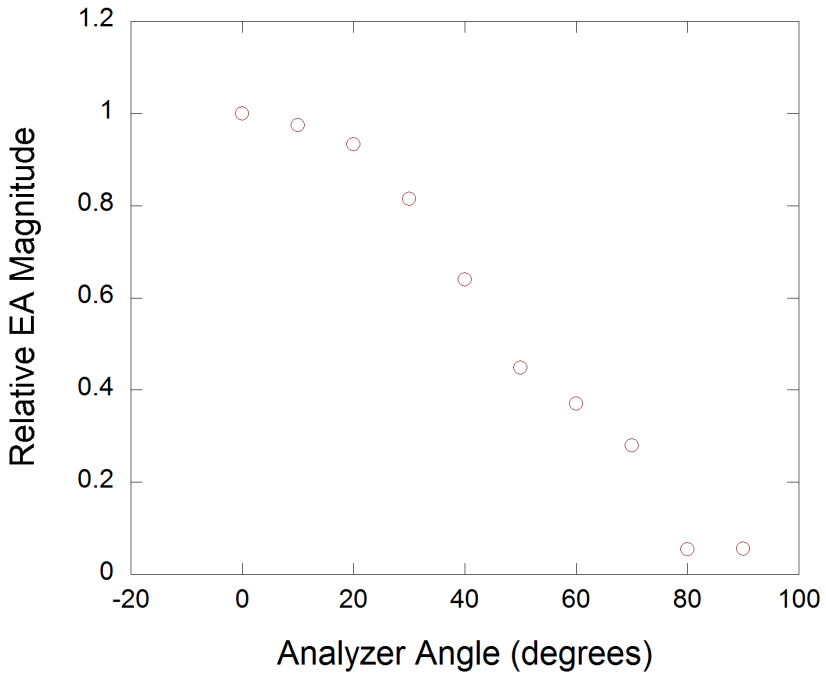

b)

Figure 3.20. The voltage and polarization dependence of the EA signal. a) Magnitude of the EA signal as a function of the square of the applied voltage. b) Normalized EA signal strength as a function of polarization angle between the analyzer and the direction of the applied field.

light with respect to the direction of the applied electric field. Figure 3.20b shows the relative magnitude of the EA signal at several polarizations of the incident light with respect to the direction of the applied field (which is perpendicular to the electrode "fingers" discussed in Chapter 2) normalized to the parallel configuration. The absorption of SWNTs is strongly polarized along the nanotube axis because of the quasi-one-dimensional character of the tubes. The nanotubes in our films, however, are oriented randomly. Therefore, by polarizing the incident light we are selecting the absorption from those tubes that lie along the direction of polarization. The polarization dependence of the EA signal shows that only those tubes that are oriented with their axes in the direction of the applied field are affected by the field.

3.4.2 Discussion

The linear dependence of the EA amplitude on the square of the field, the polarization of the effect along the nanotube axis, and the similarity between the EA spectrum and the first derivative of the absorption are all indications that the primary effect of the applied field is to change the polarizability of the neutral excitons responsible for the absorption.

We do not see any Franz-Keldysh oscillations, as we would expect if interband transitions were to contribute to the absorption spectrum, but we do see a negative offset in the EA that corresponds to a contribution proportional to the absorption, indicating electro-bleaching of the excitonic transitions. Conspicuously absent from the EA is any signal that might be attributed to a transfer of oscillator strength (the last term in Equation 3.9. It is possible that the oscillator strength is transferred to interband transitions due to the field-induced weakening of the exciton binding energy. The resulting Franz-Keldysh oscillations may be "hidden" inside the combined signal from the many different chiralities that exist in the sample. However, Franz-Keldysh oscillations have a period that depends on the strength of the applied field and we see no change in the spectrum with the field. We can say with little uncertainty that no field-induced transitions appear below the lowest-lying, optically-active exciton.

On the other hand, the beaching may be due to the charge-induced bleaching

observed in the CIA spectrum. The films used for electroabsorption have very high resistances, but not infinite resistance. Even though the apparatus is not designed to inject current it is possible that the small current that is injected during the EA measurement is responsible for the δf component of our signal. This could also explain why we observe a variation in this component among different films. The degree to which the tubes bundle together and percolate the insulating matrix to provide conductive pathways through the film changes the amount of charge inadvertently injected in the EA measurements.

3.5 Photo-induced Absorption

As mentioned in Chapter 2, the absorption of light by excitons can lead to a number of effects in traditional semiconductors and in π-conjugated polymers. In organic materials especially the resulting excitons can dissociate into a variety of charge complexes. One way to probe the nature of these excitations is to measure the photo-induced absorption (PA). We measured the photo-induced absorption of a well-dispersed film of SWNTs and the result is shown in Figure 3.21a. There is no PA signal at lower energies, and the PA signal at higher energies is very small compared to the noise in our apparatus. Like the electroabsorption, the PA spectrum closely resembles a linear combination of the zeroth and first derivatives of the absorption spectrum (Figure 3.21b). We pumped with a $514.5nm$ and $488nm$ excitation with similar results, and a similar result has been reported for 1.17 eV excitation.[68] Both of these pump wavelengths correspond to high energy semiconducting excitons in our samples (SC_{3-3}). We used a modulation frequency between $300Hz$ and $1kHz$.

3.5.1 Discussion

In π-conjugated systems the PA spectra help to identify the nature of the photo-excitations as well as subsequently formed charge complexes. The species that form from these excitons, including polarons, polaron pairs, bipolarons, etc., each have their own spectroscopic signature in the PA signal. We see no such peaks in the PA of SWNT films. On the contrary, we see a signal that is very similar to the electroabsorption signal in that it follows the first derivative of the

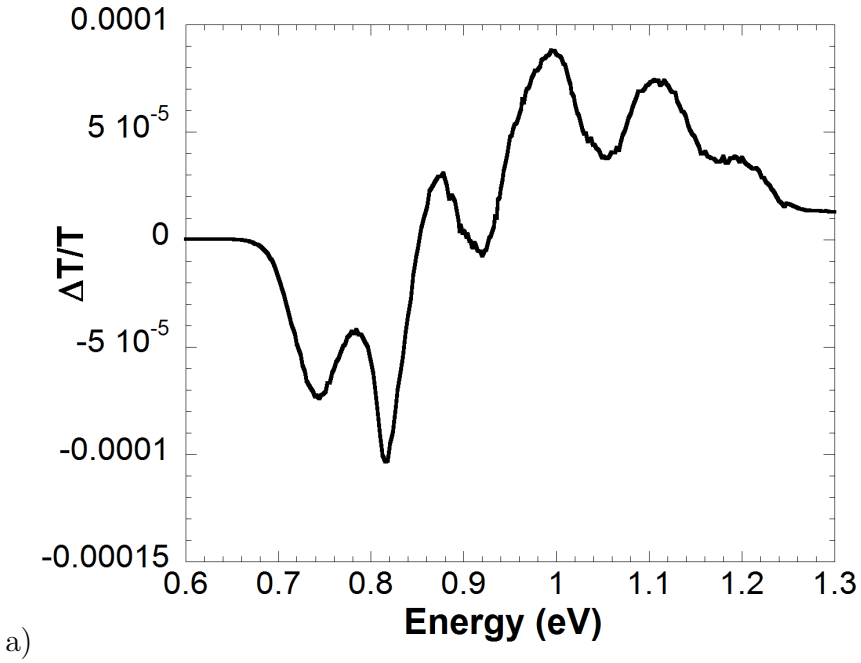

a)

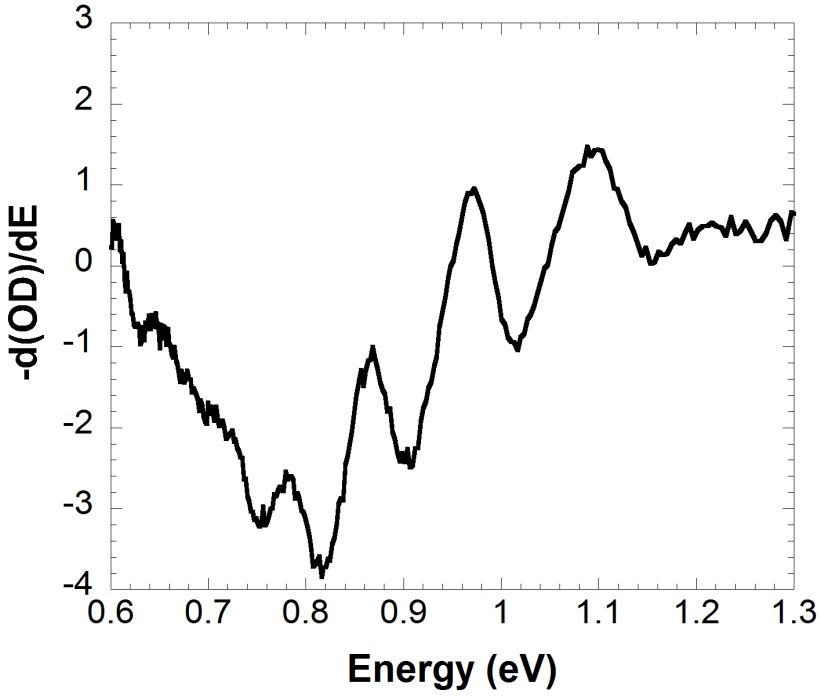

b)

Figure 3.21. The photoinduced absorption for a film of SWNTs in the NIR-Vis spectral range. (a) $\Delta T/T$ under illumination. (b) The negative derivative of the film's absorption spectrum.

absorption with an offset proportional to the absorption itself. We have reported the dependence of the PA signal on pump laser power and modulation frequency to be consistent with the idea that the PA signal is due to the local electric fields produced by *trapped* photoinduced charges within our nanotube film.[68] This is why the PA spectrum is so similar to the EA spectrum. The magnitude of the effective local field from such trapped states would depend on the nature of the trap and not on the laser pump power, so long as only one such charge complex is allowed per trap.

A diagram of how this might happen is shown in Figure 3.22 and is similar in some respects to the charge-transfer complexes in some organic photovoltaic materials.[69] The absorption of light produces bound electron-hole pairs, but those excitons are free to migrate. When they arrive at trap sites (inhomogeneities in individual tubes' environments, for example) they may persist for milliseconds, during which time their electric field influences the absorption in their immediate vicinity. It should be noted that a derivative-like spectrum could result from laser-induced heating of the sample. We used a large heat capacity substrate (sapphire) to minimize heating effects, and we note that the spectrum does not qualitatively change over a large variation in pump power.

The fact that this derivative-like signal is only present at low energies suggests that the photo-excitations migrate to lower energy manifolds, i.e., the large diameter tubes. The mobility of these photo-excitations in metallic tubes is exceptionally high and our data suggest that metallic tubes efficiently rid themselves of the associated internal fields, possibly by transferring the charge complexes to the large diameter semiconducting tubes.

3.6 Summary

The absorption of SWNTs in the far infrared is dominated by Drude-like free carriers absorption from the collection of metallic and semiconducting tubes. Electrochemical doping and direct charge injection can modify the density of those free carriers and thereby change both the plasma frequency and scattering rate. Fits of the Drude model to the experimental data allow us to calculate the density of added charges. For tubes doped electrochemically at 1 V in 1 Molar NaCl the

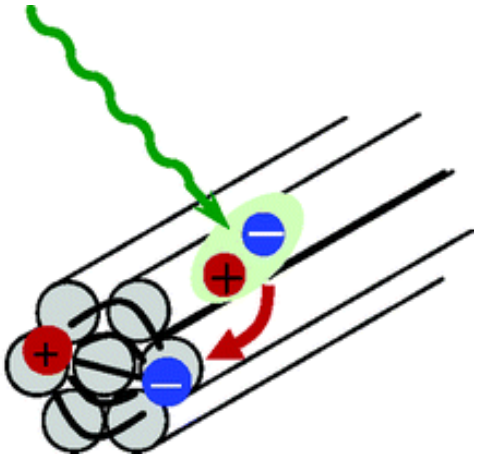

Figure 3.22. Depiction of local electric fields due to trapped photo-excitations.

doping of the semiconducting tubes determined by these fits is on the order of the carrier density in the metallic tubes: $10^{15} - 10^{16}/cm^3$. In the near infrared and visible portions of the spectrum the absorption is due to excitons and the collective π-plasmon. The plasmon is unaffected by direct charge injection, but ionic dopants on the tubes' surfaces modify the Van der Waals interaction among tubes and thereby change the plasmon absorption energy and strength. The excitons themselves, on the other hand, are strongly affected by the free-carrier density, local dielectric constant, and local electric fields. The electroabsorption and photoinduced absorption of SWNTs shows that the absorption peaks are in fact due solely to neutral excitons and not to interband transitions, but also indicate a decrease in absorption with applied field that may be compensated by a transfer of oscillator strength to some other as yet unobserved transition. These excitons are screened by the addition of free carriers to the nanotubes, and the carriers also contribute to the phenomenon of k-space filling whereby the generation of excitons is quenched and the absorption is bleached. The lack of significant change of the exciton transition energies with the corresponding decrease in binding energy is due to the compensating band gap renormalization.

CHAPTER 4

RAMAN SCATTERING IN SWNTS

4.1 Vibrational Modes of Carbon Nanotubes

4.1.1 Introduction

There are hundreds of phonon modes in SWNTs, but only a handful are Raman active.[1,8,70] In ab initio calculations of the phonon dispersions for SWNTs a common approach is to start with the phonon dispersion for graphite and use the zone-folding method to impose periodic boundary conditions along the tube circumference (similar to the tight-binding approach for the band structure discussed in Chapter 3). Approaches based on single-molecule vibrations have also been used with varying degrees of success. However, most nanotubes are at least two orders of magnitude larger in length than in diameter, so a quasi-one-dimensional approach yields results that are in closer agreement with experiments.

The differences in point group symmetries between armchair (ac), zigzag (zz), and chiral (ch) nanotubes allow for different symmetries of the Raman active phonons in those tubes. However, the frequencies of those modes lie in similar regions of the spectrum, even for tubes of different chiralities. For example, the tangential modes in the G band (discussed below) for ac-SWNTs consist of symmetric vibrations along the circumference of the tube, while for zz-SWNTs the comparable mode is along the axis of the tube.[1,8,70] The comparable modes in chiral SWNTs twist along the surface of the tube in a direction that has both axial and circumferential components.

4.1.2 Raman Spectra of SWNTs

In general, the Raman spectra of SWNTs can be divided into three primary regions of interest, with two other regions of note. The three primary regions are as follows: i) a low energy region consisting of radial modes, most notably the radial breathing mode (RBM); ii) a high energy mode that is connected with

disorder in the tubes (D); iii) a high energy region consisting of vibrations along the nanotube surface, both circumferential and axial, that is directly connected to the primary Raman active mode in graphite (G). Additionally, the overtones of the D and G modes have large scattering cross sections and are observable in most Raman spectra. A sample Raman spectrum is given in Figure 4.1. The main features are marked, and they will each be discussed below. Figure 4.2 illustrates the three main types of vibrational modes that contribute to the Raman spectrum.

4.1.2.1 Radial Breathing Mode

The vibrational modes that consist of the motion of carbon atoms perpendicular to the nanotube axis are called radial modes and have a relatively low energy (near $200cm^{-1}$). Of these, the RBM is the strongest scatterer and plays a key role in nanotube characterization.

The RBM of SWNTs consists of a symmetric motion of all of the carbon atoms toward and away from the nanotube axis (see Figure 4.2). Thus, the frequency of the RBM is strongly dependent on the nanotube diameter and chirality. Whether considering nanotubes as two-dimensional surfaces like cylindrical shells[71] or as three-dimensional bulk cylinders,[1,72] the general relationship between nanotube diameter and the frequency of the RBM is qualitatively the same: the RBM frequency is inversely proportional to the nanotube diameter. While the specific relationship has been shown to depend on the nanotube type (armchair, zigzag, or chiral), the effective dependence on diameter in a heterogeneous sample is given by

$$\omega_{RBM} = \frac{A}{d} + B \tag{4.1}$$

where A and B are constants and d is the nanotube diameter.[1] For individual tubes the values of A and B depend on the chirality, but on average it has been shown that $A = 227cm^{-1}nm$ and $B = 10cm^{-1}$ are adequate to describe samples of interacting tubes such as those in commonly occuring bundles.[1,73,74]

4.1.2.2 Disorder Mode

The D mode in SWNTs is near $1350cm^{-1}$ and is associated with defects in the nanotubes. A comparable band with similar energy appears in graphene. The

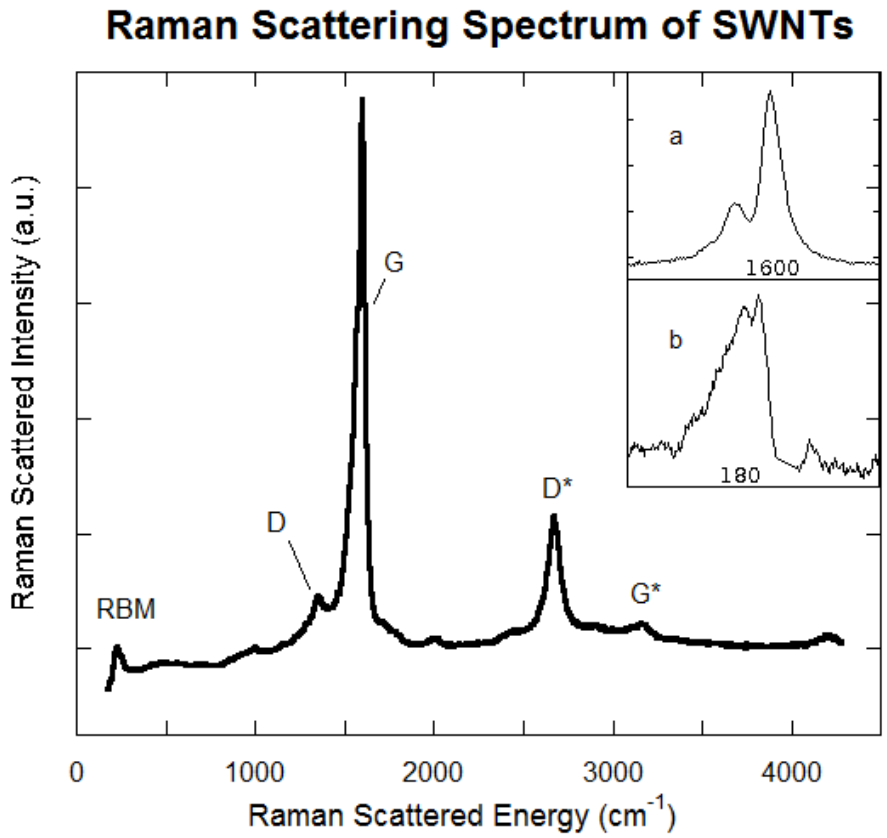

Figure 4.1. Raman spectrum of a heterogeneous sheet of SWNTs for an excitation wavelength of $488nm$. The most important regions of the spectrum are labeled, and each is discussed in detail in the text. a) High resolution plot of the G band showing the G^+ and G^- modes. b) High resolution plot of the RBM band consisting of several peaks (some unresolved) of various intensities.

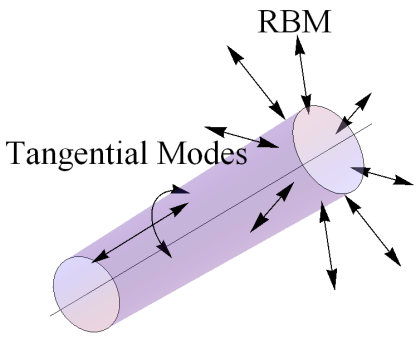

Figure 4.2. A cylinder representing a SWNT with an illustration of the three primary optical phonon types. The RBM consists of the radial motion of the carbon atoms in the tube while the tangential modes G and D consist of motion along the surface of the tube.

dependence of the frequency of the D band on excitation energy and the observed differences between the Stokes and anti-Stokes frequencies for the D mode indicate that it is a doubly-resonant process that is assisted by scattering of phonons and/or electrons off of defects in the lattice.[1,70] The overtone of the D mode is referred to sometimes as D* and sometimes as G'. The use of the letters D and G in labeling the Raman modes is unconnected to the symmetry of the vibrations. Rather, it arises from the origin of the modes. G modes are those which can be connected to similar modes in graphite and graphene, while D modes are associated with disorder. The confusion sometimes arises because the D modes are also found in some graphene samples. We will refer to it as D* to indicate its connection to the disorder mode near $1350 cm^{-1}$. The amplitude of Raman scattering from the D* mode is often much larger than from the corresponding single phonon process (see Figure 4.1), which can be partially explained by the double resonance discussed below.[1,70]

It has been proposed that the relative intensity of the D and D* modes to the G modes can be used as a measure of the number of defects in a sample.

Defects include, however, effects from the ends of the tubes. So, samples consisting of unusually short nanotubes ($< 100nm$ in length) also have strong D modes. Additionally, the resonance enhancement discussed below can significantly change the intensity of the D* peak (see Figure 4.3). Therefore, we do not assign any quantitative measure of the disorder to the scattering intensity of this peak.

4.1.2.3 Graphite Modes

The strongest band of Raman active modes in SWNTs is found near $1590cm^{-1}$ and originates from the dominant in-plane mode in two-dimensional graphene (see Figure 4.2). However, in SWNTs the curvature splits this band into a high energy mode G^+ and a low energy mode G^- (see the inset of Figure 4.1). In fact, there are several distinct modes in this spectral region, but most are of low scattering amplitude. The exception is in metallic nanotubes, where several tangential modes are enhanced, shifted, and broadened by the Kohn anomaly.[74–76] Figure 4.4 shows the Raman spectrum of two types of nanotubes in this region. The second order G band is also observable and is usually labeled as G^*.

The symmetries associated with the vibrations that contribute to the G band are different for different types of tubes. The frequency of the G^- mode, which is due to vibrations along the tube circumference, is redshifted from the G^+ mode because the curvature of the tube surface elongates the bonds and reduces the effective spring constant between neighboring carbon atoms. The G^+ mode is primarily along the nanotube axis and has a frequency much closer to the corresponding mode in graphite. The specific frequencies of these two modes depend generally on the chiral angle of the nanotube but not its diameter. There is a weak dependence on diameter for small tubes, but among tubes of similar diameters the chiral angle affects the mode frequencies much more strongly.

There are, of course, many other unlabeled features in Figure 4.1. Many of these are combination modes or are due to impurities in the sample. Their physical origins are more complex, so the information they contain is much less than that contained in the main spectral regions discussed here.

4.2 Resonance Raman Enhancement in SWNTs

The Raman scattering cross-section of a material is strongly enhanced when the energy of the incoming or outgoing photon corresponds to an allowed electronic transition. Because this enhancement can be several orders of magnitude one can selectively probe a subset of tube types in a heterogeneous collection of nanotubes by choosing a particular energy for the excitation laser.

Figure 4.3 shows Raman spectra for two excitation energies on the same sample. In each spectrum the scattering is due to the subset of tubes in the sample that are resonantly excited by the corresponding excitation laser energy. Despite having been obtained from the same sample there are several noticeable differences between the two spectra.

In the RBM region the upper spectrum contains only one obvious peak, while the lower spectrum resolves at least two peaks. The dominant RBM frequency in the lower spectrum is blue shifted by almost 10% from the RBM peak in the upper spectrum. Since the RBM frequency depends strongly on diameter this shift is an indication that the $488nm$ excitation selectively probes a different diameter tube in Raman scattering than the $532nm$ excitation.[1,8,70]

In the G band the spectrum from the $532nm$ excitation clearly resolves the G^+ from the G^- mode, while for $488nm$ excitation those two modes are much closer in energy. This is because the separation in energy between the G^+ and G^- modes depends on the diameter and chirality of the tube. In general, the G^+ mode varies little in frequency except for tubes whose chiral angle is close to 30° (a very small fraction of the tubes in a given sample). The G^- mode on the other hand primarily involves vibrations around the circumference of the tube and thus depends more strongly on the tube curvature.

While the first order D mode is very similar between the two spectra, the D^* mode is red shifted and significantly enhanced for $532nm$ excitation as compared to $488nm$ excitation. The strong dependence of scattering intensity on excitation energy is taken as evidence that the D^* mode is a double-resonance feature, meaning that both the incoming and outgoing photons correspond to real electronic transitions in the tube.[1,8] Because of this, the resonance enhancement for certain excitation wavelengths is even stronger because those wavelengths correspond more

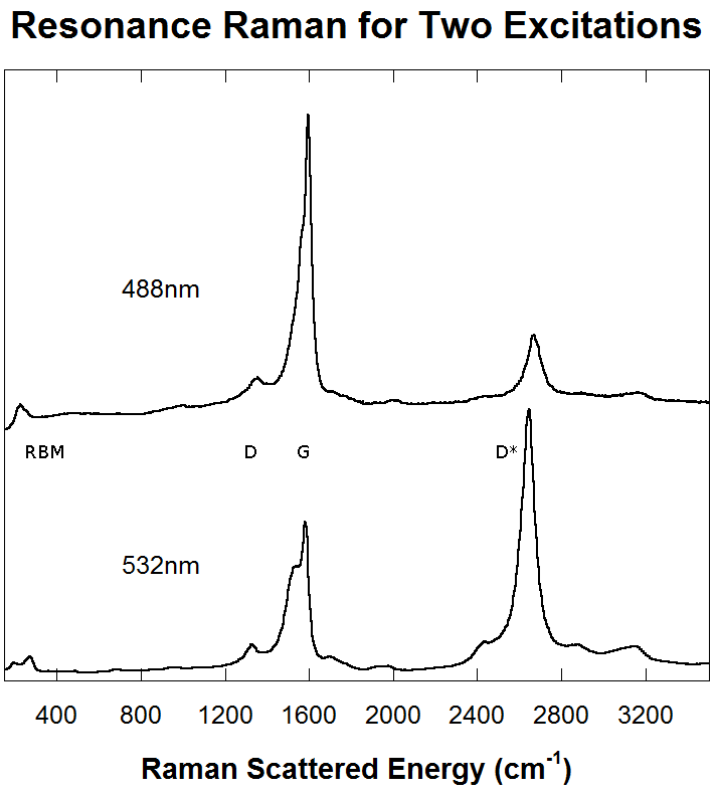

Figure 4.3. Raman spectra for a heterogenous sheet of SWNTs at 532nm (upper) and 488nm (lower) excitation.

closely to the right crossings in the phonon dispersion curves in SWNTs.

4.2.1 Chirality Dependence of Resonance Enhanced Raman Scattering

As discussed above, one can determine the diameter of a resonantly excited set of tubes by the frequency of the RBM mode. By cross-referencing the diameter with the excitation energy on a Kataura plot (discussed in Chapter 1) one can determine the type of tube that is responsible for the given Raman spectrum. The Kataura plot is reproduced in Figure 4.5 for reference. Note that for the spectra in Figure 4.4 the spectra arising from metallic tubes have a qualitatively different appearance than those arising from semiconducting tubes. For example, the spectrum obtained from $1.92eV$ excitation corresponds to tubes with a diameter of approximately $1.15nm$, indicating that the excitation laser is in resonance with E_{11} for metallic tubes in the sample. On the other hand, the spectrum obtained with $2.41eV$ excitation is from tubes of a similar diameter, but the laser is in resonance with E_{33} of semiconducting tubes (not shown in Figure 4.5).

It is important to note that the use of the Kataura plot is subject to uncertainties in the RBM frequencies as well as changes in the electronic structure of the tubes. It has been suggested that environmental effects may shift the vertical axis on the Kataura plot by as much as $0.2eV$. Therefore, one should always use a variety of methods to verify the diameter and resonance conditions for the SWNTs in a given sample. One easy way to distinguish m-SWNTs from s-SWNTs is by the shape of their G band Raman spectrum as shown above.

Similarly, one should take care in assigning the diameter of SWNTs from the RBM mode. The RBM modes in a heterogeneous sample of SWNTs can show several distinct peaks. This is because more than one type of nanotube may be in resonance to some degree with a particular excitation energy. The number and relative intensity of various peaks in the RBM band depend on the distribution of diameters and chiralities in the sample (see Figure 4.3). In general we choose the dominant peak when assigning the diameter of the tubes that are in resonance with our excitation laser. The error introduced is small compared to the uncertainty in the experimentally determined diameter-frequency relationship discussed above.

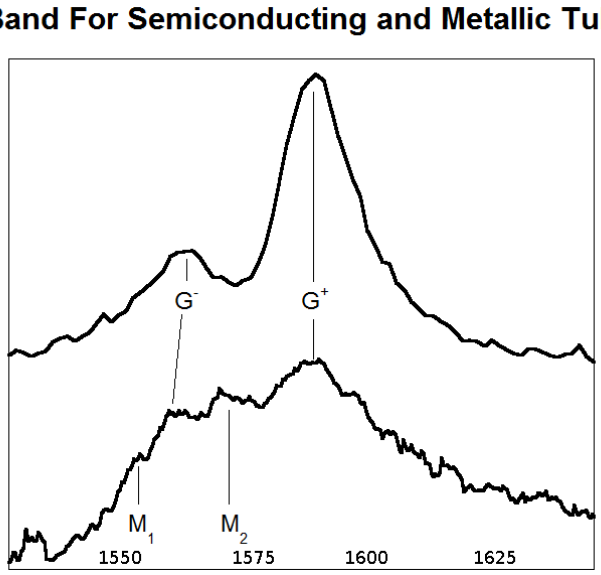

Figure 4.4. Lineshapes for the G band near $1590cm^{-1}$ of s-SWNTs (top) and m-SWNTs (bottom). Both have similar G^+ and G^- modes, but there are additional modes (M_1 and M_2) in the G band that are selectively enhanced in metallic tubes.

The diameter obtained in this way should be in agreement with the known diameter distributions produced by various manufacturing methods.

4.2.2 Impurities and Defects in the Raman Spectra

We note here the influence of standard defects and impurities (as discussed in Chapter 2) on the Raman spectra of our samples. The excitation laser spot size ranges from $0.7\mu m$ to $1cm$ in diameter depending on the laser and the Raman system used. Within that excitation area it is always possible that we illuminate something that is not a nanotube. Defects in the nanotube walls, especially near the ends, result in Raman scattering signals that are broadened and shifted with respect to their intrinsic state. Metallic and other impurities increase scattering and sometimes result in an enhanced fluorescence background. In reporting the data in this chapter we have rejected anomalous results that we interpreted as being due to one of these two effects.

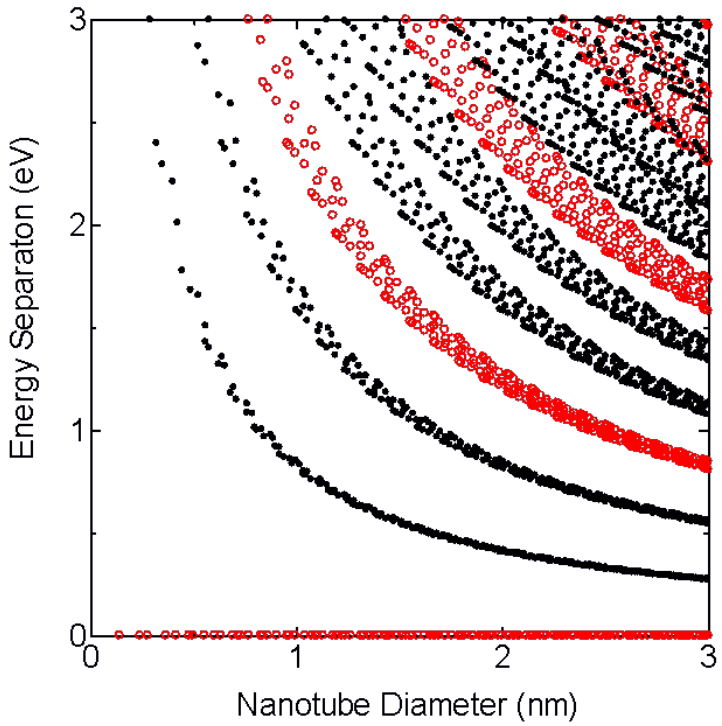

Figure 4.5. The Kataura plot contains one point per transition per distinct nanotube chirality. The horizontal axis is the tube's diameter, and the vertical axis is the transition energy of one of the tube's allowed electronic transitions (after,[4] taken from wikipedia.org). There are many more allowed transitions than are represented by the branches on this plot.

4.3 Electrochemical Doping

As discussed in Chapter 3 there is enormous interest in the effects of electrochemical doping on SWNTs because of the many potential applications for nanotubes in electronic devices. Electrochemical doping is the process of injecting charges in the nanotubes by the application of a charge double-layer at the interface of a solution (see Chapter 2 for details). There are many advantages to doping the nanotubes in this way, most notably being that the charge double-layer avoids the fatigue problems associated with the intercalation of charges inside the tubes and between tubes in bundles.

In general, the effect of electrochemical doping on the Raman spectra of SWNTs is twofold. First, the amplitude of the scattered light changes in a way that parallels the changes in absorption shown in Chapter 3. Second, the frequencies of the Raman peaks are shifted. We will discuss both of these effects in detail for both semiconducting and metallic tubes and then describe a mechanism for both phenomena in heterogeneous samples of SWNTs. The results discussed in this section were primarily obtained *in-situ* as described in Chapter 2. The *ex-situ* behavior is also discussed below.

4.3.1 EC Doping of s-SWNTs

4.3.1.1 G Band

Figures 4.6 and 4.7 show the G band for a heterogenous sample of nanotubes at various electrochemical potentials excited by $514.5nm$ laser light. For hole doping (Figure 4.6) the amplitude of the Raman scattering decreases and the frequencies of each of the primary modes is slightly blue shifted. For electron doping (Figure 4.7) the scattering amplitude increases at low voltages but decreases at higher voltages. At all negative values of the doping potential the Raman frequencies are red-shifted. We repeated this experiment over a wide range of doping potentials and for a variety of excitation wavelengths. In each case, the general behavior of the Raman signal from semiconducting nanotubes shows the same general behavior.

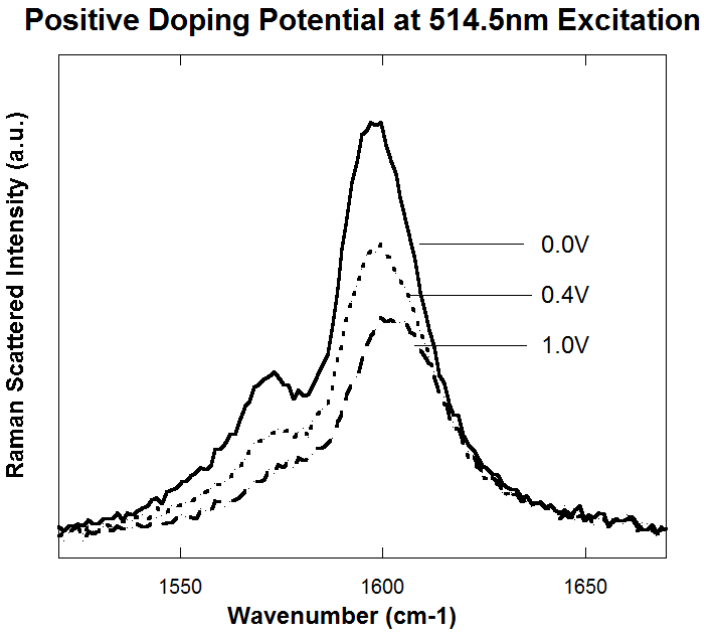

Figure 4.6. The Raman scattering spectrum for the G band of semiconducting nanotubes at 3 doping levels: 0V, +.4V and +1V vs Ag/AgCl. The peak intensity decreases and the Raman frequency increases with increasing doping voltage.

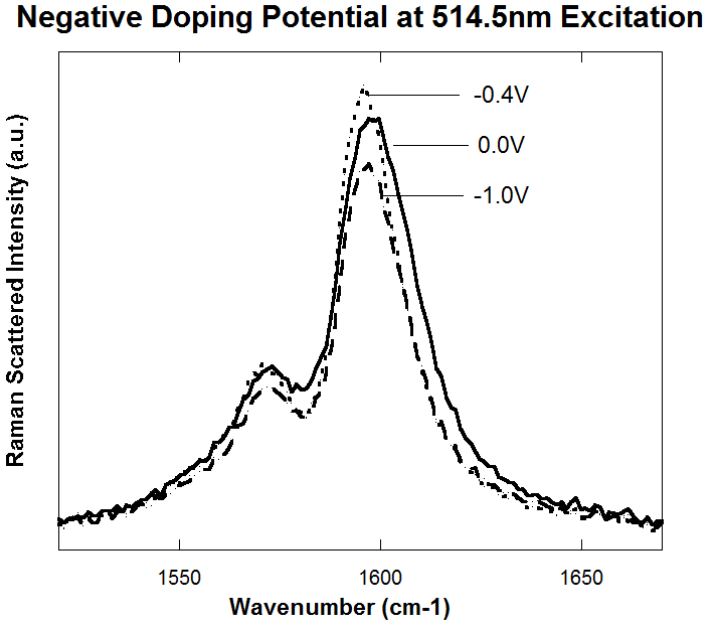

Figure 4.7. The Raman scattering spectrum for the G band of semiconducting nanotubes at 3 doping levels: 0V, -.4V and -1V vs Ag/AgCl. The peak intensity increases, then decreases with increasing doping voltage. The Raman frequencies redshift with increasing voltage.

4.3.1.2 RBM

The RBM of s-SWNTs changes in a similar way upon electrochemical doping as the tangential modes for the same tubes. Figures 4.8 and 4.9 show the RBM spectra of a nanotube sheet excited at $514.5nm$ under various doping conditions. The dominant peaks at $290cm^{-1}$ and $355cm^{-1}$ indicate that the $2.41eV$ excitation energy is resonantly enhancing the Raman signal from tubes with diameters of approximately $0.7 - 0.9nm$. From the Kataura plot we can see that this could corresponds to the E_{11} transition in metallic tubes or to the E_{22} transition in semiconducting tubes in our sample. The semiconducting nature of the tubes is verified by the absence of the anomalous metallic modes in the G band (see Figures 4.6 and 4.7.

4.3.2 EC Doping of m-SWNTs

4.3.2.1 G Band

Figures 4.10 and 4.11 show the effects of electrochemical doping on the G band modes of metallic tubes. As mentioned earlier, m-SWNTs exhibit an anomalous enhancement and broadening of several modes in the G band due to the Kohn anomaly. The appearance of these modes in the Raman spectrum, along with the cross-reference to the Kataura plot, indicates that the excitation laser is in resonance with metallic tubes for these spectra.

The effects of electrochemical doping on these additional metallic modes is remarkable. Both positive and negative doping potentials produce a decrease in these additional metallic modes that is greater than the corresponding decrease in the G^+ and G^- modes. At sufficient doping levels the G band spectra for m-SWNTs qualitatively approaches that of the s-SWNTs. Recent studies of the Raman spectra of *individual* m-SWNTs suggest that the changes in Raman Frequency are due to the influence of the Fermi surface on the electron-phonon coupling in metallic tubes.[75,76] However, in those studies the shifts in frequency were qualitatively different than in our heterogeneous samples. A possible explanation for this discrepancy is suggested by the studies of nanotube actuation discussed below.

Despite the difference between the behavior of the anomalously enhanced modes

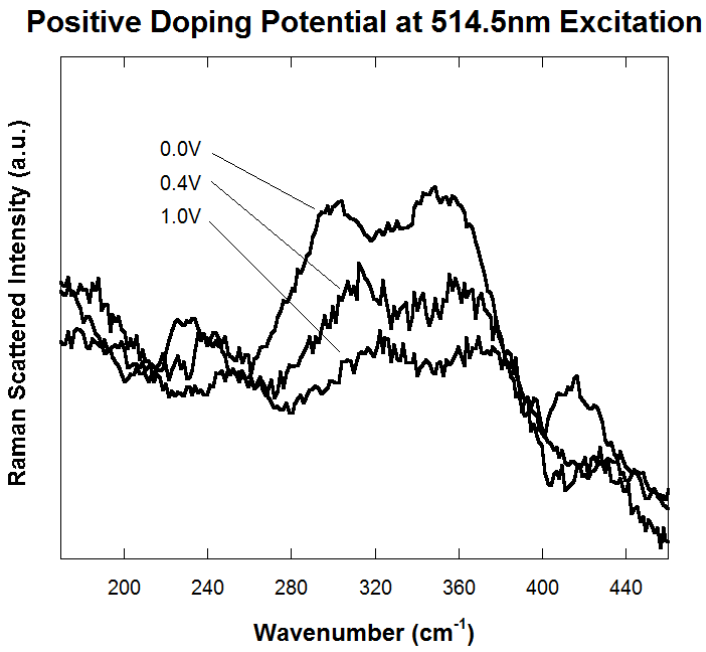

Figure 4.8. The Raman scattering spectrum for the RBM band of semiconducting nanotubes at 3 doping levels: 0V, +.4V and +1V vs Ag/AgCl. The peak intensity decreases and the Raman frequency increases with increasing doping voltage.

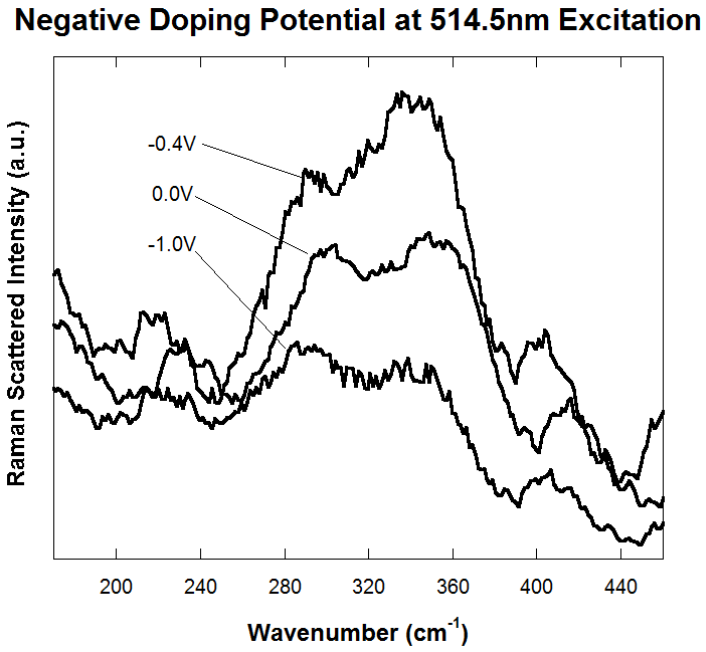

Figure 4.9. The Raman scattering spectrum for the G band of semiconducting nanotubes at 3 doping levels: 0V, -.4V and -1V vs Ag/AgCl. The peak intensity increases, then decreases with increasing doping voltage. The Raman frequencies redshift with increasing voltage.

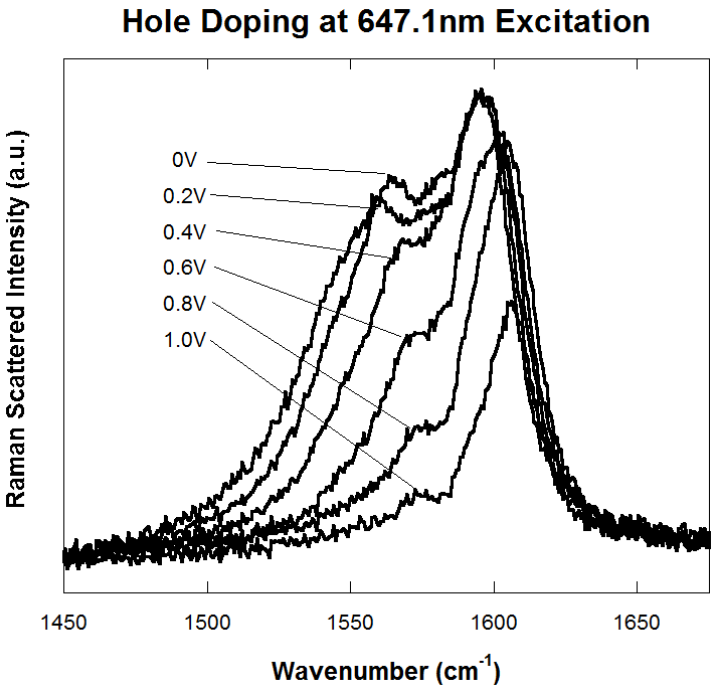

Figure 4.10. The Raman scattering spectrum for the G band of metallic nanotubes at 6 doping levels: 0V, .2V,.4V,.6V,.8V, and +1V vs Ag/AgCl. The peak intensity decreases and the Raman frequency increases with increasing doping voltage.

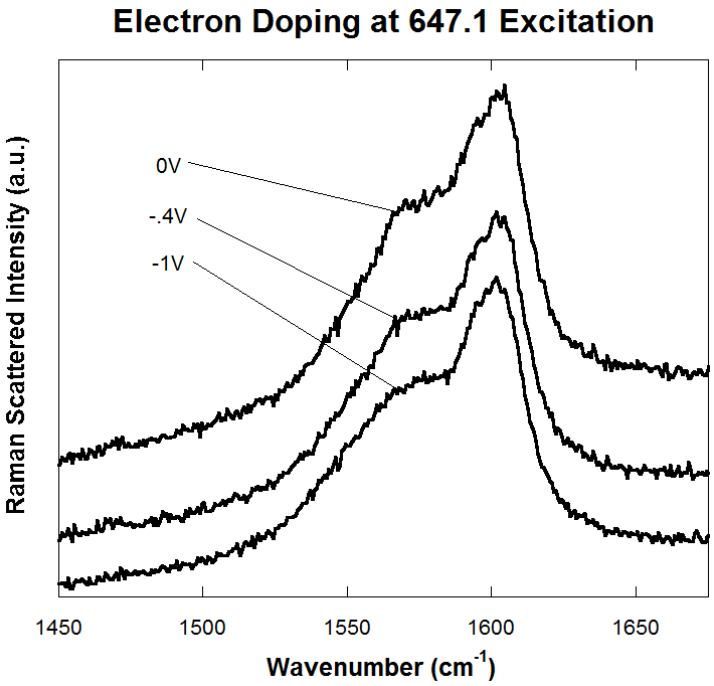

Figure 4.11. The Raman scattering spectrum for the G band of metallic nanotubes at 3 doping levels: 0V, -.4V and -1V vs Ag/AgCl. The plots are shown with an artificial vertical displacement for clarity. There is very little change in the overall scattered intensity, and only a very slight red shift of the frequencies with increasing doping potential.

and the G^+ and G^- modes common to s-SWNTs the qualitative behavior is very similar. Upon the injection of holes (positive doping potential) the overall scattered intensity decreases and the frequencies of both the G band peaks and the anomalous metallic peaks are blue shifted. The injection of electrons (negative doping potentials) results in an increase and subsequent decrease of scattered intensity with increasing voltage. However, the magnitude of the change is much smaller than in s-SWNTs.

4.3.2.2 RBM

Figures 4.12 and 4.13 show the effects of electrochemical doping on the RBM modes of metallic tubes. The general behavior is very similar to the effects on the G band modes. Positive doping potentials result in a blue shift of the Raman frequencies and a reduction in the overall scattered intensity. Negative doping potentials result in a very small change in the scattered intensity and a redshift of the Raman frequencies.

4.3.3 *Ex-situ* Robustness of Electrochemical Effects

As discussed in Chapter 3, the changes in the optical absorption of films of SWNTs due to electrochemical doping are long-lasting. Similarly, the effects on the Raman scattering signal remain after the nanotube film has been removed from the electrochemical cell. Raman spectra were obtained on samples that doped to $1V$ vs Ag/AgCl then removed, rinsed, and dried. In each case the scattering intensity and peak positions begin to approach the undoped level, but the rate of change of the spectrum slows and it approaches an intermediate state between the fully doped and the pristine spectra.

Figure 4.14 shows the fractional change in integrated scattered intensity, along with the fractional change in peak position for the G^- Raman peak for excitation at $514.5nm$. If the only changes to the Raman spectra consisted of the enhancement or reduction of the scattered intensity one might think that the gradual loss of solvent (in this case, water) was responsible for both the changes in optical absorption and in Raman scattering. However, the fact that the Raman frequencies also converge to a condition somewhere between the doped and undoped states

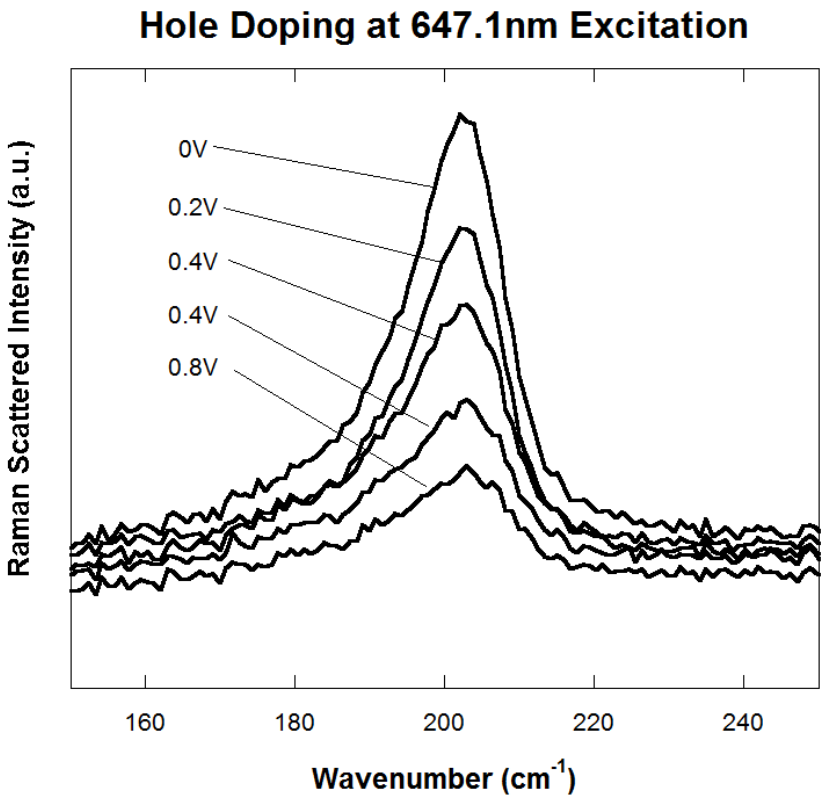

Figure 4.12. The Raman scattering spectrum for the RBM band of metallic nanotubes at 4 doping levels: 0V, .2V,.4V,.6V, and .8V vs Ag/AgCl. The peak intensity decreases and the Raman frequency increases with increasing doping voltage.

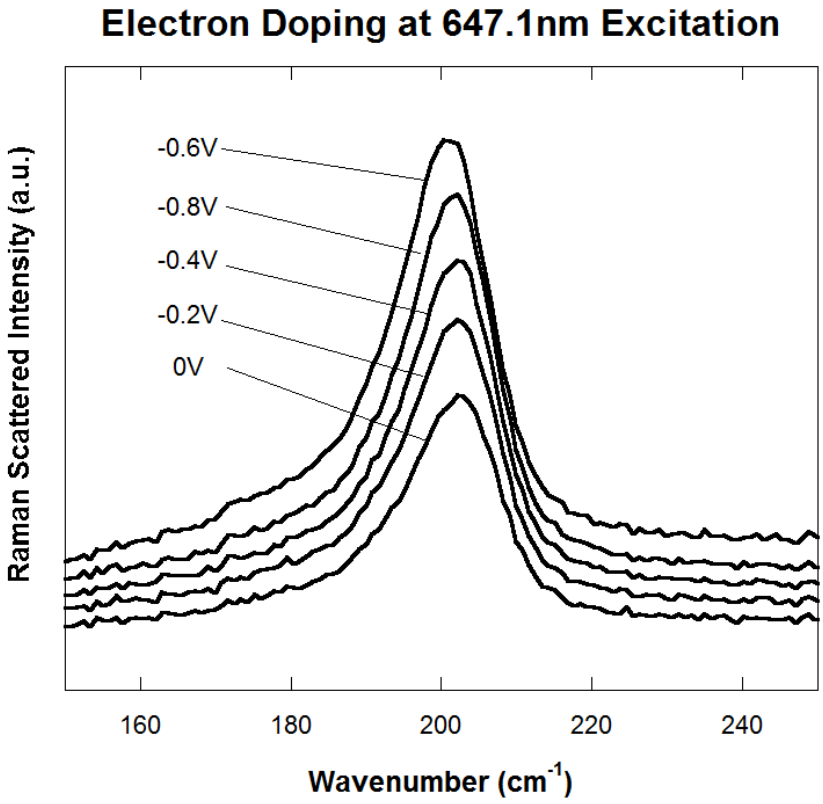

Figure 4.13. The Raman scattering spectrum for the G band of metallic nanotubes at 4 doping levels: 0V, -.2V, -.4V and -.8V vs Ag/AgCl. The plots are shown with an artificial vertical displacement for clarity. There is very little change in the overall scattered intensity, and only a very slight redshift of the frequencies with increasing doping potential.

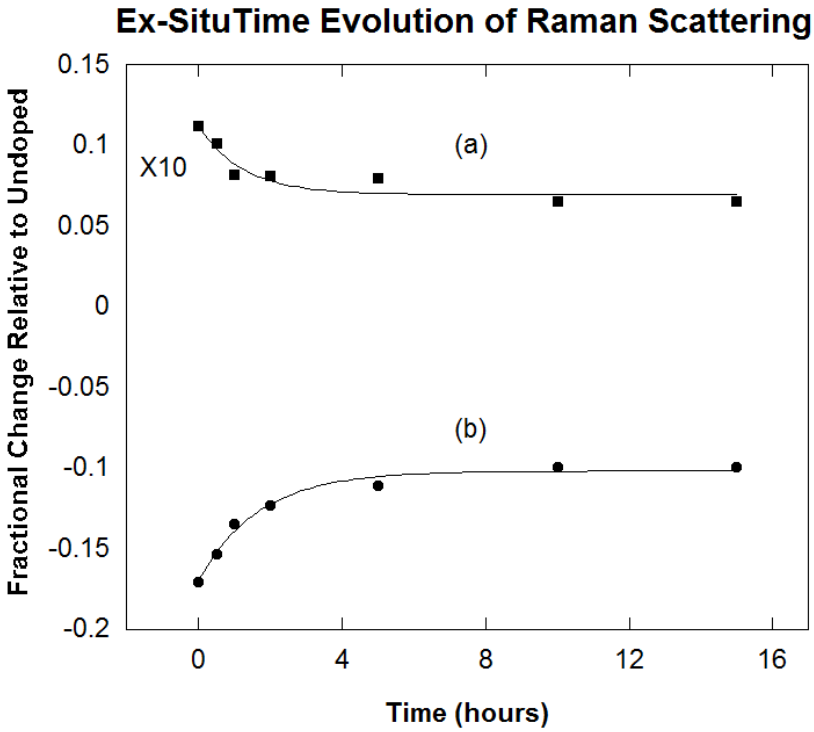

Figure 4.14. The fractional change (relative to the pristine sample) in Raman scattering for several hours after hole doping. The data are represented by points; the solid lines are exponential fits. a) The fractional change in the G^- frequency (magnified ten times). The exponential fit decays with a time constant of $0.69hr$. b) The fractional change in integrated scattering intensity for the G band. The exponential fit decays with a time constant of $0.59hr$.

indicates that this time evolution is, in fact, related to the degree of doping in the sample. This is confirmed via direct measurements of the conductivity of the sample as mentioned earlier (see Figure 3.8). When s-SWNTs are positively doped their conductivity increases.[77] When we measured the conductance of our samples (via the slope of the I-V curve) as a function of time after removal from the electrochemical cell the results were directly comparable to the optical measurements as seen in Chapter 3.

It should be noted that, as discussed in Chapter 2, the electrochemical doping involves the charge transfer from the electrochemical charge double-layer. Therefore, even in apparently dry samples we expect that the doping ions are accompanied by a collection of polar solvent molecules (in our case, usually water). The results shown in Figure 4.14 were obtained using the triple-monochromator configuration explained in Chapter 2. When we attempted the same experiment using the WiTeC machine, where the excitation laser intensity is much higher we observed a monotonic decrease in Raman scattering intensity with time. The Raman signal always approached zero after around 30 minutes. We attribute this to the boiling off of adsorbed water and the subsequent formation of ionic crystals (in most cases, salt) at the surface of the sample immediately under the illumination spot. These crystals were visible in the accompanying optical microscope.

4.4 Summary

4.4.1 Raman Scattering Intensities

The intensity of the resonance Raman spectra for both m-SWNTs and s-SWNTs changes with electron and hole doping for *in-situ* electrochemically doped bulk sheets of nanotubes. For hole doping the intensity of the scattered light decreases with increasing doping potential. For electron doping, on average, the intensity first increases and then decreases. For s-SWNTs we attribute these changes to differences in the amount of light absorbed by the sample. As shown in Chapter 3 the exciton transitions are bleached by electrochemical doping, thereby bleaching the resonant Raman scattering signal. Exciton transitions in metallic tubes, on the other hand, are minimally affected by doping. In the case of

m-SWNTs there is very little change in the scattering intensity for electron doping but for hole doping the change in intensity is similar to s-SWNTs. This is a result of the Kohn-anomaly in m-SWNTs[75] whereby the doping-induced change in the Fermi-level changes the probability for electrons close to the Fermi edge to scatter off of the lattice, thereby changing the resonance Raman scattering cross-section.

4.4.2 Raman Frequencies

Figure 4.15 shows the relative change in Raman frequency for all of the observable first order modes in SWNTs in a heterogeneous sample. The fractional changes in frequencies were measured with laser excitation from a variety of sources. The wavelengths used were as follows: $457.9nm$, $476.5nm$, $488nm$, $496.5nm$, $514.5nm$, $532nm$, $647.1nm$, $676.4nm$, and $740nm$. Each excitation wavelength selects a different subset of nanotubes within the sample, but the results for the changes in mode frequencies were very similar, even for those belonging to the m-SWNTs. This is in contrast to measurements made on individual tubes and suggests a very important intertube interaction in SWNT sheets.

It has been shown that bulk, heterogeneous sheets of nanotubes experience a charge-induced strain when electrochemically doped.[18,19,78] The explanation of this phenomenon depends on both the microscopic nanotube properties and the effect of intertube interactions in bundles of nanotubes. Simultaneous measurements of the strain in individual nanotubes and the resulting change in Raman frequencies illustrate the dependence on chirality,[74] while calculations of the changes in bond lengths for a variety of tubes show that the average effect of adding electrons to a SWNT is to increase the carbon-carbon distance.[18]

In general, the addition of charges to SWNTs changes the character of the sp^2 hybridization in the carbon-carbon bonds which changes the effective spring constant. While the specific effect on individual vibrational modes for different tube types varies, our data suggest that the overall effect is to soften the vibrational modes in bulk SWNT samples, corresponding to a relaxation of the inter-atomic forces and an expansion of the lattice. Our results show that in heterogenous samples of bundled SWNTs this overall softening is transmitted to all of the observable Raman modes in both m-SWNTS and s-SWNTs within the same

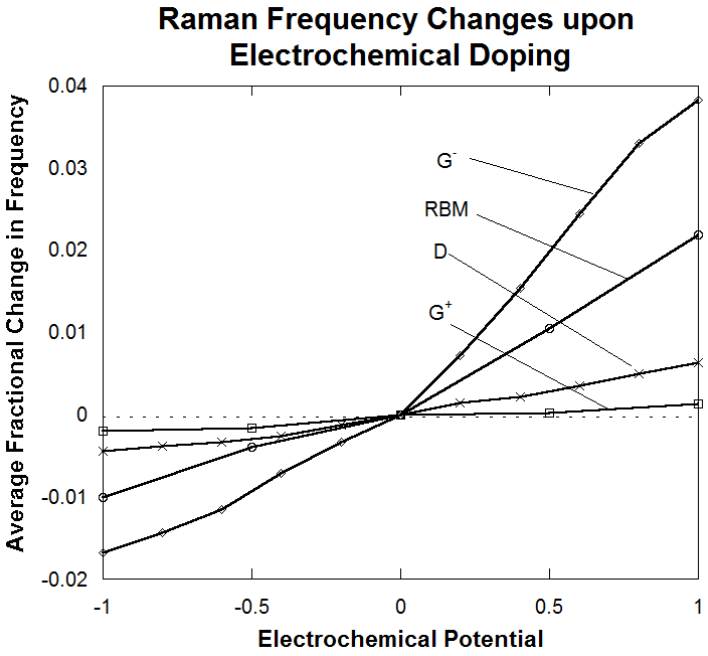

Figure 4.15. The average fractional change for each of the dominant first-order modes in a heterogeneous sample of SWNTs. The addition of holes relaxes the lattice, while the addition of electrons tightens it.

sample. One way in which this could happen is through the strong Van der Waals interaction between tubes in the same bundle.

Consider two adjacent nanotubes of different chirality with a strong Van der Waals attraction as in Figure 4.16. If each tube is given additional electrons (or holes) through electrochemical doping the response of the various bonds, and the corresponding Raman frequencies, will depend on the chirality of each tube. On average, however, the softening (or strengthening) of the intratube carbon-carbon bonds will dominate the overall effect. Thus, the tubes will collectively experience a strain in both the axial and radial direction. This will result in all of the observed Raman modes behaving as though the bond lengths had increased.

The most obvious exception to the rule is the response of the metallic nanotubes in the sample. From experiments on *individual* tubes it has been shown that the RBM frequencies for m-SWNTs actually increase for both electron and hole doping.[75,76] However, on average the metallic tubes constitute no more than one-third of all of the tubes in a given heterogeneous sample. If the various

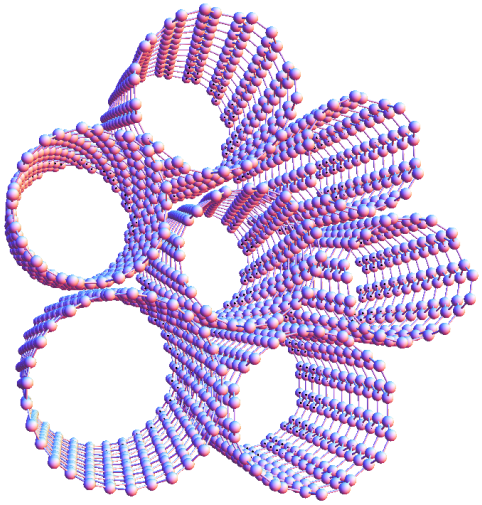

Figure 4.16. A cartoon showing several tubes of slightly different chirality bundled together via Van der Waals interaction. Groups of carbon nanotubes always tend to form bundles or ropes of tubes in a hexagonal lattice as depicted here.

chiralities are evenly mixed in the bundles then the metallic tubes will experience a strain due to the expansion or contraction of their neighbors. Thus, in our data on heterogeneous samples the metallic tube response to hole doping is similar to that of the semiconducting tubes and the frequency shifts are comparable; whereas for electron doping the metallic tubes experience a smaller strain because their intrinsic response is in opposition to the response of their semiconducting neighbors. The average fractional change in Raman frequency for all of the primary modes is on the order of a few percent. This is in agreement with physical measurements made on sheets of nanotubes wherein the total strain on the sheet is on the order of a few percent for the same electrochemical conditions.[18,19,78]

Because even the semiconducting tubes would become conductive at high doping levels we would expect a saturation of the electrochemical actuation effect. However, the amount of doping possible within standard electrochemical methods is very small. Surprisingly to us, but consistent with theoretical predictions, the modes that change the most are those associated with the circumferential direction. Therefore, the strain induced by electrochemical doping in bulk samples seems to be transmitted mostly through a change in diameter. To maximize the

efficiency of a nanotube-based actuator one should ideally orient the nanotube axes perpendicular to the direction in which actuation is desired. Given currently available techniques of growing large arrays of well aligned, monochirality tubes it should be possible to make electrochemical actuators from SWNTs that are far more robust and efficient than their mechanical counterparts at the nanoscale.

CHAPTER 5

CONCLUSIONS AND FUTURE WORK

5.1 Summary

The worldwide interest in carbon nanotubes is motivated by both the unique fundamental physics as well as the potential technological applications. We have contributed to the ongoing investigations into these important properties by demonstrating the response of SWNTs to electrochemical doping, electric field modulation, photomodulation, and charge injection.

We have shown that the primary photoexcitations in SWNTs are excitons, and we have placed a lower limit on the size of those excitons to be $300\mathring{A}^3$. Some of the photogenerated excitons are trapped in low energy manifolds and contribute an EA-like signal to the photo-induced absorption. The screening of these excitons by added charges, as well as the k-space filling by those carriers, results in a bleaching of the exciton transitions signaled by a reduction in the corresponding absorption features. However, the transitions are not blue shifted due to the band-gap renormalization caused by the strong electron-electron interactions in SWNTs. In the case of electrochemical doping (but not necessarily for charge-injection) the plasmon resonance is also shifted by the addition of charges.

In the infrared the absorption of SWNTs is due to Drude free-carriers absorption. The addition of carriers through electrochemical doping as well as direct injection results in an increase in the scattering time and plasma frequency of an ensemble of tubes.

Electrochemical doping also results in a renormalization of the nanotube lattice as evidenced by macroscopic strain measurements as well as shifts in Raman scattered frequencies. While the responses of individual tubes vary according to chirality and species, the collective effect for heterogeneous films is that the injection of electrons softens the circumferential, resonantly enhanced Raman

modes. These modes include the radial breathing mode and the curvature-induced G^- mode. Electrochemical doping at 1 V in 1 M NaCl results in Raman frequency shifts of a few percent, in agreement with macroscopic film strain.

These phenomena have important implications for the development of technologies using SWNTs, and they lead to further questions about their optoelectronic properties. We will discuss some of these open questions in detail.

5.2 What's Next?

5.2.1 Absorption

Absorption spectroscopy of films of SWNTs is inevitably complicated by the heterogeneity of the samples. Unlike photoluminescence and resonant Raman spectroscopies it is difficult to perform absorption measurements on individual tubes because the absorption measurement requires the ability to measure the difference between two large quantities of photons. There are indirect ways to probe the absorption; for example, studying the resonance Raman scattering as a function of incident laser energy.[3] Additionally, there are some advanced techniques such as confocal total internal reflection absorption that could measure the absorption from extremely thin films, but no known technique for measuring the absorption of a single molecule or nanotube. However, since the discovery of SWNTs chemists have explored a variety of ways to separate nanotubes by chirality or species. It is already possible to obtain films of pure s-SWNTs or pure m-SWNTs, and it may not be long before we are able to obtain large quantities of monochirality tubes. Absorption measurements of films of tubes with a well defined chirality would provide invaluable insight into the effects of electrochemical doping and charge injection since they would eliminate any broadening of the exciton transition peaks or ambiguity over which peaks correspond to which type of tube. Even without monochirality samples, absorption measurements on a pure m-SWNT film would confirm the lack of doping- and charge-induced bleaching in the metallic tubes.

5.2.2 Electroabsorption

The electro-bleaching observed in our electroabsorption measurements is different for different samples. We investigated the temperature dependence, field dependence, and light-intensity dependence of the bleaching with no conclusive results. If the bleaching does come from screening due to injected charges as our analysis proposes, then the degree of bleaching in the signal should depend on the transport and contact interface properties of the film. It should be relatively straightforward to carry out EA measurements on films of various concentrations, thicknesses, and matrix materials to verify that injected charges are the source of the bleaching signal.

5.2.3 Raman Spectroscopy

Because of the strong resonance enhancement in SWNTs Raman spectroscopy has already been performed on individual tubes.[35,74,75] However, we have shown that the collective strain experienced by heterogeneous films of nanotubes depends not only on the properties of the individual tubes but also on their interactions. The effects of Van der Waals interactions, intertube charge transfer, π-electron overlap, etc. have been studied theoretically, but a systematic study of intertube effects would be extremely useful in separating individual tube properties from bundle effects. One way to achieve the necessary understanding would be to perform resonant Raman spectroscopy on collections of nanotubes with varying degrees of bundling. Starting from common source material one might vary the processing technique to obtain films in which the size of the nanotube bundles varies from completely isolated tubes to large ropes in a controlled or measurable way. Large survey SEM or TEM images could provide the quantification of the bundle sizes.

Furthermore, it is unclear from our experimental results whether the observed changes in Raman frequencies are due directly to the changes in carrier density or are somehow related to the presence of the dopant at the tubes' surfaces. This is also true in the existing measurements on individual tubes, since the doping is accomplished via a solid electrolyte gate which changes the local dielectric of the nanotube's environment. If one were able to measure the charge-induced Raman

spectrum in a way similar to our CIA experiments it would help separate these two possible effects.

5.3 Looking Forward

While they have been the object of extreme interest for more than two decades it is clear that nanotubes continue to be a fascinating and scientifically relevant system of study. Our classical definitions of "metallic" and "semiconducting" have altered meanings when dealing with these macromolecules because of their quasi-1D structure and the strong and complex electron-electron interactions. As we continue to gain insights into the optoelectronic properties of SWNTs our understanding of the physics of other low-dimensional systems will be strengthened and our ability to design the next generation of nanoscale devices will improve.

REFERENCES

[1] C. Thomsen and S. Reich, in *Light Scattering in Solids IX* (Springer-Verlag, New York, 2007), Chap. 3: Raman Scattering in Carbon Nanotubes.

[2] I. Rubinstein, *Physical electrochemistry : principles, methods, and applications* (M. Dekker, New York, 1995).

[3] A. G. Walsh *et al.*, NanoLetters **7**, 1485 (2007).

[4] H. Kataura *et al.*, Synthetic Metals **103**, 2555 (1999).

[5] S. Iijima, Nature **354**, 56 (1991).

[6] P. Launois *et al.*, Solid State Communications **116**, 99 (2000).

[7] S. Lebedkin *et al.*, Carbon **40**, 417 (2002).

[8] R. Saito, G. Dresselhaus, and M. Dresselhaus, *Physical Properties of Carbon Nanotubes* (Imperial College Press, New Jersey, 1998).

[9] A. Gohier, C. Ewels, T. Minea, and M. Djouadi, Carbon **46**, 1331 (2008).

[10] S. A. Morin, M. J. Bierman, J. Tong, and S. Jin, Science **328**, 476 (2010).

[11] C. Journet *et al.*, Nature **388**, 756 (1997).

[12] W. K. Masera *et al.*, Chemical Physics Letters **292**, 587 (1998).

[13] M. J. Bronikowski *et al.*, Journal of Vacuum Science and Technology A **19**, 1800 (2001).

[14] S. Fan *et al.*, Science **283**, 512 (1999).

[15] T. W. Ebbesen, P. M. Ajayan, H. Hiura, and K. Tanigaki, Nature **367**, 519 (1994).

[16] T.-J. Park, S. Banerjee, T. Hemraj-Bennya, and S. S. Wong, Journal of Materials Chemistry **16**, 141 (2006).

[17] P.-X. Hou, C. Liu, and H.-M. Cheng, Carbon **46**, 2003 (2008).

[18] R. Baughman *et al.*, Science **284**, 1340 (1999).

[19] J. Riemenschneider, S. Opitz, M. Sinapius, and H. Monner, Journal of Intelligent Material Systems and Structures **20**, 245 (2009).

[20] L. J. Hall *et al.*, Science **320**, 504 (2008).

[21] S. Reich, C. Thomsen, and J. Maultzsch, *Carbon Nanotubes: Basic Concepts and Physical Properties* (Wiley-VCH, Berlin, 2004).

[22] T. Ando, Journal of the Physics Society of Japan **66**, 1066 (1997).

[23] H. Zhao and S. Mazumdar, Physical Review Letters **93**, 157402 (2004).

[24] C. L. Kane and E. J. Mele, Physical Review Letters **93**, 197402 (2004).

[25] J. Maultzsch *et al.*, Physical Review B **72**, 241402 (2005).

[26] O. J. Korovyanko *et al.*, Physical Review Letters **92**, 017403 (2004).

[27] J. Deslippe, C. D. Spataru, D. Prendergast, and S. G. Louie, NanoLetters **7**, 1626 (2007).

[28] M. J. O'Connell *et al.*, Science **26**, 593 (2002).

[29] J. N. Coleman *et al.*, Advanced Materials **12**, 213 (2000).

[30] J. N. Coleman *et al.*, Chemical Communications **2000**, 2001 (2000).

[31] D. Chattopadhyay, I. Galeska, and F. Papadimitrakopoulos, Carbon **40**, 985 (2002).

[32] L. Zhanga, Q.-Q. Nia, Y. Fub, and T. Natsuki, Applied Surface Science **255**, 7095 (2009).

[33] M. J. O'Connell *et al.*, Chemical Physics Letters **342**, 265 (2001).

[34] J. Chen *et al.*, Journal of the American Chemical Society **124**, 9034 (2002).

[35] B. White *et al.*, Journal of Physical Chemistry C **111**, 13684 (2007).

[36] Z. Sun *et al.*, Journal of Physical Chemistry C **112**, 1069210699 (2008).

[37] A. Nahata, D. H. Auston, T. F. Heinz, and C. Wu, Applied Physics Letters **68**, 150 (1996).

[38] A. Nahata, A. S. Weling, and T. F. Heinz, Applied Physics Letters **69**, 2321 (1996).

[39] J. I. Pankove, *Optical Processes in Semiconductors* (Springer-Verlag, New York, 1975).

[40] Z. V. Vardeny, J. Orenstein, and G. L. Baker, Physical Review Letters **50**, 20322035 (1983).

[41] Z. V. Vardeny *et al.*, Physical Review Letters **56**, 671674 (1986).

[42] X. Wei, Z. V. Vardeny, N. S. Sariciftci, and A. J. Heeger, Physical Review B **53**, 2187 (1996).

[43] M. Wohlgenannt *et al.*, Nature **409**, 494 (2001).

[44] M. P. Anantram and F. Leonard, Reports in the Progress of Physics **69**, 507 (2006).

[45] M. Shiraishi and M. Ata, Carbon **39**, 1913 (2001).

[46] J. Sun *et al.*, Applied Physics A: Materials Science & Processing **75**, 479 (2002).

[47] M. Zheng and B. A. Diner, Journal of the American Chemical Society **126**, 15490 (2004).

[48] C. M. A. Brett and A. M. O. Brett, *Electrochemistry: Principles, Methods, and Applications* (Oxford University Press, New York, 1993).

[49] F. Wang, G. Dukovic, L. E. Brus, and T. F. Heinz, Science **308**, 838 (2005).

[50] M. F. Lin and D. S. Chuu, Physical Review B **57**, 10183 (1998).

[51] K. Hurst, A. Dillon, D. Keenan, and J. Lehman, Chemical Physics Letters **433**, 301 (2007).

[52] M. M. Brzhezinskaya, E. M. Baitinger, and V. V. Shnitov, Physica B: Condensed Matter **338**, 95 (2004).

[53] P. Yu and M. Cardona, *Fundamentals of Semiconductors* (Springer-Verlag, New York, 2010).

[54] P. Delaney *et al.*, Nature **391**, 466 (1998).

[55] A. Ugawa, A. G. Rinzler, and D. B. Tanner, Physical Review B **60**, 11305 (1999).

[56] B. J. Landi *et al.*, Journal of Physical Chemistry B **109**, 9952 (2005).

[57] A. Rakitin, C. Papadopoulos, and J. M. Xu, Physical Review B **67**, 033411 (2003).

[58] R. J. Elliott, Physical Review **108**, 1384 (1957).

[59] J. U. Lee, Physical Review B **75**, 075409 (2007).

[60] Z. Wu *et al.*, Science **305**, 1273 (2004).

[61] D. Huang *et al.*, Physical Review B **38**, 1246 (1988).

[62] M. Liess *et al.*, Physical Review B **56**, 15712 (1997).

[63] S. J. Martin, H. Mellor, D. D. C. Bradley, and P. L. Burn, Optical Materials **9**, 88 (1998).

[64] T. Drori *et al.*, Physical Review Letters **101**, 037401 (2008).

[65] S. J. Martin *et al.*, Physical Review B **59**, 15133 (1999).

[66] S. Luer, L.and Hoseinkhani *et al.*, Nature Physics **5**, 54 (2008).

[67] H. Kishida, Y. Nagasawa, S. Imamura, and A. Nakamura, Physical Review Letters **100**, 097401 (2008).

[68] C. Gadermaier *et al.*, NanoLetters **6**, 301 (2006).

[69] M. Liess, Z. V. Vardeny, and P. A. Lane, Physical Review B **59**, 11053 (1999).

[70] R. Saito, C. Fantini, and J. Jiang, in *Carbon Nanotubes: Advanced Topics in the Synthesis, Structure, Properties and Applications*, edited by A. Jorio, G. Dresselhaus, and M. Dresselhaus (Springer-Verlag, New York, 2008), Chap. 8: Excitonic States and Resonance Raman Spectroscopy in Single-Wall Carbon Nanotubes.

[71] G. Mahan, Physical Review B **65**, 235402 (2002).

[72] L. Henrard, E. Hernandez, P. Bernier, and A. Rubio, Physical Review B **60**, R8521 (1999).

[73] A. M. Rao *et al.*, Physical Review Letters **86**, 3895 (2001).

[74] S. B. Cronin *et al.*, Physical Review B **72**, 035425 (2005).

[75] H. Farhat *et al.*, Physical Review Letters **99**, 145506 (2007).

[76] H. Farhat *et al.*, Physical Review Letters **102**, 126804 (2009).

[77] O. Kimizuka *et al.*, Carbon **46**, 1999 (2008).

[78] J. Riemenschneider, S. Opitz, M. Sinapius, and H. Monner, Journal of Intelligent Material Systems and Structures **20**, 253 (2009).